

# Surface-enhanced Raman Scattering Based Immunosensors

Kullavadee Karn-orachai

February 2017

# Surface-enhanced Raman Scattering Based Immunosensors

Kullavadee Karn-orachai

Doctoral program in Materials Science and Engineering

Submitted to Graduate School of  
Pure and Applied Sciences  
in Partial Fulfillment of the Requirements  
for the Degree of Doctoral of Philosophy in  
Engineering

at the  
University of Tsukuba

## Acknowledgements

The success of this dissertation could be attributed to the extensive support from my major advisor, Prof. Kazushi Miki.

My special appreciation is extended to my Doctoral Committees, Prof. Masahide Itoh, Prof. Hideki Miyazaki, and Prof. Mitsuhiro Ebara.

I would like to greatly thank Dr. Kenji Sakamoto for his good guidance and support throughout my graduation study. I have gained valuable research experience under his supervision.

I would like to thank Prof. Sirirung Songsivilai, Prof. Tararaj Dharakul, Dr. Rawiwan Laocharoensuk, and Dr. Suwussa Bamrungsap for all of their supports, guidances and fruitful discussions during my stay in NANOTEC.

I would like to thank National Science and Technology Development Agency (NSTDA Thailand) and Japan Science and Technology Agency (JST) provided East Asia Science and Innovation Area Joint Research Program (e-ASIA JRP). I would like to thank The Ministry of Education, Culture, Sports, Science, and Technology (MEXT) for the Japanese Government Scholarship for financial supports.

I would like to thank the past (Khine, Francesca, Ochiai, Yeji, Kanazawa, Tsubomatsu) and present members (Kirill) whose encouraging advice have made my time in the lab productive and inspirational. It was a pleasure to work alongside a remarkable group of students, having developed long lasting friendships with all of them. I would also like to give many thanks to Dr. Satoko Nishiyama, Ms. Masayo Tanaka, and Ms. Eri Sato for taking care of me from the first arrival.

Ultimately, I would like to dedicate the usefulness of this dissertation to my parents, my teachers, and my friends. The dissertation cannot be finished without their inspiration and support. I wish to express my sincere gratitude to my family for their encouragement throughout my course of study.

Kullavadee

Graduate School of Pure and Applied Sciences

Surface-enhanced Raman Scattering Based Immunosensors

(表面増強ラマン散乱検出型イムノセンサー)

Karn-orachai Kullavadee

Doctoral Program in Materials Science and Engineering

Student ID number 201430143

Doctor of Philosophy in Engineering

Advised by Prof. Kazushi Miki

## Abstract

The immunosensor combined with surface-enhanced Raman scattering (SERS) has been recognized as a powerful analytical tool for trace protein detection. The use of SERS as a readout method has attracted much interest because of its advantages, such as high sensitive, nondestructive, no photobleaching and fast detection. Highly sensitive immunosensor can be realized by combining specific recognition of antigen-antibody interactions and high signal enhancement of the SERS effect. Since all proteins are assembled from the similar basic constituents, it is difficult to distinguish the difference of proteins from their Raman spectra. Therefore, the extrinsic SERS immunoassay has been mostly employed for identification the target analyte from other proteins by using SERS probe (antibody-conjugated metal nanoparticles (MNPs) labeled with Raman reporter molecule) as Raman signal generator. The strong and distinctive Raman spectra of Raman reporter molecule are used to detect the selective antigen-antibody recognition. In general, the extrinsic SERS immunosensor consists of the antigen, antibody, SERS probe, and solid substrate. Typically, SERS immunoassay was performed on flat substrates such as polydimethylsiloxane (PDMS) well plate, glass or gold (Au) substrate. No significant electric field enhancement can be expected from the flat substrate. Therefore, in these systems, the enhancement of Raman signal solely comes from the localized surface plasmon resonance (LSPR) of SERS probes. By changing the flat substrate with a nanostructured metallic substrate (SERS substrate), the extra enhancement can be expected through the strong plasmon coupling between the SERS substrate and probes, leading to sensitivity enhancement. In this study, we aimed to improve the sensitivity of SERS immunosensor by using SERS substrates instead of flat substrates. To realize highly sensitive SERS immunosensors, the following experiments were conducted.

In this work, wavelength-tunable SERS substrates with a high binding affinity with the biomolecule

and SERS probes were fabricated. The SERS probes are antibodies-capped Au nanoparticles (AuNPs) labeled with Raman reporter molecules, which are the thiolated molecules that can chemisorb on MNPs and produce strong and unique Raman spectra. The SERS substrates are two-dimensional (2D) arrays of gold core@silver shell (Au@Ag) NPs deposited on indium-tin-oxide (ITO) substrates, which were previously reported as high SERS-active substrates by our group. The substrates were prepared by our original hybrid method, which is a bottom-up deposition method based on self-assembly of alkanethiolate-capped MNPs. The LSPR of the 2D arrays was tuned to a He-Ne laser line of 633 nm by designing the particle structure of Au@Ag NPs: the particle size and the molar ratio of Au/Ag. In the 2D arrays fabrication process, the Au@Ag NPs were capped with a mixed alkanethiolate self-assembled monolayer by treating with a mixture of dodecanethiol and octadecanethiol (6:1 molar ratio). Thus, the as-prepared 2D arrays of Au@Ag core-shell NPs are hydrophobic, which is not suitable for interacting with biomolecules. Thus, the 2D arrays of Au@Ag core-shell NPs must be hydrophilized before utilizing it as a SERS substrate of immunosensors using an aqueous solution. The hydrophilization was successfully performed by replacing hydrophobic molecules of mixed alkanethiols with a hydrophilic molecule of 16-mercaptohexadecanoic acid (MHDA). By performing immunoassay on hydrophilized SERS substrates, the sensitivity improvement of SERS immunosensor was achieved. Two immunoassay formats were used: direct-type and sandwich-type immunoassays. In the direct-type SERS immunoassay, the target antigen is directly immobilized on the substrate, and the amount of them is quantified by detecting the signal from SERS probes. In the sandwich-type immunoassay, the antigen is sandwiched between the capture antibody immobilized on the SERS-active substrate and the detection antibody immobilized on the SERS probes. The amount of antigen is quantified by measuring the signal of the SERS probes. This format enables high sensitive and specific detection.

The principle study of the sensitivity improvement by employing the SERS substrates was firstly performed using a direct immunoassay format. The nucleoprotein of influenza A virus, which is one of the most conserved and abundant structural proteins on the virion, was used as a target. Highly sensitive immunosensors were realized by combining specific recognition of antibody-antigen interaction and high signal enhancement of SERS effect. SERS probes were fabricated by decorating PEGylated, 4, 4'-thiobisbenzenethiol (TBBT)-labeled 25 nm-size AuNPs with Influenza A antibodies. The SERS signal of TBBT at  $1565\text{ cm}^{-1}$  was utilized to detect the selective nucleoprotein-antibody recognition. The stronger

Raman signal was observed for the SERS substrate than for the Au film substrate under the same concentration of the target. The sensitivity was enhanced ~4 times by using the SERS substrates instead of a flat Au film. The limit of detection (LOD) of the immunoassay using the SERS substrate was 8 ng/mL, while that using the Au film substrate was 59 ng/mL. These results indicate that using a well-tuned Au@Ag 2D array as a SERS substrate is an effective way for improving the sensitivity of SERS-based immunosensors. Our SERS immunoassay system revealed high selectivity among other proteins (avidine, ampicillin, bovine serum albumin, lysozyme, and tryptone). Good reproducibility from ten replications was obtained with a small sample-to-sample variation of 4.6% (relative standard deviation). To demonstrate the applicability of our SERS immunoassay system to real biological samples, the detection of influenza A using infected allantoic fluid was also performed. The linear relation between the concentration of infected allantoic fluid and the SERS signal was obtained in the range of 5 to 56 TCID<sub>50</sub>/mL ( $R^2 = 0.96$  for the TBBT Raman bands at 1565 cm<sup>-1</sup>) with the least detection limit of 6 TCID<sub>50</sub>/mL. This finding demonstrated the potential of this SERS immunosensor platform for a high sensitive and specific detection of target molecules in a complex matrix commonly found in clinical specimens. This work indicates that the sensitivity of SERS immunoassay for influenza A was successfully improved by using SERS substrate instead of flat Au substrate.

Then, the factors determining the sensitivity of SERS immunosensor were clarified. In this study, SERS immunoassay was performed using the sandwich format to increase the immobilized and select the target antigen density on the SERS substrate. The influence of the SERS probe size and the interparticle gap distance between the SERS substrate and probe on the sensitivity of sandwich-type SERS-based immunosensors was studied using hydrophilized 2D arrays of Au@Ag NPs as the SERS substrates. The SERS probes were the antibody-capped PEGylated AuNPs with different sized Au-core labeled with 4-mercaptobenzoic acid (MBA). MBA was selected as Raman reporter molecule because of its strong Raman bands at 1089 and 1587 cm<sup>-1</sup> and ability for antibody immobilization. The SERS signal of MBA at 1587 cm<sup>-1</sup> was used to detect the selective recognition between the target antigen and antibody. To realize the highly sensitive detection, the size of SERS probes was optimized by performing a sandwich SERS immunoassay for Human-IgG (H-IgG), where the Au-core size of the SERS probe was varied from 26 to 110 nm in diameter. The maximum SERS intensity was observed at an Au core size of 53 nm. The optimal probe size was found to be determined by the balance between the increase of effective Raman cross-section of a single SERS probe

and the decrease of the probe density on the SERS substrate with increasing probe size.

Next, the influence of the separation distance between the SERS probe and the substrate was examined by performing SERS immunoassay for two antigens with different molecular size using the SERS probes with Au-core of 53 nm. H-IgG and prostate-specific antigen (PSA) were selected as representative large (12 nm) and small (4 nm) antigens. The sensitivity improvement by replacing the flat Au reference substrate with the SERS substrate was evaluated for each immunoassay. The sensitivity improvement was 2.3-fold for H-IgG and 6.4-fold for PSA. The larger sensitivity improvement was observed for the immunoassay for PSA, which is attributed to the smaller immunocomplexes (antibody-antigen-antibody complexes); the shorter separation distance between the SERS probe and substrate induces the stronger plasmon coupling. These results indicate that the sensitivity of the sandwich-type immunoassay performed on the SERS substrate can be improved by adopting a smaller capture- and detection antibodies or antibody fragments for a target antigen. This finding provides a guideline for the selection of biomolecular size in the application of SERS immunosensor utilizing the combination of SERS probe and SERS substrate.

In summary, the improvement of the performance of SERS immunoassay by using hydrophilic 2D arrays of Au@Ag NPs as a SERS substrate was reported. We found that the sensitivity of SERS immunosensors can be improved by replacing the flat substrates with the SERS substrates and also by optimizing the size of SERS probes. The degree of sensitivity improvement depended on the size of the biomolecules (immunocomplexes). The larger sensitivity improvement was observed for the smaller immunocomplexes. This result can be understood by reduction of the separation distance between the SERS probe and the SERS substrate; i.e. the smaller immunocomplex results in the smaller separation distance, leading to the stronger plasmon coupling between the SERS probe and the SERS substrate. This result suggests that the sensitivity of the immunoassay performed on the SERS substrate can be improved by adopting a smaller capture- and/or detection antibodies or antibody fragments for a target antigen. The findings obtained in this doctoral program research provide a guideline to improve the sensitivity of SERS-based immunosensors.

# CONTENTS

	<b>Page</b>
<b>ACKNOWLEDGEMENTS</b>	<b>i</b>
<b>ABSTRACT</b>	<b>ii</b>
<b>LIST OF TABLES</b>	<b>viii</b>
<b>LIST OF FIGURES</b>	<b>ix</b>
<b>CHAPTER I INTRODUCTION</b>	<b>1</b>
<b>CHAPTER II BACKGROUND INFORMATION</b>	<b>6</b>
2.1 Surface-enhanced Raman scattering	6
2.2 Immunosensors	8
2.2.1 Immunoassays	9
2.2.2 Immunoassay formats	11
2.2.3 Transducers for immunoassays	15
2.3 SERS-based immunosensors	19
2.3.1 Intrinsic SERS immunosensors	19
2.3.2 Extrinsic SERS immunosensors	20
<b>CHAPTER III EXPERIMENTAL</b>	<b>25</b>
3.1 Chemicals and biomolecules	25
3.2 Sample preparation	27
3.2.1 Substrates	27
3.2.2 Citrate-citrated AuNPs	27
3.2.3 2D arrays of 42 nmAu@Ag core-shell NPs	28
3.2.4 Hydrophilic SERS substrate	29
3.2.5 Activation of SERS substrate	30
3.3 Instruments	30
3.4 Characterization methods	32
3.3.1 Calibration	32
3.3.2 Selectivity	33
3.3.3 Reproducibility	33
<b>CHAPTER IV DEMONSTRATION OF SURFACE-ENHANCED RAMAN SCATTERING IMMUNOASSAY FOR DETECTION OF INFLUENZA A VIRUS</b>	<b>35</b>
4.1 Influenza A	36
4.2 Experimental	37
4.2.1 SERS probe preparation	37
4.2.2 SERS immunoassay protocol for influenza A	39

## CONTENTS (cont.)

4.3 Results and discussion	40
4.3.1 Characterization of SERS probes	40
4.3.2 Characterization of hydrophilic SERS substrate	42
4.3.3 SERS immunoassay	45
4.3.3.1 Optimization of immunoassay process	45
4.3.3.2 Performance of SERS immunosensing system	46
4.3.3.3 Selectivity	49
4.3.3.4 Reproducibility	50
4.3.3.5 Analysis of nucleoprotein in infected allantoic fluid	51
4.4 Conclusions	53
<b>CHAPTER V INVESTIGATION OF THE FACTORS DETERMINING SENSITIVITY OF SERS IMMUNOASSAY: SERS PROBE SIZE AND SEPARATION DISTANCE BETWEEN SERS PROBE AND SUBSTRATE</b>	<b>54</b>
5.1 Biological systems in this study	55
5.1.1 Immunoglobulin G (IgG)	55
5.1.2 Prostate-specific antigen (PSA)	56
5.2 Experimental	57
5.2.1 SERS probe synthesis	57
5.2.2 Sandwich immunoassay protocol	59
5.3 Results and discussion	60
5.3.1 Characterization of SERS probes	60
5.3.2 Influence of SERS probe size on the sensitivity of immunoassay	62
5.3.3 Influence of separation distance between SERS probe and substrate on the sensitivity of SERS immunoassay	66
5.4 Conclusions	69
<b>CHAPTER VI SUMMARY AND PROSPECTS</b>	<b>71</b>
<b>REFERENCES</b>	<b>75</b>
<b>APPENDIX</b>	<b>82</b>

## LIST OF TABLES

<b>Table</b>		<b>Page</b>
2-1	Optical signal/phenomena employed in optical immunosensors.	19
2-2	Typical Raman reporter molecule in SERS probe synthesis.	23
3-1	Amount of colloidal solution of Au seeds used for synthesizing AuNPs of different sizes.	28
4-1	Possible peak assignment of the Raman spectrum of the EDC/NHS-activation 2D array.	48
4-2	Summary of LOD of representative sensors for detecting infected allantoic fluid.	52
5-1	Structures and properties of IgG subclasses.	56
5-2	Amount of 1 mM ethanol solution of MBA used for labeling AuNPs of different sizes and centrifuge rotor speed for AuNPs of different sizes.	59

## LIST OF FIGURES

<b>Figures</b>	<b>Page</b>
2-1 Schematic illustration of SERS effect.	7
2-2 Typical energy level diagram of a molecule adsorbed on the metal nanostructured substrate. The possible charge transfer excitation are shown by the arrows.	7
2-3 Components of immunosensor. As shown in this figure, there are five steps happen while operating immunosensor. All components are important for the performance of immunosensor. The target analyte is the specific molecule that expected to detect by immunosensor. The bioreceptor is the antibody or DNA or RNA that can specifically bind with a target analyte. The transducer can convert the signal from the successful reaction between the target analyte and bioreceptors into a measurable signal. The signal processor is used for filtering the signal by canceling noise. Recording and display are used for presenting the data for further analyzation process.	8
2-4 Schematic illustration of antibody structure.	9
2-5 Binding event of the epitope of antigen and paratope of antibody.	11
2-6 Diagram illustration of the immunoreaction steps leading to the final binding structures for direct immunoassay using detection antibodies.	12
2-7 Diagram illustration of the immunoreaction steps leading to the final binding structures for indirect immunoassay using polyclonal antibodies as secondary antibodies.	13
2-8 Diagram illustration of the immunoreaction steps leading to the final binding structures for sandwich immunoassay using capture and detection antibodies.	13
2-9 Diagram illustration of the immunoreaction steps leading to the final binding structures for competitive immunoassay using labelled antigens.	14
2-10 Schematic illustration of the electrochemical detection of a sandwich immunoassay for detection of <i>P. falciparum</i> histidine-rich protein.	16
2-11 Schematic illustration of microcantilever immunoassay. The formation of the antigen-antibody complexes provokes a surface stress and, consequently, a deflection of the microcantilever, which is detected optically.	17
2-12 (a) Intrinsic SERS immunoassay of small protein adsorbed on metal nanostructure substrate, and (b) intrinsic detection of DNA in colloidal solution of gold nanoparticles.	20

## LIST OF FIGURES (cont.)

<b>Figures</b>	<b>Page</b>
2-13 Illustration of extrinsic sandwich-type SERS immunoassay performed on the flat solid substrate.	21
2-14 General steps and designs of SERS probes for biomedical applications.	22
2-15 Scanning electron microscope image of various SERS substrate fabrication process. (a) the metal film deposited over nanosphere, (b) metal island deposited on sphere mask, (c) 2D array by electron beam lithography, and (d) 2D nanoholes by atomic layer deposition, and (e) self-assemble monolayer of AuNPs capped alkanethiol.	24
3-1 Molecular structures of chemicals.	26
3-2 Schematic mechanism of carboxyl group activation by EDC/NHS.	30
3-3 Photograph (a) and sketch (b) of experimental set up for the MicroRAM-300 Raman spectrometer consisted of excitation laser (He-Ne laser), an optical lens (50× with a numerical aperture of 0.75), mirrors, edge filter, confocal optical microscope, and detector (CCD).	31
3-4 Typical calibration curve of immunosensor.	32
3-5 Typical selectivity of the immunosensor. The strong intensity was detected from target analyte while the intensities of other proteins (negative results) are weak.	33
3-6 Typical reproducibility of immunosensor. The highlighted area represents the probability of data variation with acceptable value.	34
4-1 Structure of influenza A virus. Influenza A virus has a lipid bilayer envelope, in which there are 8 proteins (PB2, PB1, PA, HA, NP, NA, M, NS). The outer layer of lipid envelope is coated with HA, NA, M1, and N2. [2] The zoomed view is the structure of trimer nucleoprotein. [6] The yellow, red, blue, and green regions represent the amino acid residues reacting with monoclonal antibody.	37
4-2 SEM image of 25nm-citrated AuNPs drop-casted on a Si wafer substrate. The histograms of size distribution of each particles are showed at the right hand side of SEM.	39
4-3 Schematic illustration of SERS probe synthesis (Ab-TBBT-AuNPs).	39
4-4 Schematic illustration of direct immunoassay on 2D Au@Ag NP array substrate. rt: room temperature.	40

## LIST OF FIGURES (cont.)

Figures	Page
4-5 Extinction spectra of colloidal solutions of citrated AuNPs, PEGylated AuNPs labeled with TBBT, and SERS probes.	41
4-6 Raman spectra of solid TBBT, TBBT-PEGylated AuNPs, and SERS probe.	42
4-7 (a) SEM image and (b) size distribution of Au@Ag NPs used in this study. (c) EDX mapping of an Au(42 nm)@ Ag(4.5 nm) NP.	42
4-8 25k and 100k magnification SEM images of (a) as-prepared 2D array and (b) MHDA-functionalized 2D array. The insets of (a) and (b) show the contact angle of a 1×1 water droplet on each substrate surface. (c) Extinction spectra of as-prepared (solid curve) and MHDA-functionalized (dashed curve) 2D array.	43
4-9 ATR-FTIR spectra of the 2D array of Au@Ag NPs: (a) as-prepared hydrophobic 2D array, (b) after annealing at 90°C for 1 h, and (c) after MHDA treatment.	44
4-10 (a) Raman spectra when the immunoassay was performed with different incubation time of recombinant nucleoprotein, and (b) Relationship between the peak intensity of the 1565 cm <sup>-1</sup> band of TBBT and the incubation time of recombinant nucleoprotein. The dashed curve is a guide for the eye.	46
4-11 (a) Raman spectra of the immunoassay performed with different incubation time of SERS probes under a fixed immobilization condition of the recombinant nucleoprotein (1.34 μg/mL and 30 min), and (b) peak intensity of the 1565 cm <sup>-1</sup> band of TBBT corresponding to incubation time of SERS probes. The dashed curve is a guide for the eye.	46
4-12 (a) Raman spectra of the immunoassay performed on the SERS substrates. The concentration of nucleoprotein was: 0 (control), 0.0067, 0.0134, 0.067, and 0.134 μg/mL from the bottom to the top. (b) Sensitivity curves of the immunoassay performed on the SERS and Au substrates over the entire measurement range from 0.0067 to 134 μg/mL of nucleoprotein concentration. These sensitivity curves were obtained from the peak intensity of the 1565 cm <sup>-1</sup> band. The solid and dashed curves are guides for the eye. (c) Sensitivity curves in the linear region. The solid and dashed straight lines are obtained by the method of least squares. The solid and open symbols in (b,c) shows the data points for the immunoassay performed on the SERS and Au substrates, respectively.	49

## LIST OF FIGURES (cont.)

Figures	Page
4-13 Selectivity of SERS immunoassay. The concentration of all proteins were fixed at 13.4 $\mu$ g/mL. The peak intensity of the 1565 cm <sup>-1</sup> band was plotted.	50
4-14 Reproducibility of SERS immunoassay (peak intensity of the 1565 cm <sup>-1</sup> band). The concentration of recombinant nucleoprotein was fixed at 1.34 $\mu$ g/mL.	51
4-15 (a) Raman spectra of the immunoassay for infected allantoic fluid, whose concentration was varied from 0 (control) to 56 TCID <sub>50</sub> /mL. (b) Sensitivity curve of the SERS immunoassay for influenza A infected allantoic fluid. This sensitivity curve was obtained by plotting the peak intensity of the 1565 cm <sup>-1</sup> band. The data points over the entire measurement range are shown in the inset. The dashed straight line was obtained by the method of least squares.	53
5-1 Schematic illustration of sandwich immunoassays for Human IgG and PSA.	60
5-2 (a) SEM images of the citrate-capped AuNPs of different sizes. (b) Normalized extinction spectra of the PBS solutions of SERS probes of different sizes. (c) Raman spectra of the solid MBA and the 53 nm-SERS probes. (d) ATR-FTIR spectra of the PEGylated MBA-labeled AuNPs and the SERS probes of 53 nm in diameter.	62
5-3 (a) SERS spectra of the sandwich immunoassay for H-IgG performed at a constant H-IgG concentration of 1 ng/mL using SERS probes of different sizes. (b) Probe size dependence of the SERS intensity of the 1587 cm <sup>-1</sup> band. The broken curve is a guide for the eye.	63
5-4 Sensitivity curves of H-IgG immunoassay using three probe size (26, 53, and 110 nm). The broken straight lines were obtained by the method of least squares.	64
5-5 Raman spectra of immunoassay for H-IgG performed on the SERS substrates using (a) 26, (b) 53, and (c) 110 nm-SERS probes. The concentration of the antigen solution was varied from 0 (control) to 10 ng/mL: a = control, b = 0.1 pg/mL, c = 1 pg/mL, d = 10 pg/mL, e = 0.1 ng/mL, f = 1 ng/mL, and g = 10 ng/mL.	65
5-6 Representative SEM images of sandwich immunoassay substrates performed at a H-IgG concentration of 1ng/mL using SERS probes of different sizes. Probe size dependence of (b) probe density and (c) SERS intensity of a single probe. The broken curves are guides for the eye.	66

## LIST OF FIGURES (cont.)

### Figures

	<b>Page</b>
5-7 Raman spectra of the immunoassay for H-IgG performed on (a) SERS (2D array of Au@Ag NPs) substrates and (b) Au film substrates using 53 nm-SERS probes. The concentration of antigen solutions are: a = 0 (control), b = 0.1 pg/mL, c = 1 pg/mL, d= 10 pg/mL, e = 0.1 ng/mL, f = 1 ng/mL, and g = 10 ng/mL. Raman spectra of the immunoassay for PSA on (c) SERS and (d) Au film substrates using 53-nmSERS probes. The concentration of antigen solutions are: a = 0 (control), b = 0.01 pg/mL, c = 0.1 pg/mL, d= 1 pg/mL, e = 0.01 ng/mL, f = 0.1 ng/mL, and g = 1 ng/mL.	68
5-8 Sensitivity curves of the sandwich SERS immunoassays for (a) H-IgG and (b) PSA performed on the SERS and Au film substrates. The broken lines are obtained by the method of least squares. Schematic illustration of sandwich immunoassay for (c) H-IgG and (d) PSA.	69

## LIST OF COMMON ABBREVIATIONS AND SYMBOLS

2D: two-dimensional	SEM: scanning electron microscope
MCH: 6-mercaptohexanol	SERS: surface-enhanced Raman scattering
MHDA: 16- mercaptohexadecanoic acid	TEM: transmission electron microscopy
TBBT: 4, 4'-thiobisbenzenethiol	UV: ultraviolet
LSPR: localized surface plasmon resonance	Vis: visible
ITO: indium tin oxide	PSS: polystyrene sulfonate
AuNPs: gold nanoparticles	PAA: polyacrylic acid
Au@Ag NPs: gold core@silver shell nanoparticles	PAH: poly (allylamine) hydrochloride
MBA: 4-mercaptobenzoic acid	DADMAC: poly (dimethyl diallyl ammonium chloride)
SH-PEG: thiol polyethylene glycol	AuNPs: gold nanoparticles
SH-PEG-COOH: thiol polyethylene glycol acid	AgNPs: silver nanoparticles

## CHAPTER I

### INTRODUCTION

The increase of death or patients arises from the lack of highly sensitive and specific point-of-care (POC) testing devices, such as the devices for glucose detection using enzyme and the test for infectious diseases using genetic materials (DNA and RNA) or antibody. The good detection method offers important information for helping clinical judgement and treatment decision. The development of disease testing devices with low cost, high reliability, sensitivity, selectivity, easy to handle, and no requirement of large amount of sample is very helpful for early diagnosis. This is the expectation for the medical profession to decrease the number of death and prevent the complication of disease. In past several decades, the high sensitive and specific sensors towards early diagnosis have been developed with high accuracy for monitoring the patients. Immunoassay is one type of quantitative bioanalytical methods for detecting the proteins or pathogens in human body fluid relying on the specific recognition of antigen and antibody [1,2]. These methodologies provide many advantages, such as high specificity, sensitivity, and accuracy [3]. Immunoassays have been widely applied in many research areas, such as clinical diagnosis and pharmaceutical analysis, and in the food industry [2,4]. At the present time, immunoassays are routinely employed in the practical clinical laboratory diagnosis to minimize the spread of contagious diseases. The demand for the highly sensitive and trace amount analysis for POC diagnosis is increasing. Thus, further improvement of the detection performances (especially sensitivity and limit of detection (LOD)) of immunoassays is strongly required.

Breakthroughs in analytical readout techniques coupled with immunoassays lead to improvement in detection performances [5]. There are attempts using various transducers to perform high sensitive immunoassays, such as electrochemical, piezoelectric and fluorescence transducers. Fluorescence transducer is the most widely used detection technique for immunoassay, which requires the fluorescent labels immobilized on biomolecules. This transducer offers high sensitivity, but it suffers from interferences from background signals. Other detection techniques were reported for improving the immunoassay performances, e.g. surface plasmon resonance (SPR), microcantilever, and surface-enhanced Raman scattering (SERS). The SPR- and microcantilever-based immunoassays are label-free detection methods. In the SPR-based

immunoassay, the antigen is detected by measuring the change of refractive index at the metal surface when the antigen or antibody binds on the metal film. This technique has been developed for detection of low antigen concentration as well as real-time monitoring. However, this detection is limited for the detection of small biomolecules because the small change of refractive index is indistinguishable. In the microcantilever-based immunoassay, the antigen-antibody binding events are detected from the resonance frequency shift or bending of the microcantilever, which is very sensitive to the mass change on the microcantilever and capable of real-time detection. However, this technique suffers from the long-term drift of microcantilever bending [5]. In past few decades, the improvement of immunoassay performances (sensitivity, and LOD) has been reported by employing SERS as a readout method. SERS is the effect that enhances the Raman signal of the molecule adsorbed on metal nanostructured substrates. This SERS effect enables the detection of Raman vibrational fingerprints of adsorbed molecules and provides ultrasensitive detection up to a single molecule detection. SERS offers several advantages over other detection methods, such as no photobleaching, fast, nondestructive, high sensitive, high structural selective, and multiplexing detection [6].

Recently, immunoassays using metal nanostructures have been developed for improving sensitivity through the SERS effect. SERS-based immunoassays combine the specific recognition of antigen-antibody and high signal enhancement of the SERS effect. SERS-based immunoassays can be performed as either label-free or label detection [7,8]. The label-free (intrinsic) SERS immunoassay employs the metal nanostructures as solid supports for enhancing the intrinsic Raman scattering of adsorbed biomolecules. The adsorbed biomolecule can be directly identified from the measured spectrum [7]. However, this intrinsic detection is unable to detect target biomolecules in complex samples containing various kinds of proteins because overwhelming background signals from the matrices interfere with the signal of the target biomolecule. To improve the specificity of detection and eliminate interference signals, the label (extrinsic) SERS immunoassays have been proposed. The amount of target biomolecule is indirectly determined from the signal intensity of Raman reporter molecules that are labeled on metal nanoparticles (MNPs). The Raman signal of the Raman reporter molecule is significantly enhanced through the localized surface plasmon resonance of MNPs [7,8]. To date, the extrinsic SERS immunoassays have been mostly applied in the diagnostic tests for infectious diseases, cancers, and tumors. This is because extrinsic detection provides many advantages over

conventional fluorescence detection, such as no photobleaching, and narrow spectral width of Raman peaks, which can reduce the overlap between different label molecules.

In my doctoral program research, a highly sensitive detection method has been developed by fabricating SERS-based immunoassay, which is the combination of immunoassay method and SERS readout. SERS-based immunoassay employing extrinsic SERS immunoassay platform offers strong potential to a great sensitive detection method for the clinical diagnosis. This study has been motivated by the increasing demand for highly sensitive and specific detection technique for early disease diagnosis, and SERS immunosensors with high sensitivity were fabricated. The applicability of this sensor for detection of cancer biomarker and influenza A virus was demonstrated. To fabricate high sensitive SERS-based immunosensors, the hydrophilic 2D arrays of Au@Ag NPs were used as the SERS substrates instead of flat substrates for increasing the sensitivity of immunoassays. The hydrophilicity of these substrates plays an important role in the immobilization of the biomolecules. The hydrophilic functional groups (e.g. COOH, and NH<sub>2</sub>) are used for capturing and retaining the biomolecules on the substrates while performing immunoassays. In addition to the hydrophilicity, the nanostructure of these substrates is useful for amplifying the Raman signal through the electromagnetic field enhancement. The attractive features of our hydrophilic SERS substrates are high particle coverage, high uniformity, hydrophilicity, and LSPR tunability to the excitation laser light in the Raman measurement. Moreover, to detect target antigen with strong Raman signal and low background signal, SERS probes were employed. A variety of SERS probe structures has been reported in many literatures. In our study, Au sphere particles, which have been widely used as a core of SERS probe, were employed as the solid support because it is easy to synthesize with high uniformity in size and shape. In order to achieve better sensitivity, the optimization of SERS probe size should be conducted. By combined use of SERS substrates and SERS probes in the SERS immunosensors, the sensitivity enhancement is expected to be obtained through the plasmon coupling between these SERS-active materials. Moreover, it has been reported that the size of biomolecules, which acts as the barrier between SERS probe and substrate, has an effect on the sensitivity of immunosensor. However, improvement of sensitivity by decreasing the size of antibody was still not confirmed. Herein, we reported a novel combination of 2D arrays of Au@Ag NPs on ITO substrates, whose LSPR was tuned to a He-Ne laser line of 632.8 nm, and immuno Au sphere labeled with Raman reporter molecule for detection of Influenza A virus and prostate-specific antigen (PSA). The sensitivity improvement

for immunoassay of influenza A and PSA was 4-fold and 6.4-fold, respectively, when performing these immunoassay on SERS active substrates. Moreover, we firstly proved that the sensitivity of immunoassays was improved by optimizing the size of SERS probe. We found that the maximum sensitivity was obtained by using 53-nm probes. We also confirmed the influence of separation distance between SERS probe and substrate on the sensitivity improvement. By reducing the immunocomplexes from 36 nm to 28 nm, the sensitivity was improved 3-fold. The objectives of this study are (i) to fabricate the SERS immunosensor using hydrophilic 2D arrays of Au@Ag core-shell NPs as the SERS substrates and antibody-coated Raman reporter molecule-labeled AuNPs as the SERS probes for demonstrating influenza A virus detection under real biological condition, and (ii) to improve the sensitivity of sandwich type SERS-based immunosensors by optimizing SERS probe size, and investigating the influence of separation distance between SERS probe and substrate.

This dissertation is composed of six chapters. The introduction, the overview of immunoassays, the motivation, and objectives of this research, and the structure of this dissertation are presented in this chapter. Chapter 2 introduces SERS, immunosensors and SERS-based immunosensors. The synthesis of AuNPs, and Au@Ag NPs, the fabrication of ITO, Au, and SERS substrates, the preparation of SERS probes, the immunoassay protocol, the instruments, and the characterization methods are written in chapter 3. In chapter 4, the demonstration of SERS-based immunoassays for influenza A detection relying on direct immunoassay format is described. The study on the factors determining the sensitivity of SERS immunoassay is reported in chapter 5. The optimization of SERS probe sizes for highest sensitivity enhancement in immunoassays is reported. Moreover, the investigation of the influence of separation distance between the SERS probe and the SERS substrate on the sensitivity are also described. Finally, in chapter 6, I summarized the major findings in this research and discussed the possible future perspective of this research.

## List of publications

1. K. Karn-orachai, U. Ruktanonchai and S. M. Smith, *Adv. Mat. Res.*, 2012, **364**, 313-316.
2. K. Karn-orachai, S. M. Smith, S. Phunpee, A. Treethong, S. Puttipipatkajorn, and U. R. Ruktanonchai, *J. Microencapsul.*, 2014, **6**, 609-618.
3. K. Karn-orachai, S. Nishiyama, and K. Miki, *J. Photopolym. Sci. Tec.*, 2014, **27**, 273-276.
4. K. Karn-orachai, S. M. Smith, S. Saesoo, A. Treethong, S. Puttipipatkachorn, S. Pratontep, U. Ruktanonchai, *Colloid Surface A.*, 2016, **488**, 118-128.
5. K. Karn-orachai, K. Sakamoto, R. Laocharoensuk, S. Bamrungsap, S. Songsivilai, T. Dharakul, and K. Miki, *RSC adv.*, 2016, **6**, 97791-97799.
6. K. Karn-orachai, K. Sakamoto, R. Laocharoensuk, S. Bamrungsap, T. Dharakul, and K. Miki, *RSC adv.* (Accepted on Feb. 22<sup>th</sup>, 2017).

## CHAPTER II

### BACKGROUND INFORMATION

This chapter introduces the surface-enhanced Raman scattering (SERS), immunosensors (immunoassays, components of immunoassays, immunoassay formats), and SERS-based immunosensors (types of SERS immunosensor, SERS probes, SERS substrates, and characteristic of immunosensors).

#### 2.1 Surface-enhanced Raman scattering (SERS)

SERS phenomenon was firstly discovered in 1974 by Fleischmann and coworkers who observed the enhancement of Raman spectra of pyridine adsorbed on roughened silver electrode [9]. The phenomenon was correctly interpreted by Albrecht *et al.* and Van Duyne *et al.* in 1977 [10,11]. It was reported that the Raman scattering can be significantly enhanced when target molecules adsorbed onto or in close proximity to metal nanostructured substrates (Fig. 2-1). Substrates for SERS measurement are typically made of gold (Au) and silver (Ag). This is because localized surface plasmon resonances (LSPRs) of these metals lie in the visible and near infrared wavelength region, which cover the range of the excitation laser wavelength of Raman measurement. By exploiting of the SERS effect, Raman signals of target molecules can be enhanced by several orders of magnitude. Therefore, it is possible to detect molecules at low concentrations without label molecules. There are two underlying mechanisms to explain the SERS phenomenon: electromagnetic [11] and chemical enhancement [10]. The electromagnetic enhancement mechanism (EM) is the dominant enhancement with the highest contribution to the enhancement factor by 11 orders of magnitude [12]. EM is caused by the enhanced electromagnetic field of metal nanostructures excited by excitation laser. The enhancement is maximized when the frequencies of excitation laser and localized surface plasmon resonance (LSPR) of the metallic nanostructure (substrate) are properly matched. The LSPR of the metal nanostructure is dependent on the size, shape, and type of materials. This EM enhancement is chemically non-selective, but distance-dependent [13,14]. The enhancement can vary by several orders of magnitude, depending on the distance between adsorbate and substrate. Another mechanism is chemical enhancement mechanism (CM), which originally

risks from the charge transfer between adsorbed molecules and metal nanostructured substrates. The charge transfer in SERS has been proposed and illustrated in Fig.2-2 [15,16]. Firstly, the electronic state of adsorbed molecules is shifted and broadened by their interaction with metal nanostructures. The charge transfer involves the transfer from metals to adsorbates or from adsorbates to metals. These interactions lead to signal enhancement up to  $10^2$  [17]. Until now, SERS has proved as a powerful detection method for investigation of the structure and vibrational properties of target molecules adsorbed on metal nanostructures.

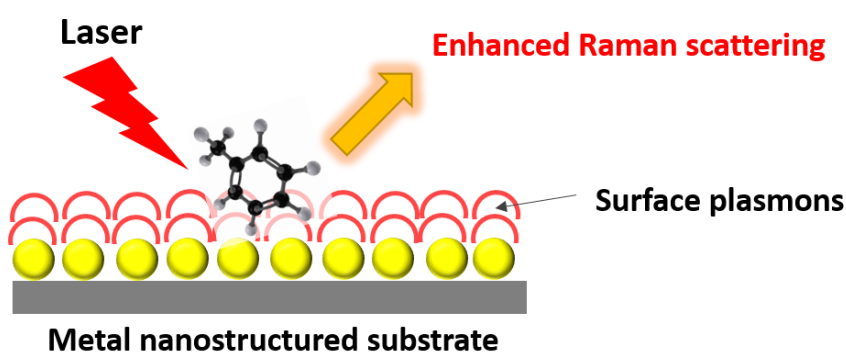


**Fig. 2-1** Schematic illustration of SERS effect.

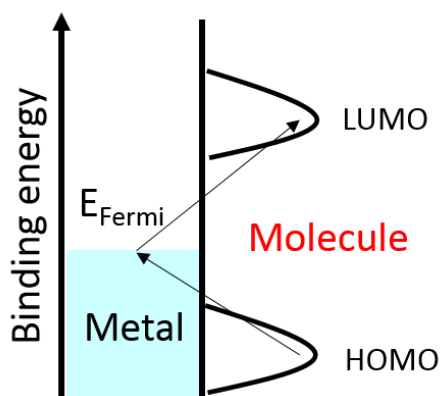


**Fig. 2-2** Typical energy level diagram of molecule adsorbed on a metal nanostructured substrate. The possible charge transfer excitation is shown by the arrows.

## 2.2 Immunosensors

Immunosensor, affinity-type biosensor, consists of target analytes (food, environmental, biological samples), bioreceptors (antigen-antibody, DNA, aptamer) immobilized on solid support and transducers, which translate the signal from the successful reaction between the target analyte and bioreceptors to the detectable data [18]. The typical systematic illustration of immunosensor is shown in Fig. 2-3. Immunosensor is the essential analytical device in the research areas of clinical diagnostics and point-of-care (POC) testing because it provides several advantages including high sensitivity, specificity, and accuracy [3]. Regarding its benefits, there is no doubt that immunosensors have been applied in the practical use especially in the medical areas.

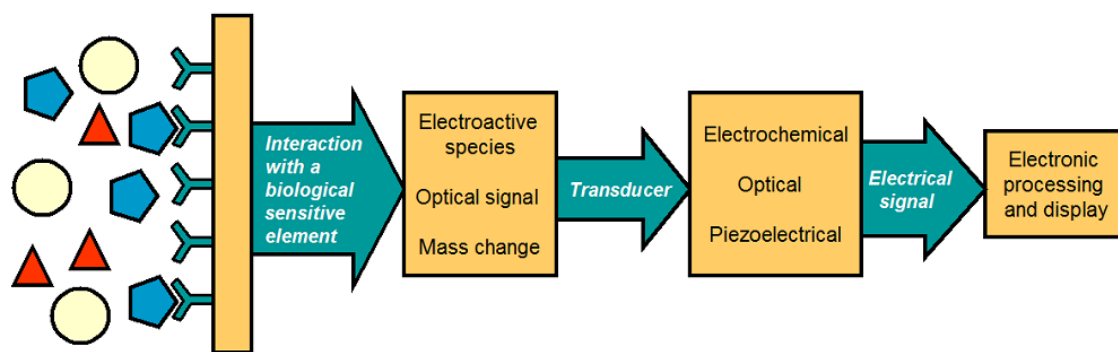


**Fig. 2-3** Components of immunosensor. As shown in this figure, there are five steps happen while operating immunosensor. All components are important for the performance of immunosensor. The target analyte is the specific molecule that expected to detect by immunosensor. The bioreceptor is the antibody or DNA or RNA that can specifically bind with a target analyte. The transducer can convert the signal from the successful reaction between the target analyte and bioreceptors into a measurable signal. The signal processor is used for filtering the signal by canceling noise. Recording and display are used for presenting the data for further analyzation process.

### 2.2.1 Immunoassays

Immunoassay is the analytical method employed in immunosensors for detecting the concentration of biomolecule in a sample by specific antigen-antibody recognition. The methodology was firstly developed for detecting the insulin in 1960. Immunoassays are still continuously used especially in the health diagnostic labs for early diagnosis for several diseases. Moreover, immunoassays have also been employed in the food safety and environmental analysis. Immunoassays provide several advantages, such as high specificity and sensitivity. However, immunoassays suffer from the high price of antigen and antibody. Immunoassays consist of two main components: antigens, and antibodies. The antibody is produced from plasma cell that related to the immune system. The antibody can specifically recognize a unique molecule, which is called antigen. The information of immunoassay components is given below.

The antibody is the protein molecule that can specifically identify complementary antigen. The antibody or the other name is immunoglobulin (Ig). Immunoglobulin has been classified into five subclasses, e.g. IgG, IgE, IgM, IgA, and IgD, which has the different functions in the immune system [19]. The common antibody that mostly found in human serum is IgG isotype, which has a flexible Y-shaped structure with 150 kDa containing 4 polypeptide chains (two heavy chains and two light chains). The two heavy chains are connected to each other via a disulfide bond (-S-S-) and the two light chains are also linked with heavy chains via disulfide bonds (-S-S-). The structure of an antibody is shown in Fig. 2-4. The Y-shaped antibody consists

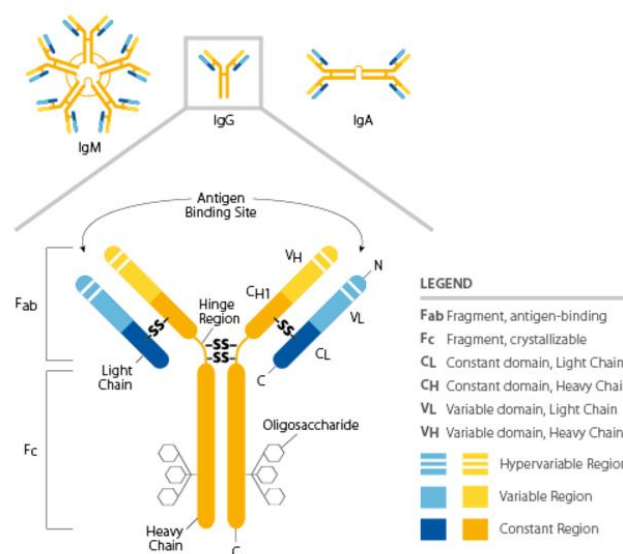


Fig. 2-4 Schematic illustration of antibody structure.

of three equivalent size parts: two arms and one trunk. The two arms of Y structure are called variable region or Fab fragment, where the antigen-antibody binding occurs. Each antibody is designed to react with particular antigen due to the difference of amino acid sequence at Fab fragment. The trunk of antibody is named a constant region or Fc region, which cannot bind with antigen but can react with macrophages, natural killer cells and neutrophils [20]. The antibodies have two types: monoclonal and polyclonal antibodies. Monoclonal antibodies have a monovalent affinity with a single binding site of antigen. Whereas, polyclonal antibodies can bind to multiple binding sites of antigen. For high specific recognition of target analyte, the monoclonal antibodies are preferably used.

Antigen stands for **Antibody Generator**, which was proposed by Paul Ehrlich; German Scientist. The antigen is the molecule that can stimulate an immune response and antibody on the host after entered or created by host's body. The molecules that can act as an antigen are glycoproteins in or out plasma membrane, peptides, polysaccharides, nucleic acids, and lipids. The antigen can be specifically captured by the complementary antibody.

The antibody interacts with antigen via a lock and key model. The strength of reaction is referred to the affinity of reaction, which is determined by the binding strength between antigen's epitope and antibody's paratope (Fab fragment). The epitope is the binding site of antigen, while the paratope is the binding site of an antibody [19]. Fig. 2-5 shows the epitope of antigen and paratope of antibody. There are many forces get involved in the interaction of antigen at Fab fragment of an antibody, i.e. electrostatic force, hydrogen bonds, hydrophobic interaction and van der Waals force. These forces are weak, which makes the reversible antigen-antibody bond. This reaction is not only reversible but also accept the law of mass action, for example, the reaction rate is proportional to the concentration of antigen and antibody. The equilibrium constant ( $K_{aq}$ ) or the affinity constant of antigen (Ag)-antibody (Ab) interaction can be calculated as shown in equation 1. At equilibrium, the ratio of the concentration of product (antigen-antibody complex) and reactants (antigen and antibody) is constant. The affinity of antigen-antibody interaction depends on not only the aforementioned forces but also the pH, temperature, concentration and ionic strength of electrolyte, type of antigen and antibody [21]. The value of  $K_{aq}$  of antigen-antibody recognition normally falls in the range of  $10^6$ - $10^{12}$   $M^{-1}$

[22]. The higher affinity of immunoassay system results in irreversible interaction between antigen and antibody.

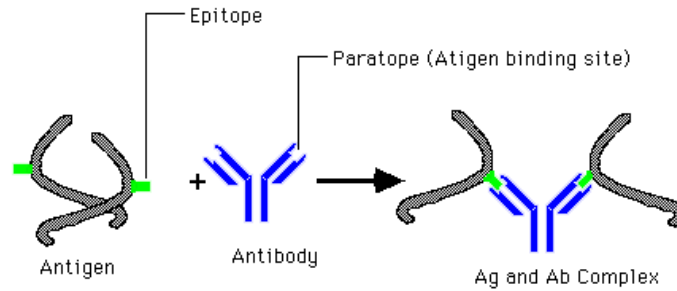
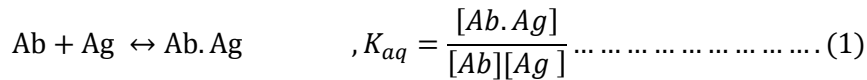


**Fig. 2-5** Binding event of epitope of antigen and paratope of antibody.

### 2.2.2 Immunoassay formats

Immunoassays have two main platforms that depend on the separation process of unbound biomolecules from the reaction [23]. The homogeneous immunoassay, such as agglutination, capillary electrophoresis, fluorescence polarization, and fluorescence-resonance energy-transfer-based immunoassay, do not require any separation process. Another platform is called heterogeneous immunoassay, which requires the separation of unbound molecules from immunocomplexes. In this platform, immunoreagents have to immobilize on a solid support, which is convenient for removing unbound molecules. The specifically bound target antigen can be only measured without any contaminations. The materials used as supporting substrate for immobilizing biomolecule (e.g. antigen, antibody, DNA) play a crucial role for the binding affinity of the biomolecule. Immunoassays performed on the substrates can be carried out with four ways of formats, such as direct, indirect, sandwich, and competitive immunoassays. The format selection for immunoassay depends on the dynamic range of analytes and sensitivity of detection. The schematic illustrations of reaction steps of all immunoassay formats are shown in Fig. 2-6 to 2-9 and the details of each format are described below.

## A. Direct immunoassay

The direct immunoassay is the simplest immunoassay format. For direct immunoassay, the antigen is directly immobilized on a solid substrate and it is detected by monitoring the signal from added primary antibody conjugate (Fig. 2-6). This model is good for quick detection with few step of immunoassay and no cross-reaction from secondary antibody. However, no commercial kits are available because it provides some disadvantages; (i) primary antibody is expensive, (ii) signal amplification is low [23].

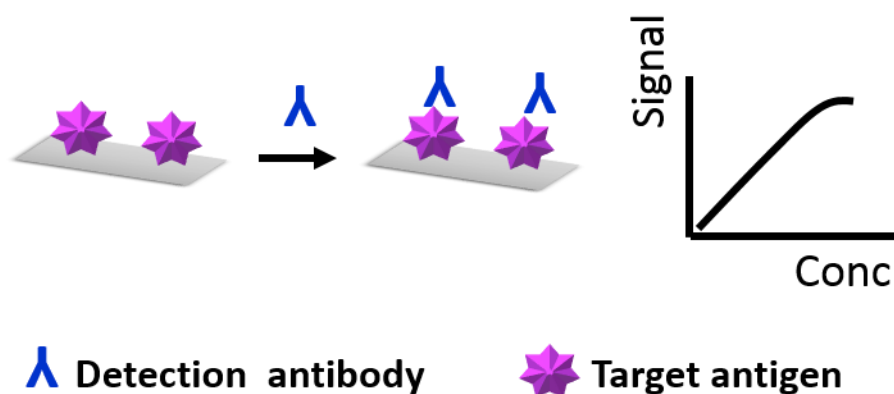
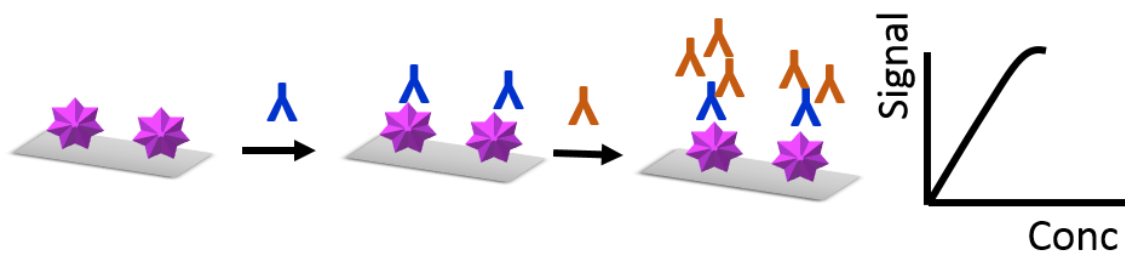


**Fig. 2-6** Diagram illustration of the immunoreaction steps leading to the final binding structures for direct immunoassay using detection antibodies.

## B. Indirect immunoassay

For indirect immunoassay, the protocol is similar with direct immunoassay with one more additional step of polyclonal antibodies. Therefore, the immobilized antigen is detected with two types of antibodies. The non-labeled primary antibody is first added to specific bind with antigen. Then, the labeled secondary antibody is added for binding with the primary antibody (Fig. 2-7). The type of secondary antibody that often used is a polyclonal antibody. This indirect format is mostly used for ELISA because (i) secondary antibody can widely use for binding with many kinds of primary antibody, (ii) the sensitivity can be enhanced via the signal amplification from the several binding sites of the secondary antibody on several epitopes of the primary antibody. However, this immunoassay model has some disadvantages about the prolongation of detection time due to one more addition step and the non-specific signal due to the cross-reaction of the secondary antibody.

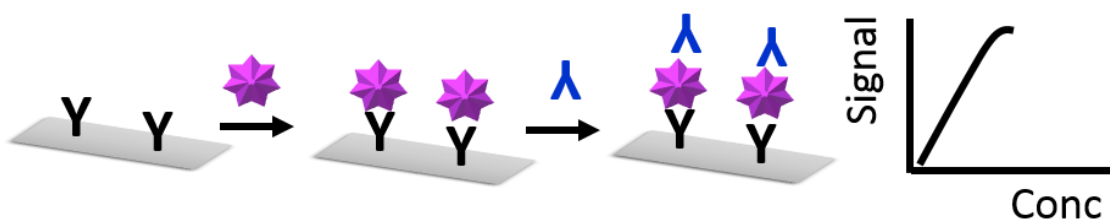


**Y** Detection antibody **Y** Polyclonal antibody **☆** Target antigen

**Fig. 2-7** Diagram illustration of the immunoreaction steps leading to the final binding structures for indirect immunoassay using polyclonal antibodies as secondary antibodies.

### C. Sandwich immunoassay

Sandwich immunoassay consists of one antigen and two antibodies, which has high antigen specificity. The antigen is sandwiched between two antibodies. The first antibody, namely capture antibody, is firstly immobilized on the substrate. Then, the antigen is injected for binding with capture antibody. Next, another antibody (detection antibody) is added to bind with antigen. These two antibodies are bound to an antigen with different epitope. The signal is measured from the secondary antibody [23]. The signal of detected secondary antibody corresponds to the concentration of target antigen. The reaction steps in the sandwich immunoassay are shown in Fig. 2-8. The advantages of this platform are high specificity, suitable for complex samples, e.g., crude, blood without purification process.



**Y** capture antibody **Y** Detection antibody **☆** Target antigen

**Fig. 2-8** Diagram illustration of the immunoreaction steps leading to the final binding structures for sandwich immunoassay using capture and detection antibodies.

#### D. Competitive immunoassay

The competitive immunoassay or inhibition immunoassay is the competitive reaction between the target antigen and labeled antigen to bind to the primary antibody that immobilized on the substrate. Firstly, the primary antibodies are immobilized on the substrate to selectively bind with the target antigen. Then, the fixed amount of labeled antigen and variable amount of target antigen are mixed. The mixed solution is dropped and incubated on the substrate, leading to antigen-antibody complexes formation. At this step, the labeled antigen and target antigen compete to bind with the primary antibody. Then, the unbound labeled antigen and target antigen are washed away by washing process [23]. Figure 2-9 shows the immunoreaction steps leading to the final binding structures of competitive immunoassay. The signal from labeled antigen after bind primary antibody is measured, which is represent the total amount of labeled antigen and target antigen. As the concentration of target antigen increases, less amount of labeled antigen can bind to antibody and the measurable signal decreases. The lower signal of labeled antigen, the higher concentration of target antigen. The calibration curve of this immunoassay has a negative slope, which is drawn in Fig. 2-9. This immunoassay format is suitable for detecting target antigen from complex samples due to its high specificity. However, this format is not commonly used because it is complicated.

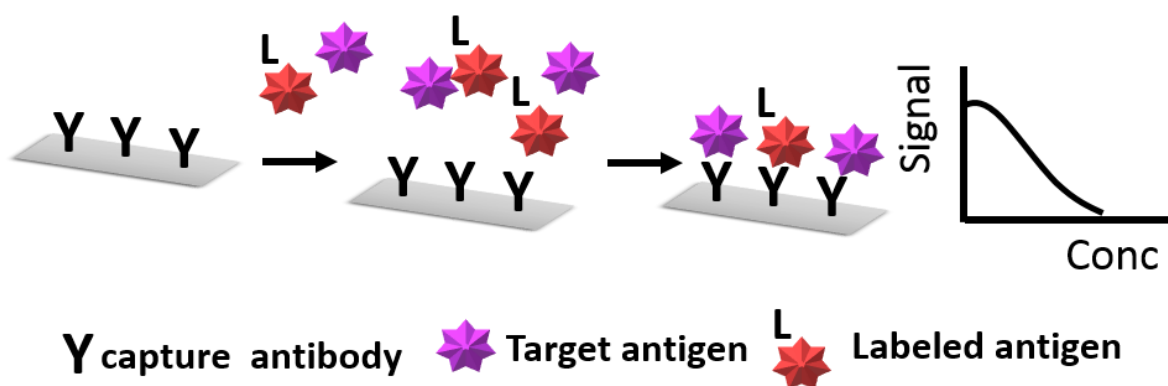


**Fig. 2-9** Diagram illustration of the immunoreaction steps leading to the final binding structures for competitive immunoassay using labelled antigens.

### 2.2.3 Transducers for immunosensors

Transducers are the devices to convert the signal generated from the formation of antigen-antibody complexes to a measurable signal. There are three main types of transducers have been applied in immunosensors, such as electrochemical, piezoelectric, and optical transducers. The basic of different transducer techniques employing in immunosensors are given below.

#### A. Electrochemical transducers

The electrochemical transducers are combined with the immunosensors to convert the event of antigen-antibody recognition into electrical signals, such as the change of current, potential, and electrical conductivity [24]. Since the immunoreaction are detected near the surface of electrodes, electrodes play an important role in the performance of electrochemical immunosensors. In electrochemical detection, three kinds of electrodes are required: a working electrode, a reference electrode, and a counter electrode [25]. The working electrode uses as transduction element, where the recognition between antigen and antibody occurs. The reference electrode, typically made from Ag/AgCl, has stable and known electrode potential. The counter electrode establishes electrical potential connected to the working electrode. The main electrochemical transducers applied in immunosensors are amperometric (measuring of current), potentiometric (measuring of voltage or potential difference between the working electrode and reference electrode), and conductimetric transducers (measuring of conductivity or resistance). Figure 2-10 shows an example of electrochemical immunosensor for detection of *P. falciparum* histidine-rich protein related to malaria using magnetic nanoparticles-coupled graphite-epoxy composite as a working electrode and Ag/AgCl electrode as a reference electrode [26]. The immunoassay for malaria was performed by adopting sandwich immunoassay on the working electrode. IgM monoclonal antibodies were used as capture antibodies deposited on the working electrode and IgG antibodies labeled enzyme horseradish peroxidase (HRP) were served as detection antibodies. Based on the redox reaction of HRP enzyme after adding hydrogen peroxide, the electrochemical signal was detected, which corresponds to the amount of *P. falciparum* histidine-rich protein. This electrochemical immunosensor shows detection limit of 0.36 ng/mL. Electrochemical detection has the potential for applying in the detection of diseases because of its advantages, such as simple, low cost, and non-destructive detection. However, this detection

method has suffered from a lack of surface architecture of working electrode for improving sensitivity and specificity [27]. Therefore, the integration of nanotechnology with working electrode offers a possible way to improve the sensitivity of detection.

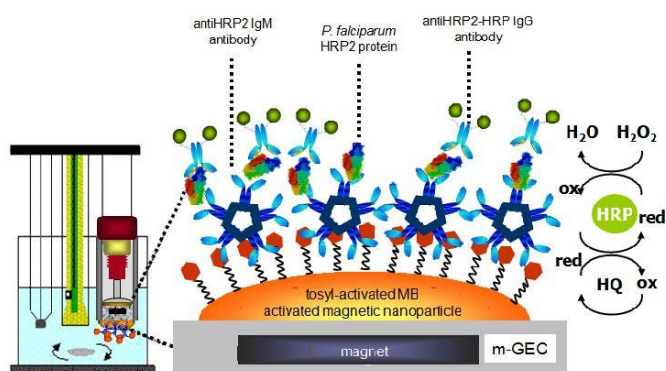


**Fig. 2-10** Schematic illustration of the electrochemical detection of sandwich immunoassay for detection of *P. falciparum* histidine-rich protein.

## B. Piezoelectric transducers

Piezoelectric transducers can directly detect the change of mass during the immunoreaction between antigen and antibody occurs. Piezoelectric transducers are used in immunosensors, such as microcantilevers and quartz crystal microbalances. For this transducer, the antibody is immobilized on the surface of piezoelectric substrates and the antigen in the solution is capture by immobilized antibody. These antigen-antibody complexes are detected as resonant frequency shift, which is sensitive to the mass changes on substrates [28,29]. An example of piezoelectric immunosensor performed on microcantilever is shown in Fig. 2-11 [30]. The first piezoelectric immunosensor was originated by Shons et al [31] to detect bovine serum albumin (BSA) using 9 MHz piezoelectric crystal. They succeeded in detecting BSA in short detection time with good sensitivity comparable to the conventional technique of passive agglutination, which required many hours for detection. Piezoelectric immunosensors have been further developed for detection of meaningful analytes, such as microbial pathogen [32-34], immunoglobulin [35], and human chronic gonadotropin (hCG) [36]. Piezoelectric immunoassays have been performed with high sensitivity and without labeling molecule and secondary

antibodies. However, nonspecific adsorption may possibly happen, which interferes with the target antigen signal and reduce the reliability of the detection [37]. The development to eliminate the nonspecific adsorption from piezoelectric immunoassays is still required. The modification of the immobilization processes may improve the sensitivity and selectivity of the sensor.

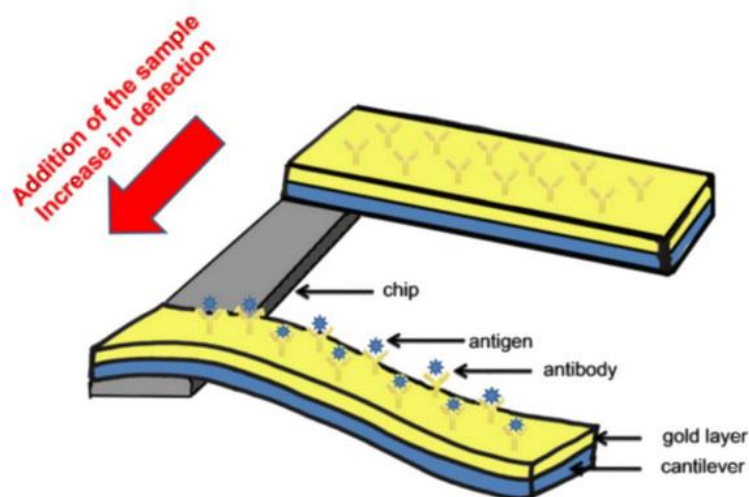


**Fig. 2-11** Schematic illustration of microcantilever immunoassay. The formation of the antigen-antibody complexes provokes a surface stress and, consequently, a deflection of microcantilever, which is detected optically.

### C. Optical transducers

Optical transducers are used to convert the light interacted with biological elements to the electronic signals. In the optical immunosensors, the biomolecules are immobilized on the surfaces connected to the transducer and the interaction between antigen and antibody is detected by the change of optical signals, such as absorbance, reflectance, emission, refractive index. Optical signals are collected by the photodetector and converted to electrical signals. There are many kinds of optical signals/phenomena employed in the optical immunosensors, which are summarized in Table 2-1 [38]. Optical detections can be classified into two types regarding the direct and indirect detection of antigen-antibody recognition [39]. The direct (label-free) detections directly measure the signal generated from the antigen-antibody interaction. The label molecules are not required in these methods. These techniques are limited to detect the small biomolecules. They have suffered from the non-specific adsorption of the biomolecule. The main types of transducers available for

direct optical detections are surface plasmon resonance (SPR), grating-couplers, and Mach-Zehnder interferometers [40-42]. The mostly used transducer employed in direct optical immunoassays is SPR because of its high sensitivity. The SPR immunosensor has been developed to directly detect the antigen binding to an antibody immobilized on the SPR sensor surface, which is capable of detecting target antigen in a complex biological fluid with highly sensitive, specific and repeatable detection. The target antigen is detected through the shift of SPR angle [43]. The SPR immunosensor has been developed for detection of low antigen concentration as well as real-time monitoring. However, this signal interferes from an artifactual change of refractive index, which is the false-positive signal.

In the case of indirect optical detections, the labeling process of label molecules on the antigen or antibody is required. The signal from the labels is proportional to the amount of the target analytes in the samples. These label detections can improve the sensitivity and specificity of the sensors. The transducers exploited in the indirect optical detections are fluorescence and SERS. The most widely used optical immunosensor to realize protein detection with high sensitivity is the fluorescence immunosensor, which employs the fluorescent-labeled antibody to recognize the target antigen [44]. The amount of antigen can be determined by measuring the fluorescent signals of the fluorescent molecules. The fluorescence immunoassays are rapid and high sensitive detection method. However, there has been reported some disadvantages, such as rapid photobleaching of fluorescent molecule, and activity loss of biomolecule upon the chemical interaction with a fluorescent molecule [45]. To overcome the disadvantages of fluorescence detection, SERS has been employed as a transducer in the immunosensors. SERS employs Raman reporter molecule labeled-metal nanoparticles (MNPs) decorated with antibodies (SERS probes) as Raman signal generators. Raman reporter molecules provide advantages over the fluorescence labels, such as no photobleaching and 10-100 times narrower spectral width [8]. Recently, SERS-based immunosensors have attracted much attention due to its high sensitive detection through the electromagnetic field enhancement from metal nanostructures [46]. This SERS readout technique has the potential to detect antigen up to a single molecular level. Among other transducers for immunoassay, SERS shows many merits, such as inherent molecular specific, high sensitive, and rapid detection, over other detection techniques. Based on the advantages of SERS, the fabrication and demonstration of highly sensitive immunoassay adopting SERS as a readout technique have been reported in this dissertation. The background information of SERS immunosensors is described in the next section.

**Table 2-1.** Optical signal/phenomena employed in optical immunosensors.

<b>Optical signal/property</b>	<b>Transducing technique</b>
<b>Absorbance</b>	Light intensity measurement
<b>Reflectance</b>	Light intensity measurement
<b>Fluorescence</b>	Total internal reflection fluorescence
<b>Refraction index</b>	Interferometry
	Surface plasmon resonance (SPR)
	Total internal reflection
<b>Optical path</b>	Interferometry
<b>Spectroscopies</b>	Surface-enhanced Raman scattering (SERS)

### **2.3 SERS-based immunosensors**

The SERS-based immunosensor is the combination between the immunosensor device and the surface-enhanced Raman scattering (SERS) readout technique. SERS immunosensors are used in the detection of various biological samples, such as urine, plasma, etc. In SERS immunosensors, the signal of the antigen-antibody recognition is enhanced by the electromagnetic field enhancement of the metal nanostructures. By taking the advantage of both immunoassay (high reaction affinity) and SERS (high signal enhancement), the SERS immunoassay has been developed to perform the high sensitive and selective detection technique. Typically, SERS-based immunosensors were classified into two types: intrinsic and extrinsic immunosensors.

#### **2.3.1 Intrinsic SERS immunosensors**

In the intrinsic detection, Raman scattered light from bioanalyte is directly detected with the help of the electromagnetic field enhancement effect of SERS. The detected signals are relatively straightforward for the target molecules. Intrinsic detection is suitable for the detection of molecules has a small number of vibrational modes, such as small protein, lipids, and DNA [8]. For instance, the detection of DNA on gold nanoshell deposited glass substrate [47], a protein linked between AgNPs [48], and bombesin, tumor marker, adsorbed

AgNPs [49] were achieved. The illustrations of intrinsic SERS immunoassay performed on the metal nanostructured substrates and in a colloidal solution of gold nanoparticles (AuNPs) are shown in Fig. 2-12. The intrinsic detection has suffered from the detection of large molecules and complex systems that contain a lot of biomolecules. Since different kinds of proteins have common basis components, their Raman spectra should contain similar vibrational bands, e.g. COO<sup>-</sup> stretch at 1400 cm<sup>-1</sup>, aromatic NH<sub>2</sub> at 950 cm<sup>-1</sup>, broad amide (CO-NH) I and III bands at 1600-1700 cm<sup>-1</sup>, and 1200-1350 cm<sup>-1</sup> [8]. Therefore, it is difficult to make a distinction between different kinds of proteins (biomolecules) from the Raman spectra.

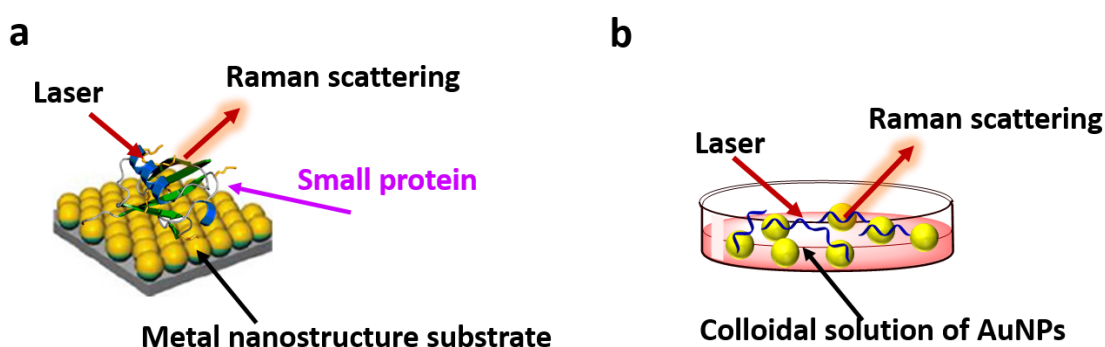


**Fig. 2-12** (a) Intrinsic SERS immunoassay of small protein adsorbed on metal nanostructure substrate, and (b) intrinsic detection of DNA in colloidal solution of gold nanoparticles.

### 2.3.2 Extrinsic SERS immunosensors

Extrinsic SERS immunosensor has been developed to overcome the limitation of intrinsic SERS immunosensor, in which a target bioanalyte labeled with a Raman reporter molecule that has unique vibrational fingerprints is used. In general extrinsic detection methods, target bioanalytes are first immobilized on substrates, and then SERS probes containing Raman reporter molecules are selectively immobilized on the target bioanalytes. The existence of bioanalytes is indirectly recognized by detecting the signal from the Raman reporter molecules. Therefore, this extrinsic detection can be applied to complex systems that contain a lot of biomolecules.

In the first generation of extrinsic detection, the immunoassay reaction was performed on flat substrates, e.g. Au or glass substrates [50,51]. Since no electric field enhancement can be expected from such a flat substrate, the enhancement of Raman signal comes from the electromagnetic field enhancement effect

of the center metallic NPs composing SERS probes and/or from that due to plasmonic coupling among SERS probes. The illustration of extrinsic SERS immunoassay on a flat substrate is shown in Fig. 2-13. There are two strategies for improving the sensitivity of extrinsic detection. One is the structure design of SERS probes; for instance, higher electromagnetic field enhancement can be obtained by using Au nanoflowers, Au nanostars, or aggregates of AuNPs as the center metallic NPs of SERS probes, instead of sphere-shaped AuNPs [52]. Another strategy is the use of a nanostructured metallic substrate (SERS substrate) instead of a flat substrate. By properly designing the SERS substrate, significant improvement in the sensitivity can be expected through strong plasmon coupling between SERS substrates and SERS probes. According to these strategies, some groups reported good achievements on SERS biosensors. Kaminska and coworkers [53] reported a microfluidic SERS immunosensor for Hepatitis B virus detection, where an Au/Ag-coated GaN substrate was used as a SERS-active substrate and basic fuchsin-adsorbed Au nanoflowers were used as SERS probes. This system reveals good performance with high specificity and low detection limit about 0.01IU/mL. Pei and coworkers [52] achieved high sensitive SERS immunoassay by using self-assembled gold nanostars substrate as a SERS substrate and aggregates of gold nanostars as SERS probes. The low detection limit about 10 fg/mL was obtained for immunoassay of anti-goat human IgG and human IgG. Such a very low detection limit of this model may be caused by the strong plasmonic coupling between the SERS probe and substrate [46]. Therefore, the development of SERS substrates that can be electromagnetically coupled with SERS probes and also that shows high reproducibility is crucial for realizing high sensitive biosensors.

Since extrinsic SERS immunosensors consist of two important components: SERS probe and substrate, the general information of these materials were briefly explained as follows.

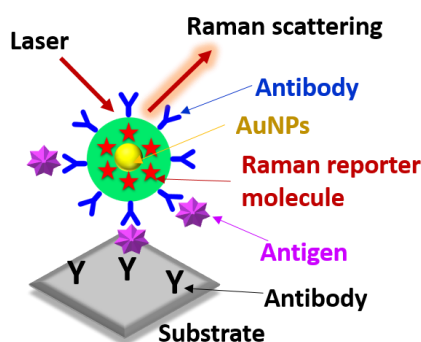


**Fig. 2-13** Illustration of extrinsic sandwich-type SERS immunoassay performed on flat solid substrate.

## A. SERS probes

SERS probes are noble MNPs loaded with Raman-active molecules, which has high and distinctive vibration fingerprint, for identifying bio-targets using their own inherent Raman fingerprint. Typical SERS probes consist of MNPs, Raman reporter molecules, protecting shell, and specific targeting molecules [54,55]. The MNPs act as SERS-active support for Raman reporter molecule. These particles are the biocompatible materials that mostly applied for biomedical applications. Raman reporter molecules are the thiolated molecules that can chemisorb on the MNPs and produce strong and unique Raman spectra. The typical Raman reporter molecules are listed in table 2-2. Protecting shell, used for MNPs stabilization and avoided desorption of Raman reporter, has many kinds of chemical, such as  $\text{SiO}_2$ ,  $\text{TiO}_2$ , polymer. These chemicals are able to decorate with a biomolecule (antibody, DNA, and aptamer) for selective binding with target analytes [56]. The general steps of SERS probe synthesis and design are shown in Fig. 2-14 [57]. Briefly, the MNPs with desired particle size, shape and LSPR is selected. Then, the MNPs are labeled with Raman reporter molecules via the metal-S bond. These particles are stabilized by coating with polymers. Finally, the antibodies are immobilized on the particles via covalent bonds. The SERS probes should have large effective Raman cross-section with the selective binding ability to a target bio-analyte and sufficient stability in air and aqueous solution. By designing metallic NPs properly, the scattering efficiency of Raman reporter molecules can be strongly enhanced via LSPR of the MNPs. Using biocompatible SERS probes, the extrinsic detection can be applied to cellular and in vivo sensing: e.g. local pH mapping in cell and detection of cancer markers in a live cell [54,8,58].

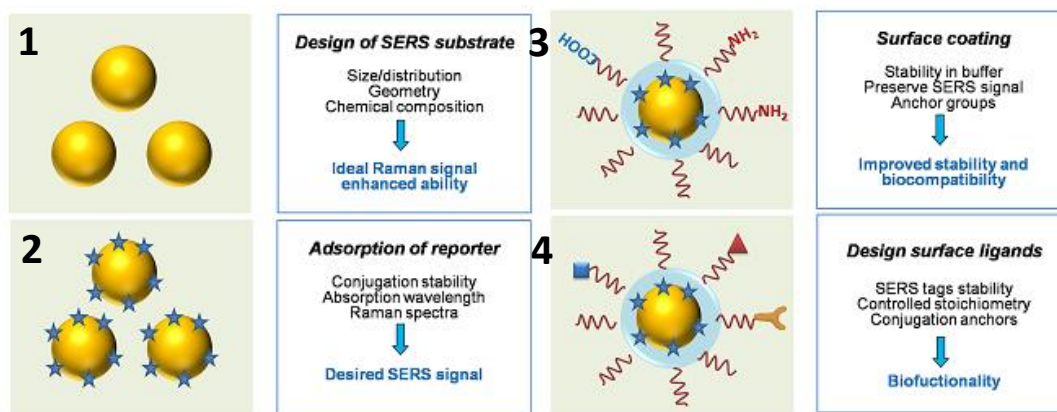


**Fig. 2-14** General steps and designs of SERS probes for biomedical applications.

**Table 2-2** Typical Raman reporter molecule in SERS probe synthesis

Type	Example	Linking mode	Advantages	Disadvantages
<b>Cationic dye</b>	Rhodamine 6G	N-Au or Ag	-Cheap	- Weak bonding to metal
	Nile blue	(electrostatic force)	-Large Raman cross-section	
<b>Thiol molecule</b>	4-mercaptobenzoic acid	S-Au or Ag	-Cheap	- Small Raman cross-section
	4-aminothiophenol		-Strong bonding to metal	
	4-thionitrophenol			
<b>Thiol dye</b>	Malachite green	S-Au or Ag	-Large Raman cross-section	- Difficult to form SAMs
	isothiocyanate			
	Rhodamine-5-(and-6)-isothiocyanate		-Strong bonding to metal	

## B. SERS substrates

SERS substrates are the metal nanostructured substrates, which mostly fabricated from silver (Ag) and gold (Au). The large electromagnetic field enhancement could be obtained from SERS substrates when the LSPR of substrates is properly matched with the wavelength of excitation laser [59,60]. SERS substrates can be fabricated by using various kinds of fabrication processes, such as lithography [61], self-assembled monolayer [62], electrochemical deposition, atomic layer deposition [63], laser printing, and nanoimprinting technique. The lithography and atomic layer deposition require high cost, the skilled person, but it shows the uniform size and shape. On the other hand, a self-assembled monolayer is easy to handle and cheap, but uncontrollable size and shape are found. Figure 2-15 shows the scanning electron microscope images of some SERS substrates fabricated using various kinds of the fabrication processes, such as (a) metal film deposited over nanosphere [64], (b) metal island deposited on sphere mask [63], (c) two-dimensional (2D) array by electron beam lithography [61], and (d) 2D nanoholes by atomic layer deposition[64], and (e) self-assembled monolayer of AuNPs capped alkanethiol [62].

The ideal SERS substrate for all kinds of applications should possess high uniformity, high field enhancement, reproducible SERS enhancement, stable, and biocompatibility [65]. In past few decades, the SERS substrates have been employed for amplifying the signals in immunoassays. In the case of SERS substrate for immunoassay, it not only shows the strong electromagnetic field enhancement but also presents the chemical group for chemically binding with a biomolecule. The use of SERS substrate in immunoassays offers a great promise for trace amount detection with high sensitivity [66,67].

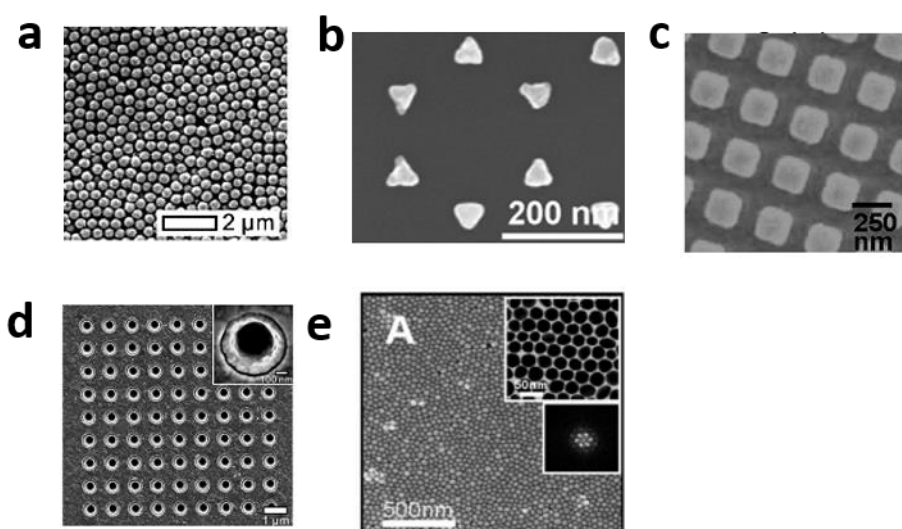


**Fig. 2-15** Scanning electron microscope image of various SERS substrate fabrication process. (a) metal film deposited over nanosphere [64], (b) metal island deposited on sphere mask [63], (c) 2D array by electron beam lithography [61], and (d) 2D nanoholes by atomic layer deposition [64], and (e) self-assemble monolayer of AuNPs capped alkanethiol [62].

## CHAPTER III

### EXPERIMENTAL

The chemicals, biomolecules, the characterization equipments and the characterization methods employed in this research are described in this chapter. The chemicals and biomolecules are given in the first part. The molecular structures of some chemicals are shown in Fig. 3-1. Next, the preparation of substrates (gold (Au) and indium tin oxide (ITO)), gold nanoparticles (AuNPs), gold core@silver shell nanoparticles (Au@Ag core-shell NPs), and hydrophilic SERS substrates are explained. Then, the instruments and the measurement conditions are described. Finally, the characterization methods of SERS immunosensor are described.

#### 3.1 Chemicals and biomolecules

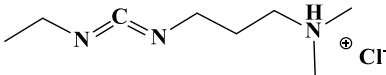
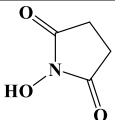
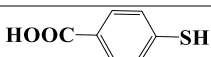
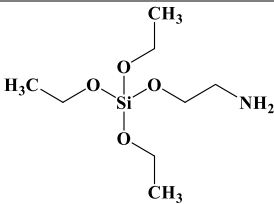
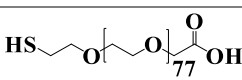
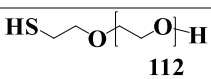
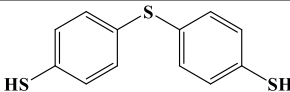
Chloroauric acid ( $\text{HAuCl}_4$ ), 4,4'-thiobisbenzenethiol (TBBT), 1-ethyl-3[3-dimethylaminopropyl] carbodiimide hydrochloride (EDC), N-hydroxysuccinimide (NHS), mercaptohexadecanoic acid (MHDA), mercaptobenzoic acid (MBA), polyoxyethylene (20) sorbitan monolaurate (Tween 20), disodium hydrogenphosphate ( $\text{Na}_2\text{HPO}_4$ ), potassium dihydrogenphosphate ( $\text{KH}_2\text{PO}_4$ ), and sodium chloride (NaCl) were obtained from Sigma-Aldrich. Silver nitrate ( $\text{AgNO}_3$ ), sodium citrate, ascorbic acid, dodecanethiol, and octadecanethiol were purchased from Nacalai tesque. Polyethylene glycol methyl ether thiol (PEG-SH, MW 5,000 Da), and polyethylene glycol 2-mercaptoethyl ether acetic acid (COOH-PEG-SH, MW 3,400 Da) were obtained from Nanocs, Inc. Bovine serum albumin (BSA) was purchased from Wako. The commercially available chemicals were used without further purification. *Phosphate buffered saline* (PBS) solution was prepared by mixing  $\text{Na}_2\text{HPO}_4$ ,  $\text{KH}_2\text{PO}_4$ , and NaCl: one liter of 10 mM PBS solution includes 2.17 g of  $\text{Na}_2\text{HPO}_4$ , 0.26 g of  $\text{KH}_2\text{PO}_4$ , 8.71 g of NaCl. Distilled water (18.2 M $\Omega$ . cm) was used in all experiment.

For influenza A detection, a monoclonal antibody specific to influenza A nucleoprotein was purchased from Innova Biotechnology and used without further purification. The allantoic fluid infected with Influenza A/Thailand/104/2009 (H1N1) (Prof. Pilaipan Puthavathana, Mahidol University, Bangkok, Thailand) was prepared and inactivated as described [68]. The recombinant nucleoprotein used in this study was generated and characterized as described previously [69]. For dilution of the infected allantoic fluid, an extraction buffer

solution (150 mM NaCl, 5 mM EDTA, 16 mM Triton X-100, 12 mM sodium deoxycholate, and 3.5 mM SDS in 10 mM phosphate buffer pH 7.4) was used as the solvent.

For immunoglobulin G (IgG) detection, Goat anti Human-IgG (# 31119, Mw 150 kDa) was purchased from Thermo scientific. Purified human-IgG (# P80-105, Mw 150 kDa) was bought from Bethyl laboratories, Inc. For prostate specific antigen detection, monoclonal capture antibody to PSA (clone M12619PS1, # 10-P142A, Mw 150 kDa), monoclonal detection antibody to PSA (clone M18612PS4, # 10-7948, Mw 150 kDa), and PSA antigen (clone A15052982, # 30C-CP1017U, >98% pure, Mw 30 kDa) were provided by Fitzgerald.

**Fig. 3-1** Molecular structures of chemicals

Chemical name	Molecular structure
<b>1-ethyl-3[3-dimethylaminopropyl] carbodiimide hydrochloride (EDC)</b>	
<b>N-hydroxysuccinimide (NHS)</b>	
<b>Mercaptohexadecanoic acid (MHDA)</b>	
<b>Mercaptobenzoic acid (MBA)</b>	
<b>Aminopropyl trimethoxysilane (APTES)</b>	
<b>Thiolated PEG carboxylate; HS-PEG-COOH (MW = 3,400 Da)</b>	
<b>Thiolated PEG; HS-PEG (MW = 5,000 Da)</b>	
<b>4, 4'-thiobisbenzenethiol (TBBT)</b>	

## 3.2 Sample preparation

### 3.2.1 Substrates

**ITO substrate:** 0.6 mm-thick quartz were used as a substrate with 1cm×1 cm. Substrates were immersed in piranha solution (30% H<sub>2</sub>SO<sub>4</sub>/H<sub>2</sub>O<sub>2</sub>=2:1 v/v) for cleaning organic matter on the substrate and rinsed with milli-Q water three times. Then substrates were coated with ITO by radio frequency sputtering deposition at room temperature. Before functionalized substrate, UV-ozone cleaning was done for 3 h (final bulk resistivity of 1.1×10<sup>-3</sup> Ω.cm), followed by immersing in 1% (v/v) solution of 3-mercaptopropyltrimethoxysilane in toluene for 40 h, rinsed with toluene and methanol three times. Ultimately, substrates were immersed in 1% (v/v) solution of 1, 6-hexanedithiol in ethanol for 12h, rinsed with isopropanol three times and dried with N<sub>2</sub> stream.

**Au substrate:** Before Au film deposition, 0.6 mm-thick quartz substrates were immersed in piranha solution to remove organic matter and then rinsed with milli-Q water three times. A 10 nm-thick Cr adhesion layer and a 40 nm-thick Au film were sequentially deposited on the quartz substrate by thermal evaporation in a vacuum (<10<sup>-4</sup> Pa). The deposition rate of both Cr and Au was 0.1 nm/s.

### 3.2.2 Citrated-capped AuNPs

Citrate-capped AuNPs of different sizes were synthesized by a seed-mediated growth method [62]. Firstly, a colloidal solution of Au seeds of 13 nm in diameter was synthesized as follows; 20 mL of a 0.5 mM aqueous solution of HAuCl<sub>4</sub> was refluxed, and then 1 mL of a 38.8 mM aqueous solution of sodium citrate was added to the boiling solution; and the solution was refluxed for 30 minutes at 120°C to complete the reaction. Next, AuNPs of different particle sizes were synthesized as follows; the colloidal solution of Au seeds, whose volume was varied depending on the target particle size as listed in Table 3-1, was mixed with 34 mL of deionized (DI) water in a vessel while stirring constantly; then 0.8 mL of a 20 mM aqueous solution of HAuCl<sub>4</sub> and 80 μL of a 10 mM aqueous solution of AgNO<sub>3</sub> were added in series; after the solution was mixed for a few minutes, 6 mL of a 5.3 mM ascorbic acid aqueous solution was added with a constant feeding rate of 0.61 mL/min; to complete the reduction, the solution was stirred for 5 min after the addition of ascorbic acid solution; and then a solution of citrate-capped AuNPs was obtained.

**Table 3-1.** Amount of colloidal solution of Au seeds used for synthesizing AuNPs of different sizes.

Diameter of AuNPs (nm)	13 nm-Au Seed solution (mL)
26	5.0
31	3.0
42	1.3
53	0.6
77	0.2
110	0.1

### 3.2.3 2D arrays of 42Au@Ag core-shell NPs

The SERS substrates used in this study are 2D arrays of Au@Ag NPs formed on ITO substrates. First, Citrate-capped Au@Ag core-shell nanoparticles were synthesized as follows [70]. 15 mL of 42 nm gold colloidal solution prepared according to the recipe described in the previous section was added to 13 mL of water containing 1.2 mL of 10 mM ascorbic acid, then a 1.2 mL of 5 mM AgNO<sub>3</sub> solution was added with feeding rate of 0.4 mL/min. After completely adding AgNO<sub>3</sub>, the solution was continuously stirred for 5 minutes to complete reaction. The Au core diameter and the Ag shell thickness were determined to be 42 nm and 5 nm, respectively. The structure of Au@Ag NPs was designed so that the LSPR energy of 2D Au@Ag NP arrays matches the excitation wavelength (633 nm) of the Raman measurement in this study. Then, alkanethiolate-capped Au@Ag NPs were synthesized according to the procedure reported previously,[70] except for using a mixed solution of octadecanethiol: dodecanethiol = 1:6 (molar ratio) in acetone [71] for the mixed self-assembled monolayer (SAM) formation on the Au@Ag NP surface. The details of Au@Ag NP synthesis were described below. The citrate-capped Au@Ag NPs were thiolated as follows. A mixed solution of dodecanethiol and octadecanethiol in acetone was prepared at a molar ratio of dodecanethiol:octadecanethiol = 6:1 and at a total alkanethiol concentration of 11.3 mM. 10 mL of this mixed alkanethiol solution was gradually added to 10 mL of the citrated Au@AgNPs colloidal solution while stirring. Then, this stirring was continued at RT overnight, until the solution became clear and Au@Ag NPs were floated. To collect mixed-alkanethiolate-capped Au@Ag NPs, a mixture of acetone and n-hexane was added to the colloidal solution. The thiolated Au@AgNPs concentrated at the interface between the hexane and acetone/water layers were collected with a pipette. This collection process was performed repeatedly until no Au@Ag NPs appeared at the interface. The collected particles were washed by three cycles of centrifugation and redispersion into a

mixture of acetone and n-hexane; the acetone/hexane ratio was sequentially varied: 10:0, 1:9, and 0:10. After the supernatant was discarded in the final washing cycle, the Au@Ag NPs were dried under a nitrogen atmosphere. Before arraying process, the powder of Au@Ag NPs was redispersed in 2 mL of a mixture of hexane-acetone (4:1 v/v).

The alkanethiolate-capped Au@Ag NPs were arrayed on an ITO substrate by a hybrid method, in which uniform and high coverage 2D arrays of metallic NPs are formed through solvent-evaporation-induced self-assembly under the presence of electric field.[72,73] Before arraying Au@Ag NPs, the ITO substrate was successively functionalized with 3-mercaptopropyl trimethoxysilane (MPTMS) and 1,6-hexanedithiol. The colloidal solution of mixed alkanethiol-capped Au@Ag NPs redispersed in 2 mL of a mixture of hexane-acetone (4:1 v/v) was added into a vessel. A thiolated ITO substrate and a plastic formed carbon electrode were immersed into the vessel and used as a cathode and an anode, respectively. The distance between these electrodes was set at 1.2 mm. The Au@Ag NPs immobilized on thiolated ITO substrate after applying a voltage of 1 V at room temperature under nitrogen environment. The arraying of Au@AgNPs was completely done after solvent entirely evaporated. Afterward, the 2D array samples were annealed at 60°C overnight to enable chemisorptions of Au@Ag NPs on the functionalized ITO substrate, and then washed by sonication in hexane for 30 s to remove excess of Au@Ag NPs.

#### **3.2.4 Hydrophilic SERS substrate**

Since the 2D array substrate obtained by this method is hydrophobic, it is not suitable for immunoassays. Thus, the 2D array substrate was hydrophilized by exchanging the capping molecules with MHDA. First, the 2D array substrate was annealed at 90°C for 1 h. We believe that most of alkanethiolate molecules adsorbed on the upper half (air side) of Au@Ag NPs are desorbed during this annealing. Then the substrate was immersed in an ethanolic solution of MHDA (15 mM) for 12 h at 50°C. The substrates were rinsed with ethanol three times and dried under a nitrogen atmosphere.

### 3.2.5 Activation of SERS substrate

Before utilizing the hydrophilic SERS substrate as the solid support for immunoassay, the activation of carboxyl portion of MHDA molecule for further interaction with biomolecule was performed by using the mixture of EDC-NHS crosslinking molecules. The freshly prepared hydrophilic SERS substrate was activated by successively dropping 10  $\mu\text{L}$  of a 15 mM EDC aqueous solution and 10  $\mu\text{L}$  of a 15 mM NHS aqueous solution. The mixed droplet was kept on the substrate for 30 min in the dark chamber. Then, the substrate was washed with distilled PBS solution three times and dried by nitrogen gas. The mechanism of the reaction between the carboxyl group and EDC/NHS crosslinking molecules is shown in Fig. 3-2.

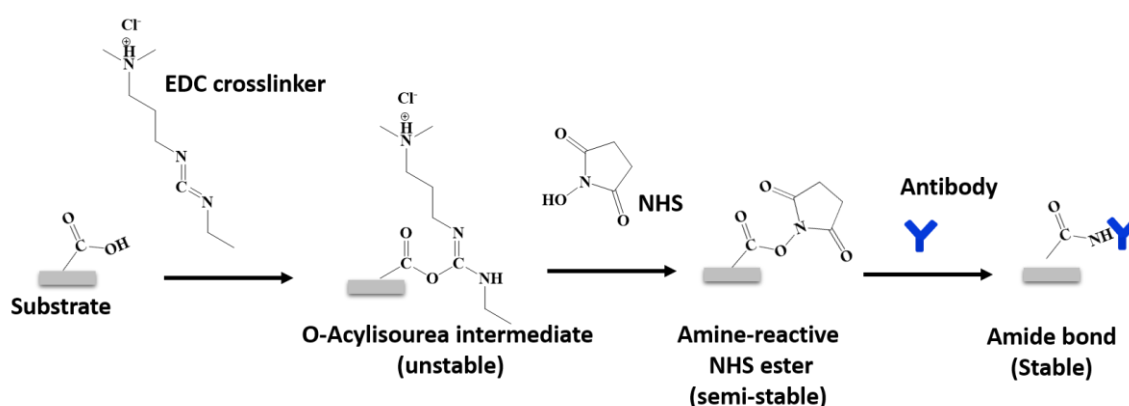


**Fig. 3-2** Schematic mechanism of carboxyl group activation by EDC/NHS.

### 3.3 Instruments

The morphology of AuNPs was characterized by SEM, TEM, and EDX. SEM images were obtained with FE-SEM S-4800 (Hitachi, Japan) to evaluate the morphology and coverage of particles on the substrate with an accelerating voltage of 5 kV. For TEM measurement, the aqueous colloidal solution of AuNPs was dropped on the copper grid and dried under vacuum. The TEM images and EDX measurements were taken using TEM HD-2000 (Hitachi) with an accelerating voltage of 200 kV.

UV-Vis-NIR spectroscopy was carried out with a V-670 spectrometer (JASCO, Japan) to examine the optical property of nanoparticles and SERS substrates. The extinction spectra of a colloidal solution of nanoparticles were obtained by using liquid cell holder module with a path length of 10 mm. The extinction spectra of SERS substrate (Au@Ag core-shell nanoparticle deposited on ITO substrates) were measured using

a transmission module for the solid samples. The FTIR spectra of PEGylated-MBA-AuNPs, SERS probes, the reaction of the exchange capping molecule of SERS substrate from hydrophobic to hydrophilic were obtained with a FTIR spectrometer (Nicolet 4700) in an attenuated total reflection (ATR) geometry using a diamond prism.

Raman spectra were measured with a micro-Raman spectrometer system with a He-Ne laser and a charge-coupled device (CCD) detector (NT-MDT NTEGRA Spectra or Lambda Vision MicroRAM-300). For the NT-MDT NTEGRA spectra system, the excitation laser light was focused on the sample surface using a 40× objective lens with a numerical aperture of 0.65, and the Raman scattered light was collected by the same objective lens. The Raman scattered light was dispersed with a single spectrograph of a focal length of 520 nm with a grating of 1200 grooves/mm. For the MicroRAM-300 system, a 50× objective lens with a numerical aperture of 0.75 was used for the excitation and collection of Raman scattered light. A single spectrograph of a focal length of 300 nm with a grating of 600 grooves/mm was used to record Raman spectra. The photograph and optical pass of MicroRAM-300 are shown in Fig. 3-3. The laser spot size was estimated about to be 4 μm in diameter. For both Raman spectrometer systems, a 632.8 nm line of the He-Ne laser was used for excitation, and the laser power was set to 100 μW at the sample surface. Stokes Raman shift spectra were obtained with an exposure time of 50 s. To improve the signal-to-noise ratio, typically five to ten spectra were averaged.

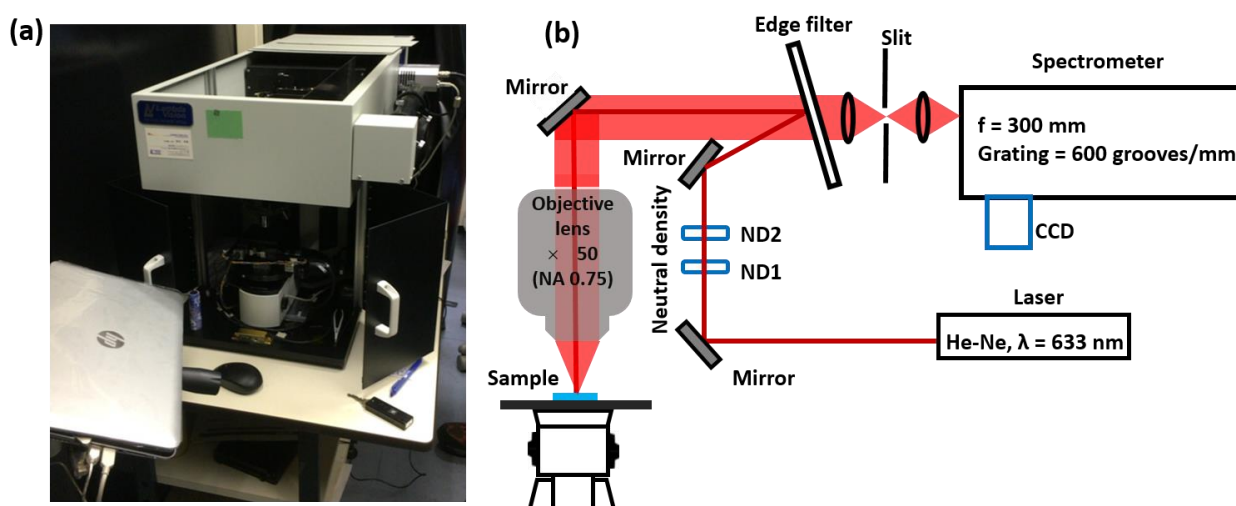


**Fig. 3-3** Photograph (a) and sketch (b) of experimental set up for the MicroRAM-300 Raman spectrometer consisted of excitation laser (He-Ne laser), optical lens (50× with a numerical aperture of 0.75), mirrors, edge filter, confocal optical microscope, and detector (CCD).

### 3.4 Characterization methods

#### 3.4.1 Calibration

Calibration curve is the standard curve for determining the concentration of target analytes in SERS immunosensor. The calibration curve is the plot of the measurable signals and concentration of analytes. Figure 3-4 shows typical calibration curve. The linear calibration curve is obtained by the method of least squares. This fitting provides much information for the quantitative analysis, such as linearity, linear equation, limit of detection, and sensitivity. Linearity shows the accuracy of the measured response to a straight line, mathematically represented as  $y=mx+c$ , where  $c$  is the concentration of the analyte,  $y$  is the observed intensity, and  $m$  is the slope. The sensitivity of the sensor is the slope of the linear calibration curve. The sensitivity is defined as the smallest change in the concentration of an analyte that is required to bring a big change in the response of the output signal. The lowest amount of analyte that can be detected by immunosensor defines its limit of detection (LOD) [74].

In this study, the linear sensitivity curve and limit of detection (LOD) can be expressed by eq1 and eq2, respectively.

$$I^{ob} = ax + b, \quad (1)$$

where  $I^{ob}$  is the observed Raman intensity, and  $x$  is the concentration of target bio-analytes. When the mean value and the standard deviation of the Raman intensity for the control sample are denoted by  $I_{control}^{ave}$  and  $\sigma_{control}$ , respectively and the standard deviation of the Raman intensity for the immunoassay at a target concentration near and higher than LOD is denoted by  $\sigma_{LOD}$ , we defined the LOD by the following equation:

$$LOD = x_{LOD} = \frac{\{I_{control}^{ave} + 1.645(\sigma_{control} + \sigma_{LOD}) - b\}}{a}. \quad (2)$$

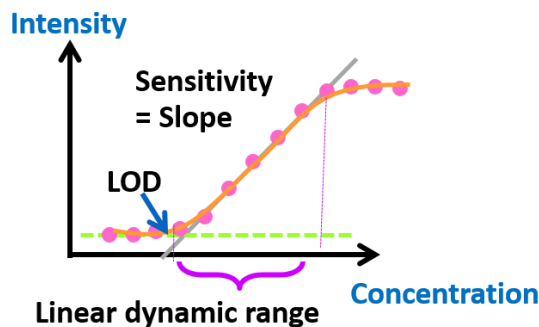


**Fig. 3-4** Typical calibration curve of immunosensor.

### 3.4.2 Selectivity

Selectivity is the performance of a sensor to detect only a specific analyte in a complex samples [74]. Fig. 3-5 shows the selectivity of the immunoassay against other proteins. Immunosensor must be able to detect only the target analyte in the complex matrix. The signal of the interference should be much lower than that of target analyte one.

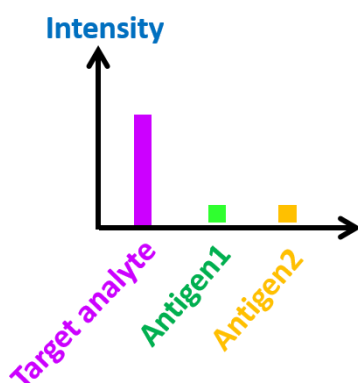


**Fig. 3-5** Typical selectivity of the immunosensor. The strong intensity was detected from target analyte while the intensities of other antigens (negative results) are weak.

### 3.4.3 Reproducibility

Reproducibility is the performance of immunosensor to generate similar signals for many replication [74]. The reproducibility is characterized by the precision and accuracy of the transducer and electronics in an immunosensor. Fig. 3-6 shows the high reproducibility of the immunosensor. The precision of reproducibility of the sensor is usually characterized in terms of the relative standard deviation (%RSD) of the replications. The %RSD, which is often expressed as a percentage, is calculated by  $\%RSD = SD / \bar{x}$ , where  $SD$  is the sample standard deviation, and  $\bar{x}$  is the mean value of the sample data. The acceptable %RSD value for the immunosensors is less than 30% of the variation within the sample replications [75].

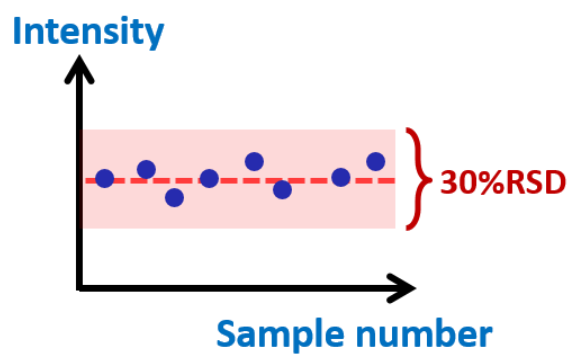


**Fig. 3-6** Typical reproducibility of immunosensor. The highlighted area represents the probability of data variation with acceptable value.

## CHAPTER IV

### DEMONSTRATION OF SURFACE-ENHANCED RAMAN SCATTERING (SERS)

#### IMMUNOASSAY FOR DETECTION OF INFLUENZA A VIRUS

The study of influenza A detection has attracted attention because it is a severe pandemic all over the world. Influenza carries a high mortality particularly in the young people (3-12 years old) [76]. Rapid and high sensitive influenza virus detection are important in terms of disease diagnosis, and point of care testing. In this chapter, an extrinsic SERS-based immunosensor for detecting nucleoprotein, influenza A antigen, and its performance were reported. In this sensor, the immunoreaction occurs on two-dimensional (2D) arrays of gold core@silver shell (Au@Ag) nanoparticles (NPs) on an ITO substrate, served as a SERS substrate to improve the sensitivity. The SERS probes were fabricated by decorating PEGylated, 4,4'-thiobisbenzenethiol (TBBT)-labeled gold nanoparticles (AuNPs) with antibodies specific to the target nucleoprotein. TBBT was chosen as a Raman reporter molecule in this SERS immunoassay because of its outstanding characteristic Raman spectra. The ~4 times sensitivity enhancement was achieved by replacing a flat Au film with a 2D array of Au@Ag NPs, whose localized surface plasmon resonance (LSPR) was tuned to the excitation laser wavelength of 633 nm. Finally, we demonstrated the applicability of our SERS immunoassay system to complex biological samples using a stock solution of Pandemic 2009 influenza A H1N1 virus-infected allantoic fluid containing  $5.6 \times 10^3$  TCID<sub>50</sub>/mL (50% tissue culture infectious dose).

First of all, the information and structure of influenza A virus are described. Then, the SERS probe synthesis, the immunosubstrate preparation, and the immunoassay protocol are explained. Next, the SERS probe and hydrophilic SERS substrate characterization, the optimization of immunoassay process, the performance of SERS immunosensing system (sensitivity, selectivity, and reproducibility), and analysis of the nucleoprotein in the infected allantoic fluid were reported. Finally, the conclusion of this topic was presented.

## 4.1 Influenza A

Influenza A is one of influenza virus types and can infect many kinds of hosts, e.g. bird, pig, horse, sheep, and human. This virus can be transmitted from one host to other hosts and may cause a severe pandemic. Influenza A virus contains 11 or 12 viral proteins, including nonstructural protein1 (NS1), matrix protein (M1), ion channel (M2), hemagglutinin (HA), neuraminidase (NA), nucleoprotein (NP), components of the RNA-dependent RNA polymerase complex (PB1, PB2, and PA), N40 protein, and pro-apoptotic protein (PB1-F2) (See Fig. 4-1) [77]. Influenza A virus has several subtypes, which are categorized by two proteins on the virus envelope: Hemagglutinin and neuraminidase. There are 18 different hemagglutinin subtypes (H1 to H18) and 11 different neuraminidase subtypes (N1 to N 11). In particular, three influenza subtypes (H1N1, H2N2, and H3N2) can be circulated among human.

The last pandemic, in 2009, influenza (H1N1 swine flu) outbreaks firstly happened in the United States and spread quickly across the world. The estimated number of infected people was about 43 to 89 million people. This influenza A virus has been recorded as one of the world's most dangerous pathogens because of its high viability and easy spread [78].

The traditional diagnostic methods for influenza A virus detection are based on the virus isolation from tissue cultures, or embryonated chicken eggs [79]. To obtain the effective and reliable result from these methods, several days for experiment and long analysis time are required. There are ELISA (Enzyme-linked immunosorbent assay) methods for detecting viral proteins relying on the interaction between antibody and virus antigens. This method requires many steps of reaction with long analysis time. However, the sensitivity is quite low. To obtain high sensitivity and specificity with shorter analysis time (a few hour), the molecular methods based on polymerase chain reaction (PCR), reverse transcriptase polymerase chain reaction (RT-PCR), and real-time PCR are adopted. The shortcoming of these methods is the sample preparation (isolation of genetic material from the virus without any contamination is required).

Nowadays, the commercial test ELISA-based kits of QuickVue Influenza A+B Test (Quidel, San Diego, CA, USA) for influenza detection are available by employing the reaction between antibody and nucleoprotein (is one of the most conserved and abundant structural proteins inside the virion). The structure and the binding site of nucleoprotein against monoclonal antibody are shown in Fig. 4-1 [80]. These kits are

capable of identifying influenza A H1N1 in the respiratory samples [81]. However, it should be noted that these kits are more suitable for Influenza A detection of the young patients than aged. Therefore, the improvement of a detection method for monitoring and observing the patient's condition with short analysis time is still demanded. The method bases on the multidisciplinary study of physics, chemistry, and biology may offer the good way to improve the detection performance.

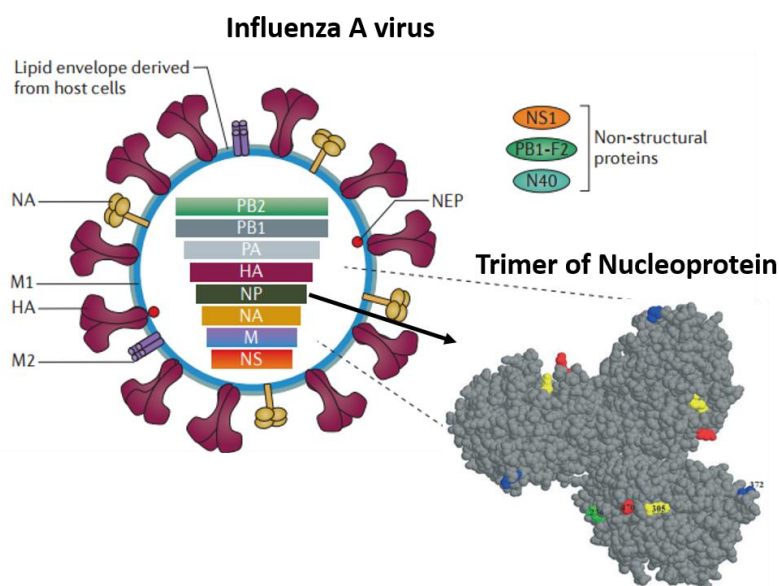


**Fig. 4-1** Structure of influenza A virus. Influenza A virus has a lipid bilayer envelope, in which there are 8 proteins (PB2, PB1, PA, HA, NP, NA, M, NS). The outer layer of lipid envelope is coated with HA, NA, M1, and N2. The zoomed view is the structure of trimer nucleoprotein. The yellow, red, blue, and green regions represent the location of amino acid residues involved in the interaction with monoclonal antibody.

## 4.2 Experimental

### 4.2.1 SERS probe preparation

SERS probes were prepared in three steps: synthesis of 25 nm citrate-capped AuNPs, modification of AuNPs with TBBT (Raman reporter) and PEG molecules, and antibody immobilization. TBBT was chosen as a Raman reporter molecule because it shows strong and outstanding Raman bands at 1077 and 1572  $\text{cm}^{-1}$  [82,83]. First, AuNPs were obtained by reducing  $\text{HAuCl}_4$  with sodium citrate. In brief, 95 mL of an aqueous solution containing 5 mg of  $\text{HAuCl}_4$  was refluxed. Then, 5 mL of 1 % (w/v) aqueous solution of sodium citrate

was added to the boiling solution. The reflux was continued for 30 min [84]. An average diameter of obtained AuNPs was  $26 \pm 2$  nm, which was determined from the SEM image (Fig. 4-2). Following the nanoparticle synthesis, AuNPs were simultaneously labeled with TBBT and thiolated PEG acid (COOH-PEG-SH) to avoid the particle aggregation and precipitation. A mixed solution of 5  $\mu$ M ethanolic solution of TBBT (1.5 mL) and 1  $\mu$ M aqueous solution of COOH-PEG-SH (1.5 mL) were freshly prepared and added to the colloidal solution of 25 nm citrate-capped AuNPs (9 mL). After 30 min incubation, 65  $\mu$ L of a 1.5 mM aqueous solution of thiolated PEG (PEG-SH) was added to the colloidal solution, and then further incubation was performed for 2 h to acquire long-term stability of particles. To wash Au particles, centrifugation was conducted at 10,000 rpm for 10 min, and then the supernatant containing excess TBBT, COOH-PEG-SH, and PEG-SH molecules was removed. Then, the remaining AuNP suspension was re-dispersed in water. This washing process was repeated twice for removal of unbound molecules. This colloidal solution can be stored at 4°C for more than 6 months.

In the last step, influenza A antibodies were covalently immobilized on the TBBT-labeled AuNPs. Briefly, we firstly adjusted the concentration of the aqueous solution of TBBT-labeled AuNPs so that its optical density becomes unity at 532 nm (= absorption peak wavelength). Then, 0.5 mL of the TBBT-labeled AuNPs solution and 100  $\mu$ L of an aqueous solution including 0.2 mg of EDC and 0.2 mg of NHS were mixed and kept at room temperature for 30 min to complete activation of carboxyl groups of COOH-PEG-SH molecules on AuNPs. Then, the excess amount of EDC/NHS was removed by three cycles of centrifugation (10,000 rpm, 10 min) and re-dispersion in water. In the last re-dispersion process, the particles were re-dispersed in 10 mM PBS solution (pH 7.4). Finally, 3  $\mu$ L of a 5.3 mg/mL of Influenza A antibody was added to the colloidal solution and incubated for 3 h at room temperature. The particles were washed by two cycles of centrifugation at 10,000 rpm for 10 min and re-dispersion in PBS solution. These particles are called “SERS probes”. The schematic processing of SERS probe (Ab-TBBT-PEGylated-AuNPs) synthesis was shown in Fig. 4-3.

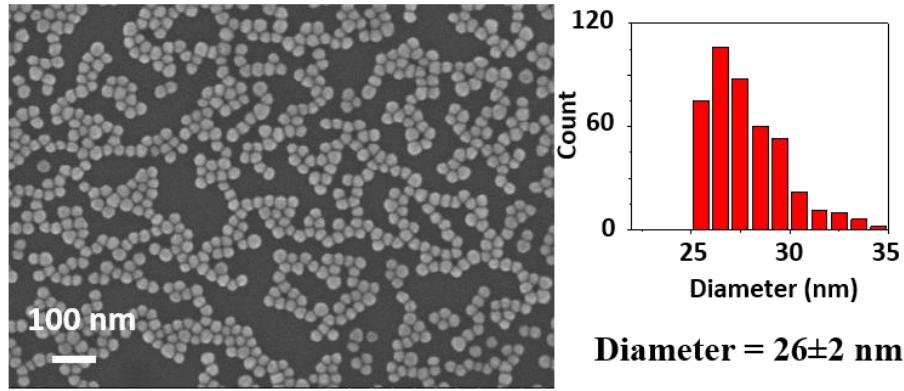


**Fig. 4-2** SEM image of 25nm-citrated AuNPs drop-casted on a Si wafer substrate. The histograms of size distribution of each particles are showed at the right hand side of SEM

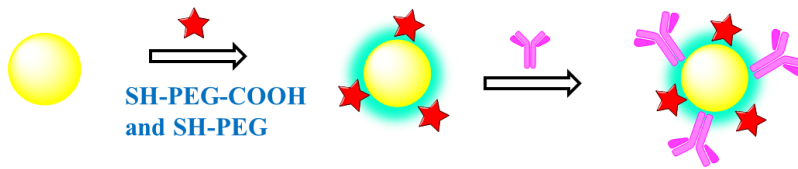


**Fig. 4-3** Schematic illustration of SERS probe synthesis (Ab-TBBT-AuNPs).

#### 4.2.2 SERS immunoassay protocol for Influenza A

The SERS immunosensor fabricated in this research is based on a direct immunoassay (Fig. 4-4). After freshly prepared hydrophilic SERS substrate was performed by immersing annealed as-prepared SERS substrate into MHDA solution, this substrate ( $10 \times 10 \text{ mm}^2$ ) was divided into quarters. A  $5 \times 5 \text{ mm}^2$  hydrophilic SERS substrate was used as the solid support for immunoassay. First, the freshly prepared hydrophilic SERS substrate was activated by successively dropping  $10 \mu\text{L}$  of a  $15 \text{ mM}$  EDC aqueous solution and  $10 \mu\text{L}$  of a  $15 \text{ mM}$  NHS solution. The mixed droplet was kept on the substrate for 30 min. Then, the substrate was washed with distilled water three times and dried by nitrogen gas. Next,  $1 \mu\text{L}$  of a recombinant nucleoprotein solution with different concentrations was directly dropped onto the SERS substrate and incubated for 30 min for immobilizing recombinant nucleoprotein. The incubation time was optimized (see Section 3.3.1). After that, the SERS substrate was washed for 5 min each in  $10 \text{ mM}$  PBS solution followed by DI water under stirring condition. Subsequently,  $5 \mu\text{L}$  of a SERS probe aqueous solution (optical density = 0.5) was dropped onto the substrate to react with the target nucleoprotein. The incubation time for

immobilizing SERS probes on recombinant nucleoproteins was 1 h, which was also optimized. Finally, the substrate was washed twice in stirred PBS solution for 5 min and then twice in stirred water for 5 min.

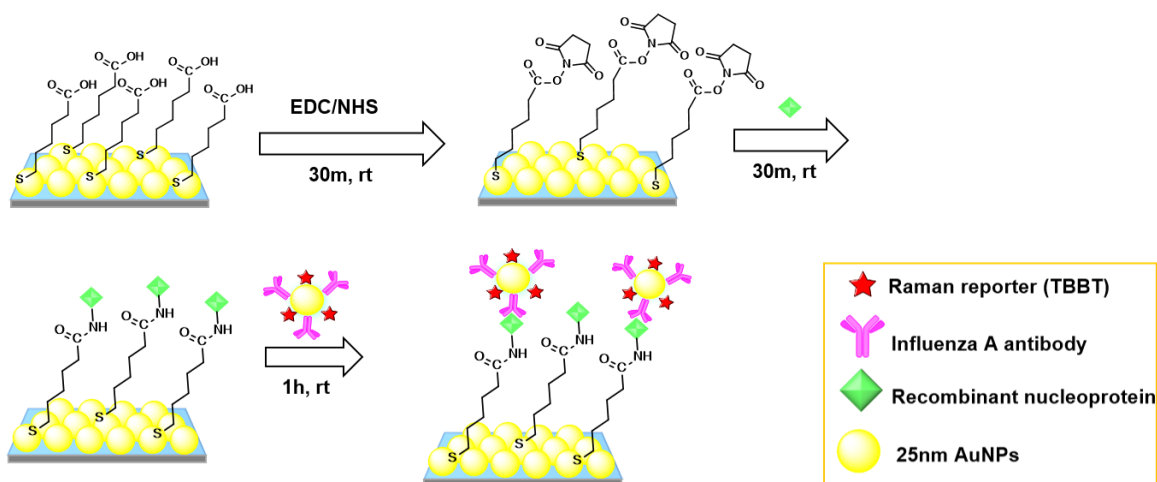


**Fig. 4-4** Schematic illustration of direct immunoassay on 2D Au@Ag NP array substrate. rt: room temperature.

## 4.3 Results and discussion

### 4.3.1 Characterization of SERS probes

As mentioned above, the SERS probes for Influenza A nucleoprotein detection were prepared in three steps; (i) synthesis of 25 nm citrate-capped AuNPs, (ii) modification of AuNPs with TBBT (Raman reporter) and PEG molecules, and (iii) immobilization of influenza A antibody. The high uniformity of citrate-capped AuNPs in shape (spherical) and in size (average diameter of  $26 \pm 2$  nm) was confirmed by SEM (Fig. 4-2). The extinction spectra of colloidal solutions of citrate-capped AuNPs, TBBT-PEGylated AuNPs, and SERS probes show a single narrow LSPR peak at around 523 nm (see Fig. 4-5). The peak position was red-shifted by a few nanometers by PEGylation, similar to the reports by X. Qian and M. Xiao groups [85,86]. This red-shift can be explained by a change in the local dielectric constant surrounding AuNPs. No spectral change of the LSPR was observed by antibody decoration on PEGylated AuNPs. The single LSPR peak with a narrow width was observed for the AuNP solutions in all three steps, indicating that the TBBT-PEGylated AuNPs and SERS probes are well dispersed and no aggregation occurs even after labeling AuNPs with TBBT.

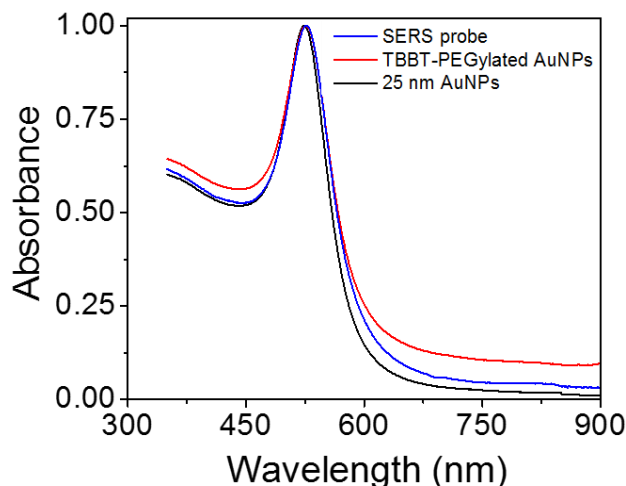


**Fig. 4-5** Extinction spectra of colloidal solutions of citrated AuNPs, PEGylated AuNPs labeled with TBBT, and SERS probes.

Figure 4-6 shows the Raman spectra of solid TBBT, TBBT-PEGylated AuNPs, and SERS probes. The characteristic Raman bands of solid TBBT were observed at 1077 and 1572  $\text{cm}^{-1}$ , which are assigned to the vibrations of  $\nu_{\text{C-S}}$  and  $\nu_{\text{CC}(\text{ring})}$ , respectively.[82,83] The corresponding bands were observed at 1065 and 1565  $\text{cm}^{-1}$  for TBBT-PEGylated AuNPs and SERS probes [87]. These vibrational frequency shifts were reported for TBBT adsorbed on AuNPs, and AgNPs, indicating chemisorptions of TBBT. The  $\delta_{\text{C-S-H}}$  band of solid TBBT at 917  $\text{cm}^{-1}$  completely disappears on the TBBT-PEGylated AuNPs and SERS probes, indicating that TBBT molecules are chemisorbed on the colloidal AuNP surface by losing two H atoms of S-H bonds. Based on TBBT molecular structure, there are two possible double-end adsorption structures; one is bidentate adsorption on a single AuNP, and the other is bridging adsorption between adjacent AuNPs, which leads to aggregation of AuNPs. After conjugation of influenza A antibody, the characteristic peaks of TBBT were still dominant; hence, both peaks at 1065 and 1565  $\text{cm}^{-1}$  can be used to detect the completion of specific antigen-antibody recognition. Since the background signal originating from the SERS substrate is more structureless around the 1565  $\text{cm}^{-1}$  band than that around the 1065  $\text{cm}^{-1}$  band, in this study the 1565  $\text{cm}^{-1}$  band was used for detection of the nucleoprotein of influenza A virus.

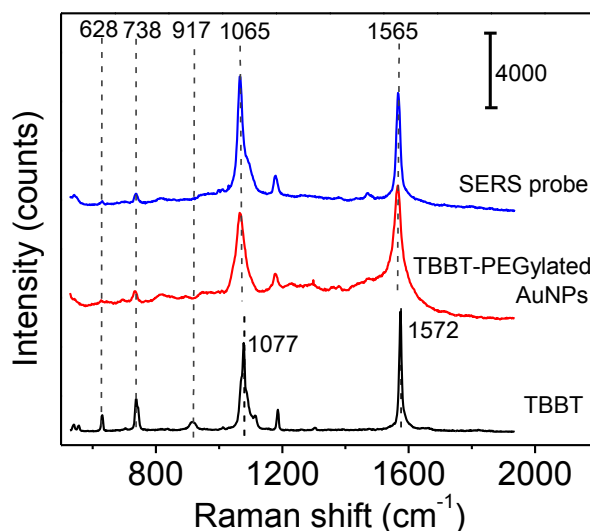


**Fig. 4-6** Raman spectra of solid TBBT, TBBT-PEGylated AuNPs, and SERS probe.

#### 4.3.2 Characterization of hydrophilic SERS substrate

Before SERS substrate fabrication, the particle size, size distribution, and morphology of Au@Ag core-shell NPs, which were the constituent NPs of the SERS-active substrates, were characterized using SEM, TEM, and EDX. The shape of Au@Ag NPs was nearly sphere as shown in Fig. 4-7(a). The size distribution ( $51 \pm 4$  nm) evaluated from 250 particles in SEM images was shown in Fig. 4-7(b). The core-shell structure of Au@Ag NPs was confirmed by EDX measurement. It was proved that Ag shell was grown uniformly on the Au core as seen in Fig. 4-7(c). The Ag shell thickness (4.5 nm) was estimated from the difference in average particle size between the Au core particles ( $42 \pm 4$  nm) and the final Au@Ag NPs ( $51 \pm 4$  nm).

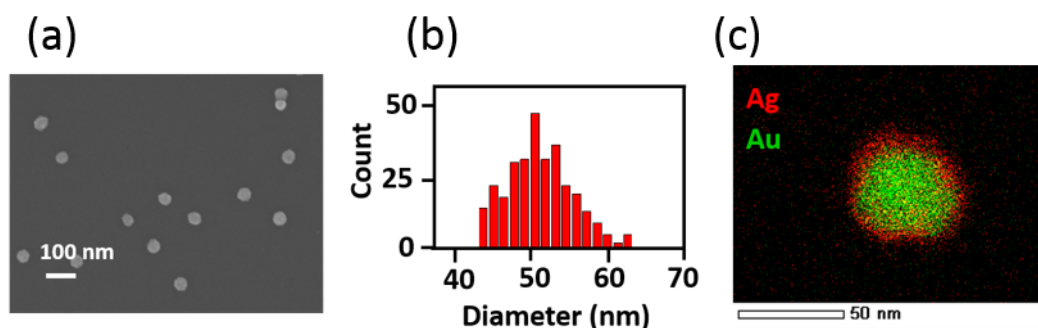


**Fig. 4-7** (a) SEM image and (b) size distribution of Au@Ag NPs used in this study. (c) EDX mapping of an Au(42 nm)@ Ag(4.5 nm) NP.

Figure 4-8(a) shows high (100k) and low (25k) magnification SEM images of a 2D array prepared by the hybrid method, indicating the high uniformity and surface coverage of the 2D array. The solid curve of Fig. 4-8(c) shows the extinction spectrum of the as-prepared 2D array. The extinction peak assigned to LSPR of the 2D array is observed around 627 nm. This result shows successful tuning of LSPR energy to the excitation (633 nm) of our Raman measurement. Hence, the highest enhancement effect is expected from the 2D array SERS substrate.

Since the constituent Au@Ag NPs of the as-prepared 2D array are stabilized with mixed alkanethiol molecules, this substrate surface is hydrophobic. As shown in the inset of Fig. 4-8(a), the contact angle of a 1  $\mu$ L water droplet was 130°, indicating a strong water-repellent characteristic. Thus, the 2D array must be hydrophilized before utilizing it as a substrate in an immunoassay using aqueous solutions. The hydrophilization was performed by annealing the hydrophobic 2D array at 90°C for 1 h and then immersing it in an ethanolic solution of MHDA at 50 °C for 12 h. Fig. 4-8(b) shows SEM images of the MHDA-functionalized 2D array and contact angle of a water droplet. The MHDA-functionalization significantly reduced the water contact angle from 130° to 35°, indicating successful hydrophilization. The arrangement of Au@Ag NPs was not influenced by MHDA-functionalization as confirmed by the SEM images. In addition, the extinction spectrum shown by the dashed curve in Fig. 4-8(c) can be used to confirm that optical property of the SERS substrate remains unchanged.

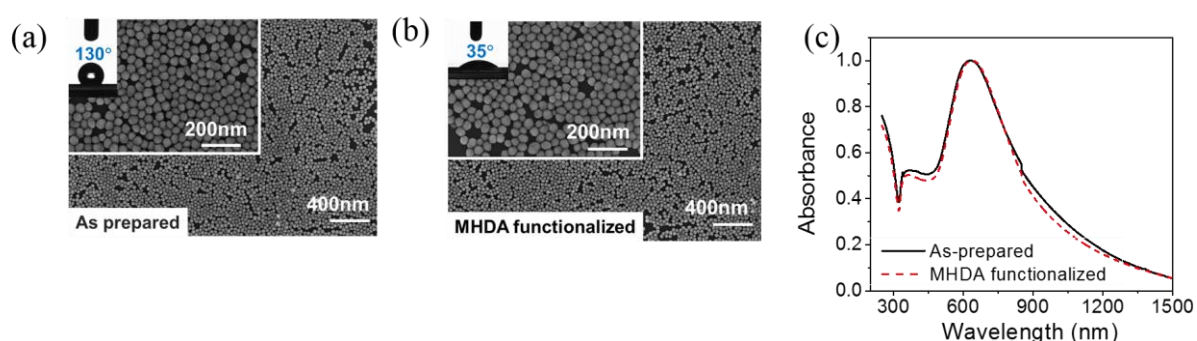


**Fig. 4-8** 25k and 100k magnification SEM images of (a) as-prepared 2D array and (b) MHDA-functionalized 2D array. The insets of (a) and (b) show the contact angle of a 1  $\mu$ L water droplet on each substrate surface. (c) Extinction spectra of as-prepared (solid curve) and MHDA-functionalized (dashed curve) 2D array.

This hydrophilization was also confirmed by attenuated total reflection Fourier transform infrared (ATR-FTIR) spectroscopy (Nicolet 4700). All reaction was confirmed by infrared (IR) absorption spectra taken at each step. Fig. 4-9(a) is the IR spectrum of the hydrophobic 2D array. Four absorption bands were clearly observed in  $\nu(\text{C-H})$  region. The absorption bands at 2847 and 2913  $\text{cm}^{-1}$  are assigned to the methylene symmetric and asymmetric C-H stretching vibrations, respectively. The 2883 and 2960  $\text{cm}^{-1}$  bands are assigned to the methyl symmetric and asymmetric C-H stretching vibrations, respectively [88]. Since the alkanethiols (dodecanethiol and octadecanethiol) have both a methyl end group and a methylene chain, the appearance of the four bands shows that the Au@Ag NPs are capped with alkanethiols. The FTIR spectrum of the annealed hydrophobic 2D array is shown in Fig. 4-9(b). The absorption intensity of the four bands was decreased by annealing, indicating that the alkanethiol capping molecules were partly desorbed from the Au@Ag NPs. After the MHDA treatment, an absorption band assigned to the carboxyl C=O stretching vibration was observed around 1710  $\text{cm}^{-1}$ , and the 2883 and 2960  $\text{cm}^{-1}$  bands assigned to the methyl C-H stretching vibrations disappeared as shown in Fig. 4-9(c). Since MHDA has a carboxyl end group but has no methyl end group, this spectral change shows that the alkanethiol capping molecules were replaced with MHDA. Since the LSPR wavelength of the resultant hydrophilic SERS substrate is matched with the Raman excitation wavelength (633 nm), this 2D array SERS substrate is suitable for an immunoassay.

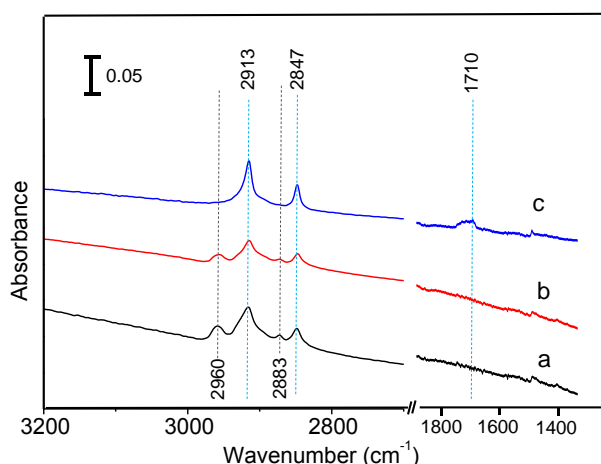


**Fig. 4-9** ATR-FTIR spectra of the 2D array of Au@Ag NPs: (a) as-prepared hydrophobic 2D array, (b) after annealing at 90°C for 1 h, and (c) after MHDA treatment.

### 4.3.3 SERS Immunoassay

#### 4.3.3.1 Optimization of immunoassay process

To maximize the performance of our immunoassay system and shorten the process time simultaneously, the incubation time for immobilizing recombinant nucleoprotein and SERS probes was optimized. To find the optimal incubation time of recombinant nucleoprotein, the whole immunoassay was performed with a different time for incubating the recombinant nucleoprotein. In this experiment, the concentration of nucleoprotein was fixed at 1.34  $\mu\text{g/mL}$ , its incubation time was varied from 15 min to 3 h, and the SERS probes were incubated for 3 h. The Raman spectra for a different incubation time of recombinant nucleoprotein are shown in Fig. 3-10(a). The intensity of the characteristic band of TBBT at  $1565\text{ cm}^{-1}$  was plotted in Fig. 4-10(b) as a function of the incubation time. The peak intensity increased with increasing incubation time and then saturated around 30 min. For incubation time of more than 2 h, the decrease of the peak intensity was observed. The reduction of peak intensity could be due to the denaturation of protein structure from the active form to an inactive form over time. Such denatured nucleoprotein lost the biological activity for binding to antibodies, leading to the lowering of the binding coefficient of nucleoprotein-antibody. From these results, the incubation time for immobilizing the recombinant nucleoproteins was determined to be 30 min.

Next, the incubation time of the SERS probes was optimized. Fig. 4-11(a) shows the Raman spectra of the immunoassay performed with a different incubation time of SERS probes, under a fixed immobilization condition of the recombinant nucleoprotein: 1.34  $\mu\text{g/mL}$  and 30 min. The characteristic peak intensity related to an incubation time of SERS probes is shown in Fig. 4-11(b). These results suggest that the incubation time of 1 h is required for sufficient nucleoprotein-antibody recognition reaction. For incubation time longer than 1 h, ~40% decrease in intensity was observed. It could be also due to the denaturation of protein structure induced by a long incubation of SERS probes. Thus, the suitable incubation time for SERS probes is 1 h.

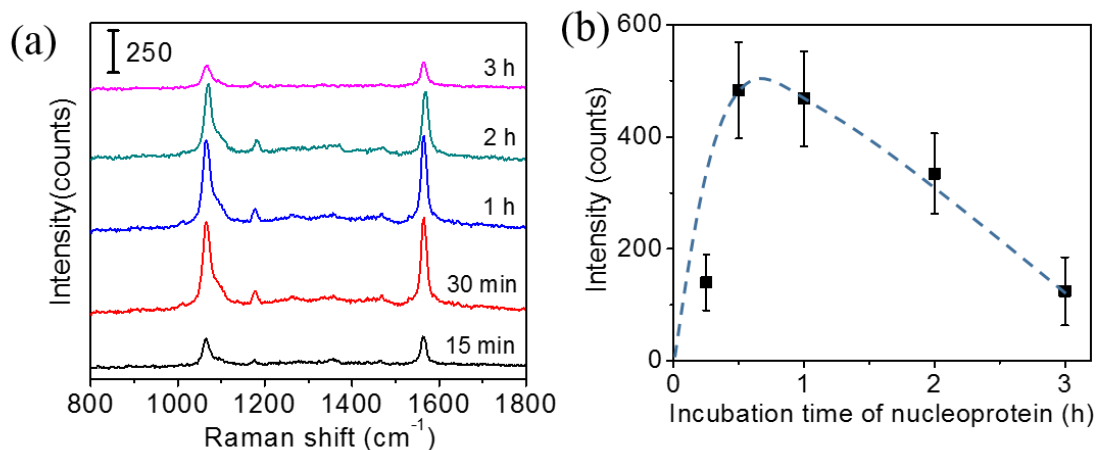


**Fig. 4-10** (a) Raman spectra when the immunoassay was performed with different incubation time of recombinant nucleoprotein, and (b) Relationship between the peak intensity of the 1565 cm<sup>-1</sup> band of TBBT and the incubation time of recombinant nucleoprotein. The dashed curve is a guide for the eye.

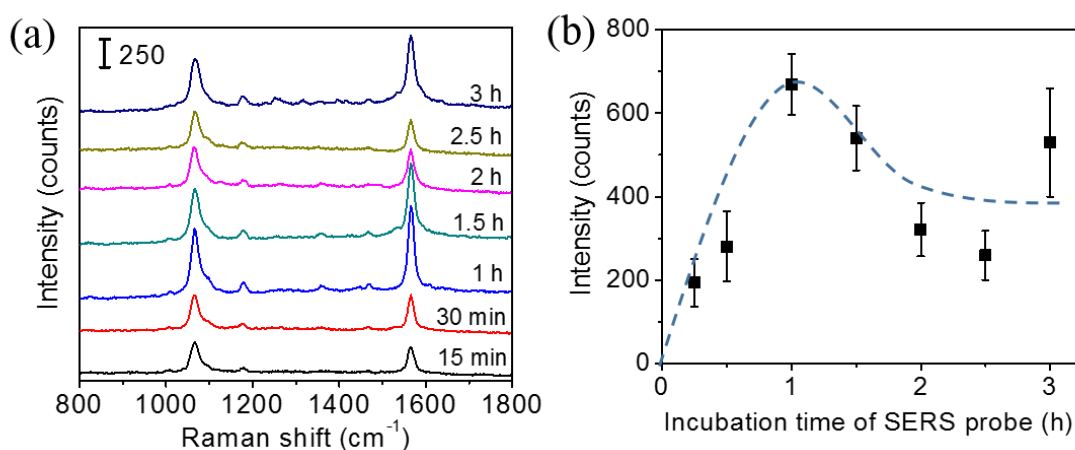


**Fig. 4-11** (a) Raman spectra of the immunoassay performed with different incubation time of SERS probes under a fixed immobilization condition of the recombinant nucleoprotein (1.34 μg/mL and 30 min), and (b) peak intensity of the 1565 cm<sup>-1</sup> band of TBBT corresponding to incubation time of SERS probes. The dashed curve is a guide for the eye.

#### 4.3.3.2 Performance of SERS immunosensing system

In order to clarify the effect of the 2D array SERS substrate towards the sensitivity improvement, a 40 nm-Au/10 nm-Cr film on a quartz substrate was used as a comparison. This film was prepared by depositing Cr

and Au sequentially on the quartz substrate by thermal evaporation in a vacuum ( $<10^{-4}$  Pa). The Au film surface was hydrophilized by immersion in an ethanolic solution of MHDA for 12 h at 50 °C, and then activated by EDC/NHS in the same manner as the SERS substrate. For sensitivity study, the recombinant nucleoprotein solutions with different concentrations were prepared via serial dilution of a 134  $\mu\text{g/mL}$  stock solution of recombinant nucleoprotein to final concentrations of 134, 67, 13.4, 6.7, 1.34, 0.67, 0.134, 0.067, 0.0134, and 0.0067  $\mu\text{g/mL}$ , and the whole immunoassay was conducted.

Fig. 4-12(a) shows the Raman spectra of the immunoassay conducted on the SERS substrates. For the control, PBS solution without recombinant nucleoprotein was dropped onto the substrates. The result demonstrated that several Raman bands were observed for the control sample on a SERS substrate in the range of 600 to 1600  $\text{cm}^{-1}$ , which can be tentatively assigned to the vibrational modes of MPTMS and activated MHDA. The assignment was presented in Table 4-1. These bands are found to be well separated from the characteristic Raman bands of TBBT at 1565  $\text{cm}^{-1}$ . As expected, the 1565  $\text{cm}^{-1}$  band was negligibly weak for the control samples, and its intensities increased with increasing concentration of recombinant nucleoprotein.

Fig. 4-12(b) show the sensitivity curves of the immunoassay conducted on the SERS substrate and the Au film substrate in the entire measurement range. The sensitivity curves were obtained by plotting the intensity of the 1565  $\text{cm}^{-1}$  band as a function of the concentration of recombinant nucleoprotein. The stronger Raman signal was observed for the SERS substrate than that of the Au film substrate with the same concentration of the target. Both sensitivity curves show a similar pattern of dependence; i.e. initially the Raman intensity increases almost linearly with increasing concentration of recombinant nucleoprotein, and then the increasing rate gradually decreases. The linear relation was observed in the concentration range of 0.0067 to 0.134  $\mu\text{g/mL}$  for both substrates.

The linear sensitivity curves are shown in Fig. 4-12(c). Comparing the slopes, we found that the sensitivity of immunoassay improved about 4 times by using the 2D Au@Ag NP array substrate, instead of the flat Au film substrate. The limit of detection (LOD) of the immunoassay was estimated using the linear sensitivity curves. The definition of LOD used in this study is described in experimental section. The LOD of the immunoassay using the SERS substrate was 8  $\text{ng/mL}$  (0.14 nM), while that using the Au film substrate was 59  $\text{ng/mL}$  (1.05 nM). Since the increase of the surface area of the 2D-NP array against the flat surface is

at the outside twice, the improvement in the sensitivity and detection limit can be mainly attributed to plasmon coupling between the SERS probe and the SERS substrate. Finally, comparison of the LOD with those of other techniques previously reported for detecting the same analyte. The LOD of our SERS immunoassay system (8 ng/mL) is much lower than those of fluorescence-based LFIA (250 ng/mL), [89] an immune-interferometric sensor (1 $\mu$ g/mL), [90] and comparable to that of the electrochemical immunoassay (e-ELISA) (10 ng/mL). [91]

**Table 4-1** Possible peak assignment of the Raman spectrum of the EDC/NHS-activation 2D array.

Observed peak (cm <sup>-1</sup> )	Possible assignment
679	v(Si-C) [92]
702 sh	v(S-C) <sub>T</sub> [92,93]
750	CH <sub>2</sub> rock [93,94]
837	CH wagging [95]
850	CH <sub>2</sub> rock [94]
952	v(Si-OH) [92]
1002	v(C-C) <sub>T</sub> [92,94]
1036	CH <sub>2</sub> rock [92,94]
1104	v(Si-O-Si) [92] or v(C-C) <sub>T</sub> [93]
1138	CH <sub>2</sub> twist [92] or v(C-C) <sub>T</sub> [93]
1156	C-O stretch [95]
1195	CH <sub>2</sub> twist [92,94]
1217	CH <sub>2</sub> twist [92] or wagging [94]
1272	CH <sub>2</sub> twist [92] or wagging [94]
1303	CH <sub>2</sub> twist [92,94]
1338	CH <sub>2</sub> twist [92] or wagging [94]
1455	CH <sub>2</sub> bending [94-96]

sh: shoulder, v: stretching, T: trans.

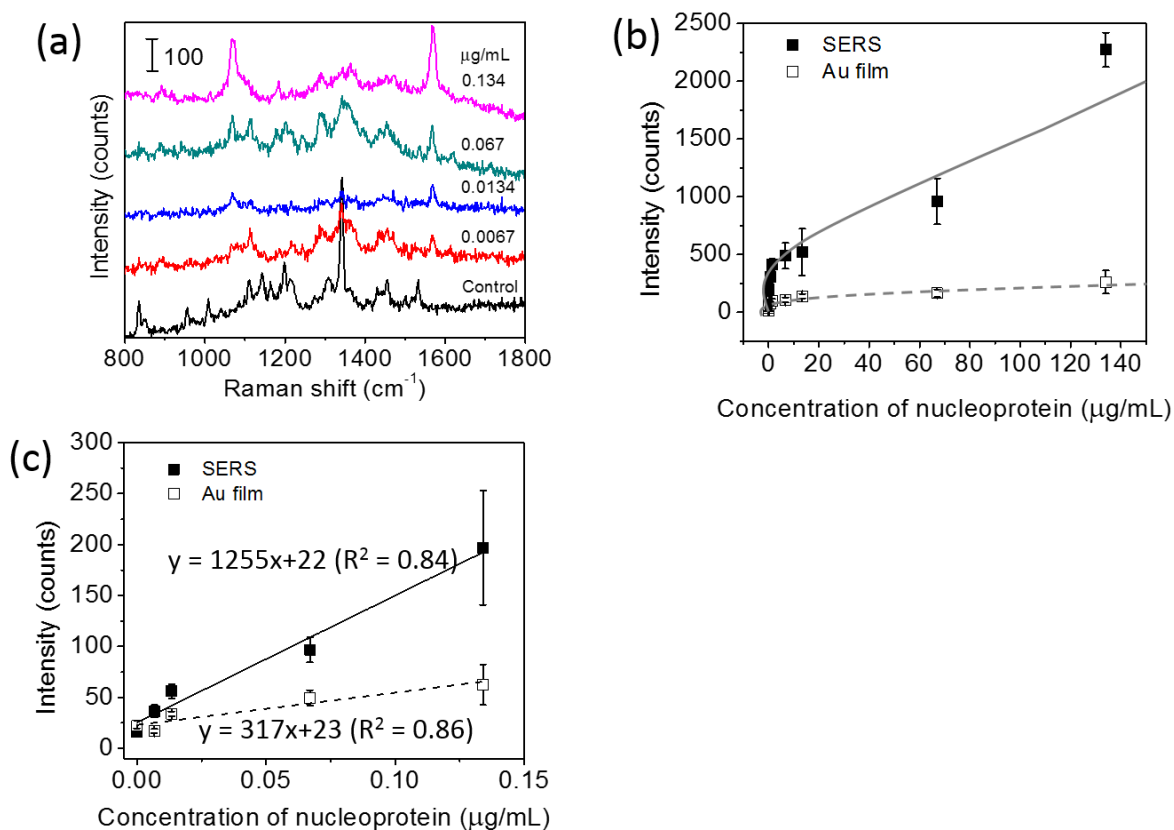


**Fig. 4-12** (a) Raman spectra of the immunoassay performed on the SERS substrates. The concentration of nucleoprotein was: 0 (control), 0.0067, 0.0134, 0.067, and 0.134 µg/mL from the bottom to the top. (b) Sensitivity curves of the immunoassay performed on the SERS and Au substrates over the entire measurement range from 0.0067 to 134 µg/mL of nucleoprotein concentration. These sensitivity curves were obtained from the peak intensity of the 1565 cm<sup>-1</sup> band. The solid and dashed curves are guides for the eye. (c) Sensitivity curves in the linear region. The solid and dashed straight lines are obtained by the method of least squares. The solid and open symbols in (b,c) shows the data points for the immunoassay performed on the SERS and Au substrates, respectively.

#### 4.3.3.3 Selectivity

To examine the selectivity of our immunoassay system, a variety of proteins; recombinant nucleoprotein, avidin, bovine serum albumin (BSA), lysozyme, tryptone, and ampicillin, were immobilized on the SERS substrates at the same concentration (13.4 µg/mL). The Raman signal intensity observed after incubating SERS probes are summarized in Fig. 4-13. The intense characteristic peak of TBBT at 1565 cm<sup>-1</sup> was observed only

for recombinant nucleoprotein. The signal intensity for the others protein is comparable to that of the negative control sample (PBS solution without nucleoprotein). This result clearly shows that our SERS immunoassay has high selectivity against recombinant nucleoprotein.

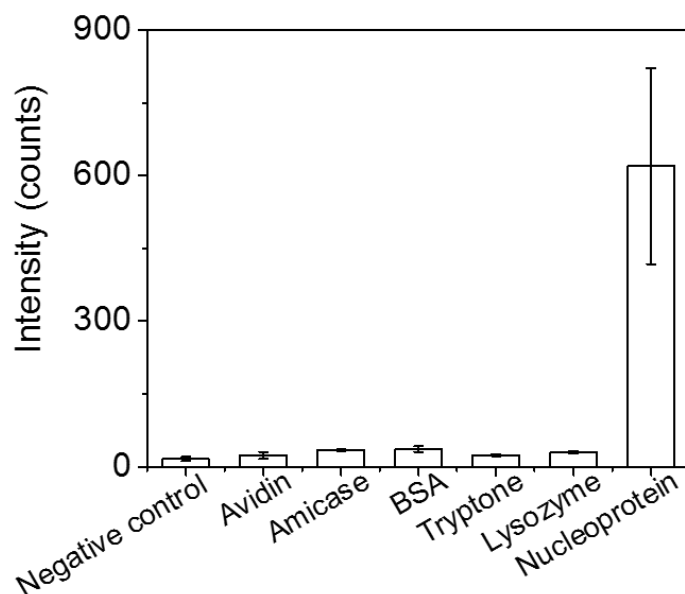


**Fig. 4-13** Selectivity of SERS immunoassay. The concentration of all proteins were fixed at 13.4 $\mu$ g/mL. The peak intensity of the 1565  $\text{cm}^{-1}$  band was plotted.

#### 4.3.3.4 Reproducibility

Reproducibility of our SERS immunoassay was examined by performing the immunoassay using ten different SERS substrates. In this measurement, the concentration of recombinant nucleoprotein was fixed at 1.34  $\mu$ g/mL. Ten repetitive measurements were performed at different positions for each sample. The relative standard deviation (RSD) of the peak intensity of the 1565  $\text{cm}^{-1}$  band within the sample was less than 5 %. The sample-to-sample variation of detected Raman intensity was shown in Fig. 4-14. The variation of the average intensity was calculated to be 4.6 % RSD, which were considered acceptable values (<30%RSD) [75]. The small sample-to-sample variation was attributed to the high uniformity and high reproducibility of surface coverage of 2D array. From the results, we can confirm that our SERS immunoassay possesses high reproducibility.

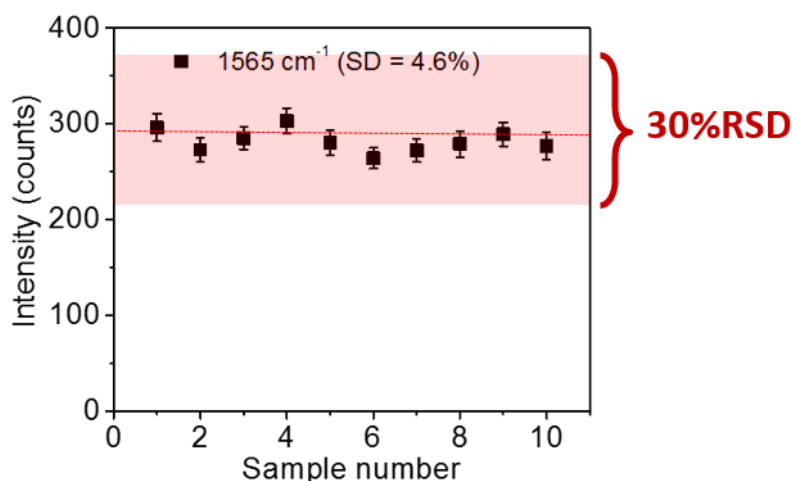


**Fig. 4-14** Reproducibility of SERS immunoassay (peak intensity of the 1565  $\text{cm}^{-1}$  band). The concentration of recombinant nucleoprotein was fixed at 1.34  $\mu\text{g/mL}$ .

#### 4.3.3.5 Analysis of the nucleoprotein in infected allantoic fluid

To demonstrate the applicability of our SERS immunoassay system for complex biological samples detection, a stock solution of Pandemic 2009 influenza A H1N1 virus-infected allantoic fluid containing  $5.6 \times 10^3$   $\text{TCID}_{50}/\text{mL}$  (50% tissue culture infectious dose) was used. The infected allantoic fluid solutions with different concentrations were prepared by serial dilution of the stock solution with extraction buffer solution. 1  $\mu\text{L}$  of diluted allantoic fluid was dropped directly on the SERS substrate and incubated at  $4^\circ\text{C}$  for 30 min,[89] and then the substrate was rinsed with PBS solution and distilled water. Before Raman measurement, a SERS probe solution was dropped on the substrate and incubated for 1h, and subsequently, the substrate was rinsed with distilled water. Fig. 4-15(a) and 4-15(b) show the Raman spectra and the sensitivity curve, respectively, of our immunoassay system with respect to the infected allantoic fluid. Initially, the intensities of the characteristic Raman peaks of TBBT are increased with increasing concentration of the allantoic fluid, and then the increasing rate gradually decreases. The linear relation was observed in the range of 5 to 56  $\text{TCID}_{50}/\text{mL}$  for a characteristic peak at  $1565 \text{ cm}^{-1}$  with a correlation coefficient ( $R^2$ ) of 0.96. The detection limit was estimated to be 6  $\text{TCID}_{50}/\text{mL}$ . This result indicates that this SERS immunoassay has a great performance to detect nucleoprotein from an allantoic fluid containing various kinds of interference matrix. This highly sensitive detection of influenza A nucleoprotein in a complex matrix is strongly attributed to the

high sensitivity and selectivity of our SERS immunoassay system. The performance of other representative techniques for detecting infected allantoic fluid of Influenza A is summarized in Table 4-2. The LOD of our SERS immunoassay system (6 TCID<sub>50</sub>/mL) is lower than those of the previously reported techniques: Fluorescence based-Lateral flow immunoassay (11 TCID<sub>50</sub>/mL),[89] Colorimetric based Lateral flow immunoassay (47 TCID<sub>50</sub>/mL for Influenza A nucleoprotein, [97] and  $5 \times 10^2$  TCID<sub>50</sub>/mL for Influenza A virus).[98]

**Table 4-2** Summary of LOD of representative sensors for detecting infected allantoic fluid.

<b>Probe</b>	<b>Biomarker</b>	<b>Type of assay</b>	<b>Detection method</b>	<b>Linear range</b>	<b>LOD</b>	<b>ref</b>
<b>Cy5- doped SiO<sub>2</sub>NPs</b>	infected allantoic fluid	sandwich	Fluorescence based-ELISA	50-1000 TCID <sub>50</sub> /mL	11 TCID <sub>50</sub> /mL	[89]
<b>Dual mAb-immunogold</b>	infected allantoic fluid	sandwich	Color based Lateral flow immunoassay	NA	47 TCID <sub>50</sub> /mL	[97]
<b>mAb-immunogold</b>	infected allantoic fluid	sandwich	Absorbance-based LFIA biosensor	NA	$5 \times 10^2$ TCID <sub>50</sub> /mL	[98]
<b>PEGylated, TBBT-labeled immunogold</b>	infected allantoic fluid	direct	SERS-based biosensor	5-56 TCID <sub>50</sub> /mL	6 TCID <sub>50</sub> /mL	This work

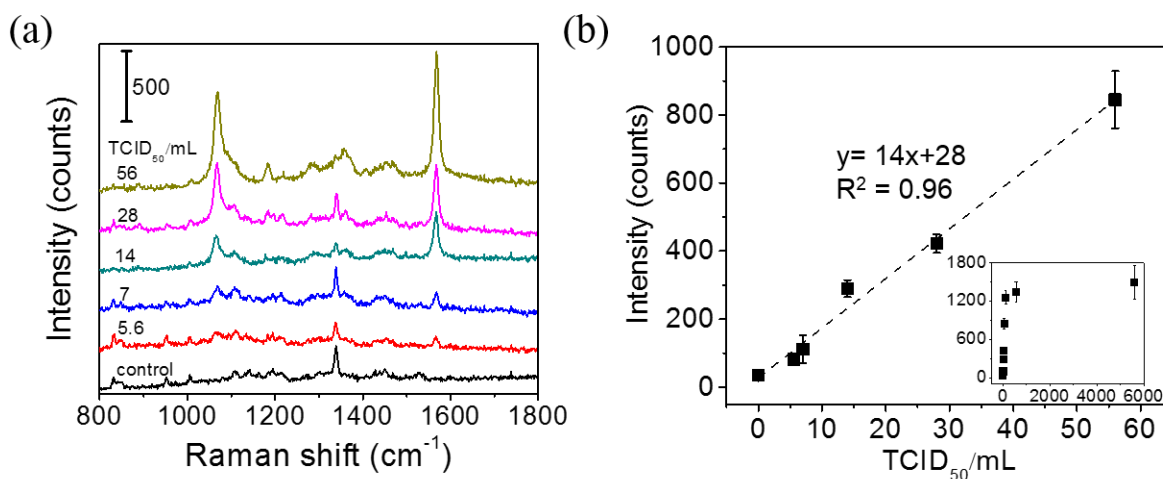


**Fig. 4-15** (a) Raman spectra of the immunoassay for infected allantoic fluid, whose concentration was varied from 0 (control) to 56 TCID<sub>50</sub>/mL. (b) Sensitivity curve of the SERS immunoassay for influenza A infected allantoic fluid. This sensitivity curve was obtained by plotting the peak intensity of the 1565 cm<sup>-1</sup> band. The data points over the entire measurement range are shown in the inset. The dashed straight line was obtained by the method of least squares.

#### 4.4 Conclusion

A SERS immunoassay with high sensitivity and selectivity for Influenza A was demonstrated utilizing both PEGylated TBBT-labeled AuNPs covered with influenza A antibody as the SERS probes and hydrophilic Au@Ag 2D array as the SERS substrates. The antibody-antigen recognition was detected by observing characteristic Raman signal of TBBT (Raman reporter). Immunoassay taken place on SERS substrates has about 4 times higher sensitivity than immunoassay on Au film substrates because the Raman signal from the SERS probes is amplified by the electromagnetic field enhancement effect of the SERS substrate. This immunoassay shows the good performance to detect the target nucleoprotein in a complex biological matrix that contains various kinds of interferences with the detection limit of 6 TCID<sub>50</sub>/mL. These results indicate that using a well-tuned Au@Ag 2D array as a SERS substrate is an effective way for improving the sensitivity of SERS-based biosensors.

## CHAPTER V

### INVESTIGATION OF THE FACTORS DETERMINING SENSITIVITY OF SERS IMMUNOASSAY: SERS PROBE SIZE AND SEPARATION DISTANCE BETWEEN SERS PROBE AND SUBSTRATE

The sensitivity of the sensor relies on the amplification of the signal from SERS probe after antigen-antibody recognition, which depends on the localized surface plasmon resonance (LSPR) of AuNPs of SERS probe and the strength of electromagnetic field enhancement between probe and substrate. The LSPR of AuNPs depends on their size, shape, and material [99-101]. Compared with other parameters, optimizing the AuNPs size of probes is a simple and effective ways to improve the detection sensitivity. Moreover, the sensitivity of immunoassay influences by the plasmon coupling between the SERS probe and SERS-active substrate, whose strength becomes strong as the separation distance between the SERS probe and substrate decreases. In sandwich SERS immunoassay, the capture antibody-antigen-detection antibody acts as the separation barrier between the SERS probe and substrate. In addition to the size of the antigen/antibody, the size of MNP of the SERS probe also influences the plasmon coupling between the SERS probe and SERS-active substrate, because the strong electromagnetic field associated with the LSPR of MNPs decays with a length scale of the size of MNP [102,81]. This means that the larger MNP allows larger separation distance between the SERS probe and SERS-active substrate. Therefore, from the viewpoint of the plasmon coupling, the optimization of the MNP size, and the size of antigen/antibody used in the immunoassay are important for realizing the high sensitive SERS-based immunoassay.

In this chapter, the influence of the SERS probe size and the length of the antibody-antigen-antibody complex on the sensitivity of sandwich-type SERS-based immunosensors was investigated, in which hydrophilic 2D arrays of Au (42 nm-core)@Ag (5 nm-shell) NPs were used as the SERS-active substrates. The SERS probes are AuNPs functionalized sequentially with 4-mercaptobenzoic acid (MBA), heterobifunctional polyethylene glycol (HS-PEG-COOH), and the antibody specific to a target antigen. MBA was selected as the Raman reporter molecule because it shows strong Raman bands at 1089 and 1587  $\text{cm}^{-1}$  and has a carboxyl group to immobilize an antibody. First, to find the optimal SERS probe size, sandwich

immunoassay for Human-IgG was performed using SERS probes of different Au-core sizes from 26 to 110 nm. The highest SERS intensity (sensitivity) was observed at an Au-core size of 53 nm. Next, to examine the influence of the size of the immunocomplexes (capture antibody-antigen-detection antibody) on the sensitivity, the sandwich immunoassay for Human-IgG and prostate-specific antigen (PSA) was performed using SERS probes whose Au core size is 53 nm. Human-IgG and PSA were selected as representative large (36 nm) and small (28 nm) immunocomplexes, respectively. The sensitivity enhancement achieved by using the SERS-active substrate instead of a flat Au substrate was evaluated for both immunoassays for Human-IgG and PSA. By comparing the sensitivity enhancement factors, we found that the sensitivity of the sandwich-type SERS immunoassay increases by a factor of 3 as the size of the immunocomplexes decreases from 36 nm to 28 nm. This result suggests that the sensitivity of SERS-based immunoassay performed on SERS-active substrates can be improved by adopting a smaller antibody or antibody-fragment for a given target antigen. Our SERS-based immunoassay system showed a low detection limit of 0.3 pg/mL for free PSA and 0.05 pg/mL for Human-IgG.

This chapter is organized into four sections. Firstly, the information of the two biological systems with different antigen sizes: immunoglobulin G (IgG) and prostate-specific antigen (PSA) are explained. Then, SERS probe synthesis and immunoassay protocols for H-IgG and PSA are described. The SERS probe characterization, the influence of the SERS probe size on the sensitivity of immunoassay, and the influence of the size of antigen/antibody complexes on the sensitivity of immunoassay are presented. Finally, the conclusion of this topic was reported.

## **5.1 Biological systems in this study**

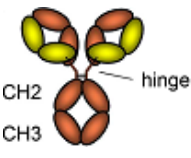
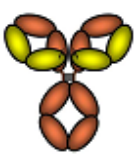
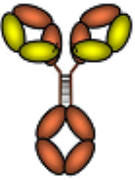
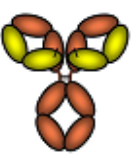
In this study, the two biological systems were selected in the SERS immunoassay as representative models of large and small antigen sizes: Immunoglobulin G (IgG) and prostate specific antigen (PSA).

### **5.1.1 Immunoglobulin G (IgG)**

IgG is the antibody produced by the immune system to fight with bacteria, viruses, and toxins. Immunoglobulin G (IgG) is the major class of the five classes of Ig in human beings: IgG, IgM, IgA, IgE, and IgD [103]. IgG

molecules are able to react with Fc $\gamma$  receptors located on the surface of macrophage and natural killer cells. IgG is produced in a delayed response after infected by pathogens or allergens and can be circulated in the body for a long time. The long half-life of IgG in serum is useful for passive immunization by transfer of this antibody. The detection of IgG is performed to indicate a prior infection or vaccination. IgG can be divided into four subclasses: IgG1, IgG2, IgG3, and IgG4. Each IgG subclass has different structures and responds to different target antigens. The structures and properties of each IgG subclass are presented in table 5-1.

**Table 5-1** Structures and properties of IgG subclasses [103].

Properties	IgG1	IgG2	IgG3	IgG4
<b>General</b>				
Structure				
Molecular mass (kDa)	146	146	170	146
Amino acid in hinge area	15	12	62	12
Inter-heavy chain disulfide bonds	2	4	11	2
Mean adult serum level (g/l)	6.98	3.8	0.51	0.56
Relative abundance (%)	60	32	4	4
Half-life (days)	21	21	7-21	21
<b>Antibody response to:</b>				
Protein	++	+/-	++	++
Polysaccharides	+	+++	+/-	+/-
Allergens	+	(-)	(-)	++

### 5.1.2 Prostate-specific antigen (PSA)

Prostate-specific antigen (PSA) is a cancer biomarker for prostate cancer, which is produced by the prostate gland and circulate in the bloodstream. Two forms of PSA proteins exist in the blood and seminal fluid: bound and free PSA. The level of total PSA can be used for prostate cancer indication. The small amount of PSA in

serum is found in healthy men, but it is elevated in the men who may have a risk of prostate cancer. The value of PSA level is shown as follows; normal PSA = 0-4 ng/mL, slightly elevated PSA = 4-10 ng/mL, moderately elevated PSA = 10-20 ng/mL, highly elevated PSA = 20+ ng/mL. However, the elevated PSA level will also cause by uncontrollable factors, e.g. age, family history, and race, which is called noncancerous prostate enlargement. There are two ways to forecast the state of cancer; (i) the detection of free PSA, and (ii) evaluation of ratio between free PSA and total PSA. For first evaluation, the reduction of PSA level has been focused. It results from the PSA that releases from the cancerous cell is bound PSA, not free PSA. Therefore, the free PSA level from patients is low by comparing with those from normal men. In the case of another PSA evaluation, the ratio of free PSA: total PSA is an additional test for PSA diagnosis. The ratios between free/total PSA are different in men with a different state of cancer. The lower ratio of free/total PSA is found from patients. Whereas, higher free/total PSA is detected from normal men. Regarding the clinical report, the decrease of PSA level showed the high risk for prostate cancer. Therefore, to improve the detection limit to detect trace amount of PSA (cancer biomarker) is the big challenge for monitoring and observing the patient's condition. The detection result is very important for cancer screening and implements medicine treatment.

## **5.2 Experimental**

### **5.2.1 SERS probe synthesis**

SERS probes of different sizes were prepared in the following three steps: (i) synthesis of citrate-capped AuNPs of different sizes, (ii) labeling and stabilizing the AuNPs with MBA and PEG molecules, respectively, and (iii) antibody immobilization. The details of the citrate-capped AuNP synthesis are already described in the previous section. After the concentration of the obtained aqueous solution of citrate-capped AuNPs was adjusted so that the optical density became unity (optical path length = 10 mm) at the peak wavelength of LSPR, the AuNPs were labeled with MBA by adding a 1mM solution of MBA in ethanol to the stirred solution of citrate-capped AuNPs (1 mL). The stirring was continued for 3 h at RT. The amount of MBA solution used in this treatment was varied depending on the size of AuNPs (See Table 5-2). Then, to stabilize the particles, 100  $\mu$ L of a 1 mM aqueous solution of SH-PEG-COOH was added to the stirred colloidal solution, and the stirring was continued for 1 h at RT. The excess amount of MBA and SH-PEG-COOH were removed by two

cycles of centrifugation and re-dispersion in DI water. The rotation speed of centrifugation was varied depending on the size of AuNPs (see Table 5-2). After this washing treatment, the optical density of the colloidal solution of PEGylated MBA-labeled AuNPs was brought back to unity by adding a proper amount of DI water.

Finally, antibody immobilization was performed as follows. Since MBA and SH-PEG-COOH bind to the AuNP surface by forming Au-S bonds, the carboxyl groups are exposed outward. The solvent of 1 mL of the aqueous solution of PEGylated MBA-labelled AuNPs was exchanged with the same volume of PBS solution. The carboxyl groups of MBA and SH-PEG-COOH binding to AuNPs were activated by adding a mixture of 100  $\mu$ L of 15 mM EDC in PBS solution and 100  $\mu$ L of 15 mM NHS in PBS solution to the colloidal solution and stirring the mixture for 30 min. After the excess amount of EDC and NHS were removed by three cycles of centrifugation and re-dispersion in PBS solution, antibodies were immobilized on the PEGylated MBA-labeled AuNPs by adding an antibody solution (10  $\mu$ L of a 1 mg/mL solution of anti H-IgG or 10  $\mu$ L of a 1  $\mu$ g/mL solution of PSA monoclonal detection antibody in PBS solution) to 1 mL of the colloidal solution. This solution was kept at 4 °C overnight to complete the immobilization. The unreacted antibodies were removed by two cycles of centrifugation and re-dispersion in PBS solution, and then the remained colloidal solution was re-dispersed in 1% (w/v) BSA in PBS solution for blocking the nonspecific binding site. The unreacted BSA was removed by two cycles of centrifugation and re-dispersion in PBS solution. In the last re-dispersion process, the concentrated suspension was re-suspended in PBS solution so that the final volume became 1 mL. This suspension was stored at 4°C until use. The particles were dispersed by sonication before use. Hereafter, the PEGylated MBA-labeled immunogold is referred to as SERS probe, and for simplicity the size of SERS probe is specified by the Au core diameter.

**Table 5-2** Amount of 1 mM ethanolic solution of MBA used for labeling AuNPs of different sizes and centrifuge rotor speed for AuNPs of different sizes.

Diameter of AuNPs (nm)	Amount of MBA solution ( $\mu$ L)	Centrifuge rotor speed (rpm)
26	300	10,000
31	300	10,000
42	300	8,000
53	200	7,000
77	300	5,000
110	400	5,000

### 5.2.2 Sandwich immunoassay protocol

The sandwich immunoassays for H-IgG and PSA were performed on the SERS substrates (2D arrays of Au (42 nm-core)@Ag (5 nm-shell) NPs) and Au evaporated film substrates (reference substrates). The preparation process of both substrates was already mentioned in the previous chapter. [104] In the last preparation step, these substrates were hydrophilized by surface modification with MHDA. Just before immunoassay, these substrates were immersed in a mixed aqueous solution of EDC and NHS (15 mM each) for 1 h in a dark chamber in order to activate the carboxyl group of MHDA. The unreacted reagents were removed by rinsing with PBS solution 3 times.

In the immunoassay for H-IgG, 10  $\mu$ L of a PBS solution containing anti H-IgG at a concentration of 1 mg/mL was dropped onto the substrates ( $5 \times 5$  mm<sup>2</sup>) and incubated overnight in a moist chamber at 4°C for immobilizing the capture-antibody. To remove the unreacted antibodies, the substrates were washed with a PBS solution containing the detergent Tween 20 at a concentration of 0.05% (TPBS) and then rinsed with PBS solution. The non-specific binding sites were blocked with BSA, which was conducted by immersing the substrates in a PBS solution with 0.05% (w/v) BSA for 30 min. The free BSAs were removed by sequential rinsing with TPBS and PBS solution. The immunosubstrates were stored in a PBS solution at 4°C until use. Then, the antigen immobilization was performed by dropping 10  $\mu$ L of a PBS solution containing H-IgG antigen onto the immunosubstrates and keeping them in a moist chamber at 4°C for 20 min. The unbound antigen was removed by sequential rinsing with TPBS and PBS solution. Next, 10  $\mu$ L of an aqueous solution of the SERS probes was pipetted onto the immunosubstrates, and the solution was kept on the substrates for

10 min to complete the antigen-antibody binding. To remove unreacted SERS probes, the substrates were rinsed sequentially with TPBS, PBS solution, and DI water and dried under N<sub>2</sub> gas flow. Finally, the Raman spectra of the substrates were measured.

The protocol of immunoassay for PSA was the same as that for H-IgG, except for the following conditions; the concentration of the PSA capture-antibody in PBS solution was 1 µg/mL, and the capture-antibody was incubated at room temperature (RT) for 6 h; the incubation for immobilizing the PSA antigen was performed at RT for 3 h; and the SERS probe immobilization was carried out at RT for 3 h. The protocols of the sandwich SERS immunoassays for H-IgG and PSA are illustrated in Fig. 5-1. The immunoassay conditions for the two systems were determined based on those reported in literatures [105-107].

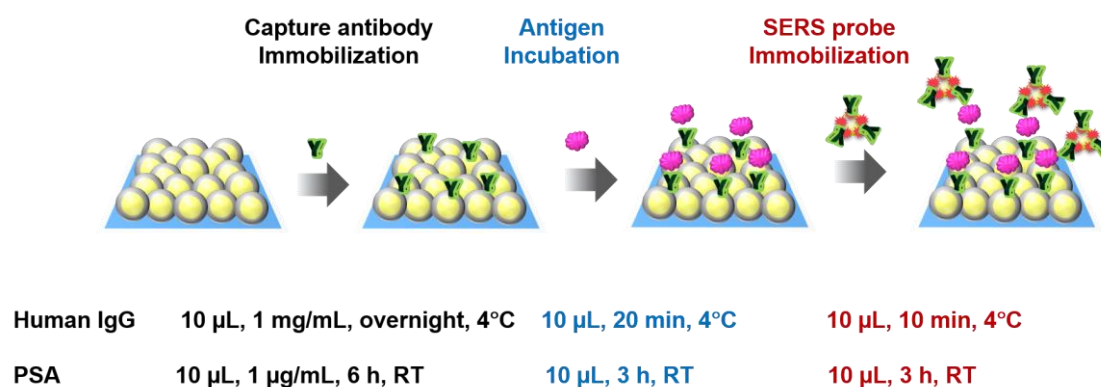


**Fig. 5-1** Schematic illustration of sandwich immunoassays for Human IgG and PSA.

## 5.3 Results and discussion

### 5.3.1 Characterization of SERS probe

First, we examined the size distribution and shape uniformity of the Au core particles. The SEM images of citrate-capped AuNPs of different sizes are shown in Fig. 5-2(a), indicating that the shape is nearly sphere for all the sizes. The size distribution (average ± standard deviation) evaluated from one hundred particles in the SEM images taken with a magnification of 100k was: 26 ± 2 nm, 31 ± 2 nm, 42 ± 4 nm, 53 ± 5 nm, 77 ± 8 nm, and 110 ± 8 nm. The relative standard deviation was approximately less than 10 % for all the sizes. The uniformity of AuNPs is crucial for examining the probe size dependence of the sensitivity of immunoassay. Figure 5-2(b) shows the extinction spectra of the PBS solutions of SERS probes of different sizes. The

maximum of the extinction band assigned to the LSPR was located at 529, 534, 543, 553, 575, and 607 nm for the 26, 31, 42, 53, 77 nm and 110 nm-SERS probes, respectively, and the bandwidth increased with increasing particle size. Similar spectral change of the LSPR band with increasing particle size was commonly observed for aqueous colloidal solutions of AuNPs [108-110]. The spectral change is attributed to the electromagnetic retardation effects in larger particles, which increases the contribution of higher-order plasmon modes to the extinction spectra for larger particles [111]. The LSPR of the SERS probes was slightly red-shifted (2-3 nm) compared to that of the citrate-capped AuNPs of the same size, which was induced by capping AuNPs with MBA, PEG, and antibody (data not shown).

Figure 5-2(c) shows the Raman spectrum of the 53 nm-SERS probes drop-casted on a Si substrate, together with that of solid MBA. The very strong Raman bands assigned to the  $\nu_{12}$  and  $\nu_{8a}$  aromatic ring vibrations [112,113] were observed at 1089 and 1587  $\text{cm}^{-1}$  for the SERS probes. These peak positions were slightly lower than those of solid MBA (1112 and 1607  $\text{cm}^{-1}$ , respectively). From these peak shifts, we confirmed that MBA was chemisorbed on AuNPs [112]. In this study, the 1587  $\text{cm}^{-1}$  band was used for detection of target analytes, because the 1587  $\text{cm}^{-1}$  band was well-separated from the Raman signal arising from the SERS substrates (2D-arrays of Au@Ag NPs) typically displayed at 1003, 1035, 1110, 1143, 1180, 1340, 1454, and 1530  $\text{cm}^{-1}$ .

The successful immobilization of antibody on the PEGylated MBA-labeled AuNPs was confirmed by measuring the FTIR spectra in an ATR geometry. Figure 5-2(d) shows the IR spectra of the PEGylated MBA-labeled AuNPs and SERS probes drop-casted on Si substrates. In the spectrum of PEGylated MBA-labeled AuNPs, the IR bands assigned to the C=O stretching of COOH group and the C-S vibration [114] were observed at 1691 and 1111  $\text{cm}^{-1}$ , respectively. The observation of these bands indicates the existence of MBA and/or SH-PEG-COOH molecules chemisorbed on AuNPs. After antibody immobilization, the 1691  $\text{cm}^{-1}$  band disappeared and the bands assigned to the C=O of the amide bond and the N-H stretching of antibody [115] appeared at 1656 and 3243  $\text{cm}^{-1}$ , respectively. From these spectral changes, the antibody was confirmed to be immobilized on the SERS probes via the amide linkage.

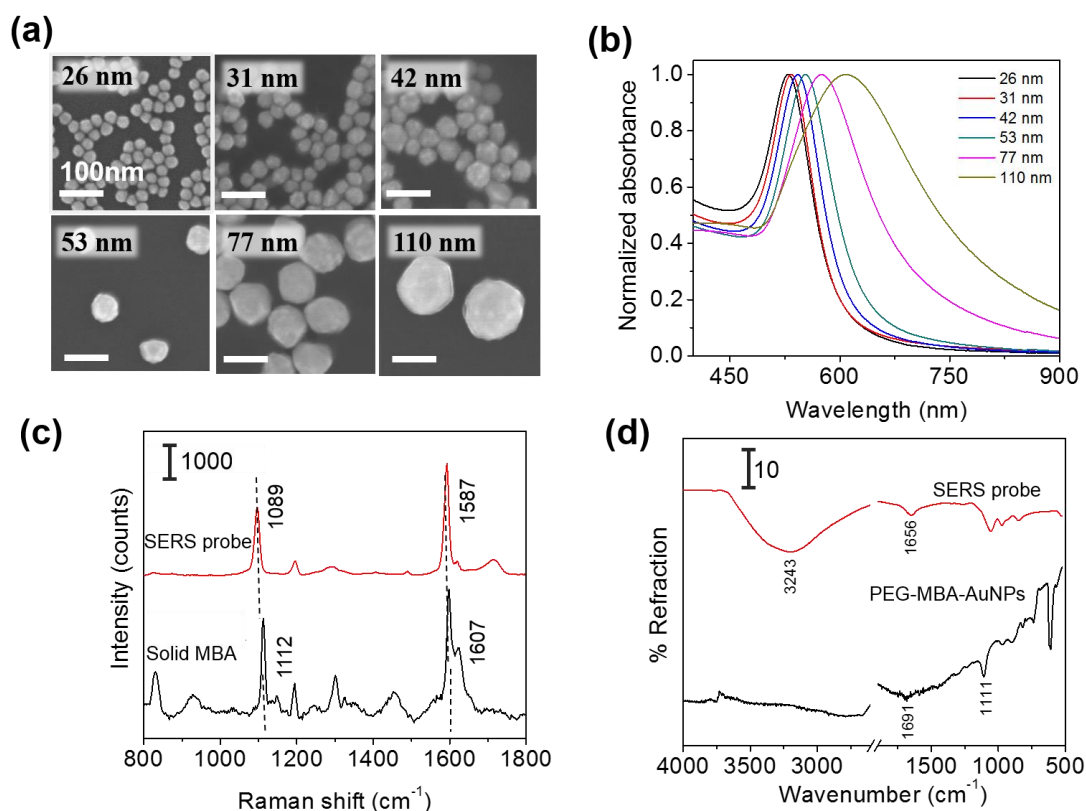


**Fig. 5-2** (a) SEM images of the citrate-capped AuNPs of different sizes. (b) Normalized extinction spectra of the PBS solutions of SERS probes of different sizes. (c) Raman spectra of the solid MBA and the 53 nm-SERS probes. (d) ATR-FTIR spectra of the PEGylated MBA-labeled AuNPs and the SERS probes of 53 nm in diameter.

### 5.3.2 Influence of SERS probe size on the sensitivity of SERS immunoassay

To roughly examine the influence of the SERS probe size on the sensitivity of immunoassay, the sandwich immunoassay for H-IgG was performed on the SERS substrates using SERS probes of different sizes (26, 31, 42, 53, 77, and 110 nm in diameter) at a constant target analyte concentration of 1 ng/mL. Figure 5-3(a) shows the SERS spectra of the sandwich immunoassay. The intensity of the characteristic bands of MBA increased with increasing probe size until 53 nm and then decreased. The probe size dependence of the 1587  $\text{cm}^{-1}$  band intensity is shown in Fig. 5-3(b), which clearly shows that it becomes maximum at a probe size of 53 nm. This result suggests that the size of the SERS probes that provide the highest sensitivity enhancement lies about 50 nm.

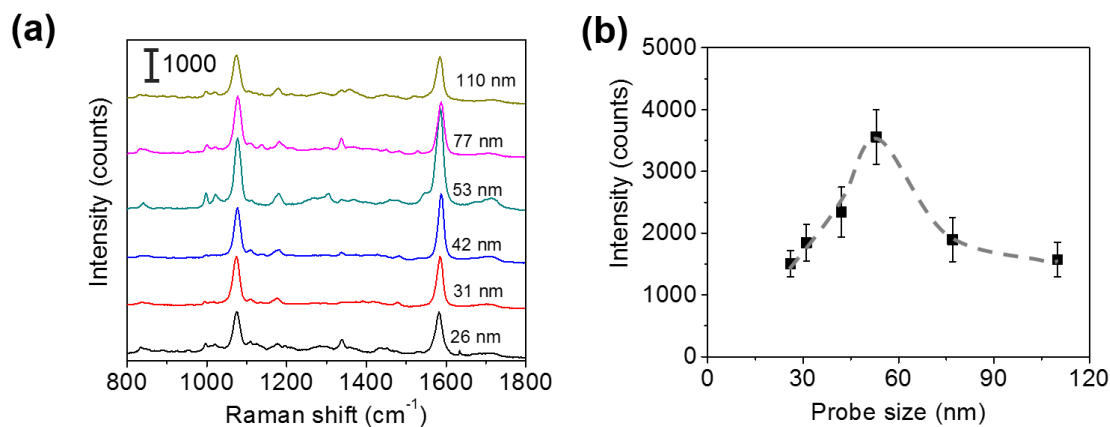


**Fig. 5-3** (a) SERS spectra of the sandwich immunoassay for H-IgG performed at a constant H-IgG concentration of 1 ng/mL using SERS probes of different sizes. (b) Probe size dependence of the SERS intensity of the 1587  $\text{cm}^{-1}$  band. The broken curve is a guide for the eye.

The sensitivity of SERS immunoassay must be discussed based on the slope of the sensitivity curve, which is the relationship between the SERS intensity and the concentration of target analyte. Thus, we determined the sensitivity curves of the sandwich immunoassay for SERS probe sizes of 26, 53, and 110 nm, which were selected as representative small, middle, and large probe sizes. The concentration of H-IgG antigen was varied from 0.1 pg/mL to 10 ng/mL by serial dilutions of H-IgG antigen solution. Figure 5-4 shows the sensitivity curves obtained by plotting the 1587  $\text{cm}^{-1}$  band intensity as a function of the logarithm of H-IgG concentration. The corresponding SERS spectra are shown in Fig 5-5. As shown in Fig. 5-4, the linear relationship was obtained in the H-IgG concentration range of 0.1 pg/mL to 10 ng/mL for all SERS probe sizes. The linear sensitivity curves obtained by the method of least squares are:  $y = 306x + 4110$  ( $r^2 = 0.97$ ) for 26 nm-probes,  $y = 726x + 9951$  ( $r^2 = 0.98$ ) for 53 nm-probes, and  $y = 377x + 5268$  ( $r^2 = 0.86$ ) for 110 nm-probe. By comparing their slopes, the sensitivity of immunoassay using 53 nm-probes was found to be approximately 2-fold higher than those using 26 nm- and 110 nm-probes. This probe size dependence of the immunoassay sensitivity is in good agreement with that of the SERS intensity at a constant H-IgG concentration shown in Fig. 5-3b. From these results, we conclude that the optimal SERS probe size is 53 nm. Here, we should note that the optimal size of SERS probes depends on the structure of SERS-active substrates used for immunoassay.

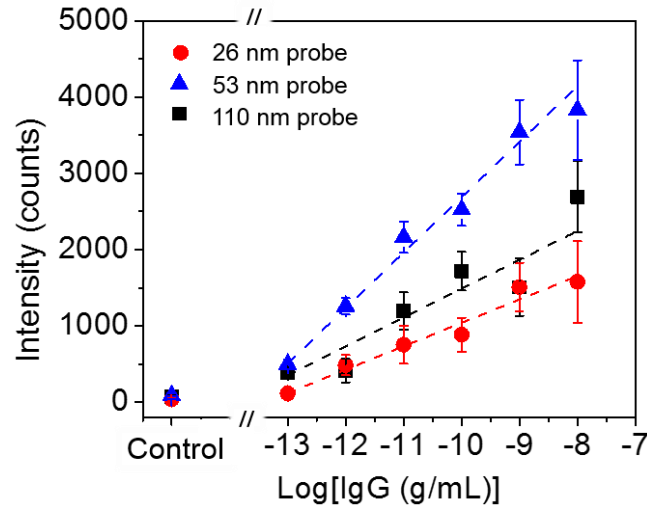


**Fig. 5-4** Sensitivity curves of H-IgG immunoassay using three probe size (26, 53, and 110 nm). The broken straight lines were obtained by the method of least squares.

We would like to discuss briefly why the maximum sensitivity is observed at a SERS probe size of 53 nm. Figure 5-6a shows the representative SEM images of the immunoassay substrates performed at a constant H-IgG concentration of 1 ng/mL using SERS probes of different sizes. (The corresponding SERS data are shown in Fig. 5-3). One can distinguish between the SERS probes and the Au@Ag NPs of the SERS substrate by the difference in size and brightness. The SERS probes situated at the top layer of 2D array appear brighter in the SEM images than the Au@Ag NPs. By counting SERS probes in the SEM images ( $3.5 \times 2.5 \mu\text{m}^2$ ) taken at five different positions, their surface density was evaluated. The result is shown in Fig. 5-6(b). The immobilized probe density decreased with increasing probe size, indicating that the immobilization probability of SERS probes decreased with increasing probe size. This may be due to the insufficient binding strength of antigen-antibody for immobilizing large SERS probes.

From the observed SERS intensity ( $I_{ob}$ ), the probe density ( $d_p$ ), and the excitation laser spot diameter ( $w_L = 4 \mu\text{m}$ ), the SERS intensity per a single SERS probe ( $I_s$ ) can be calculated by  $I_s = 4I_{ob}/(\pi \cdot w_L^2 \cdot d_p)$ .  $I_s$  is proportional to the effective Raman cross-section of a single SERS probe. The calculated results are shown in Fig. 5-6(c), indicating that the effective Raman cross-section increases with increasing probe size. This probe size dependence can be understood by considering the following two effects: one is the increase of Raman reporter molecules with increasing probe surface area, and the other is the decrease of the electromagnetic

field enhancement effect with increasing probe size due to the electromagnetic retardation effect. In the probe size range of less than 110 nm, the former effect is dominant. In consequence of the balance between the increase of  $I_s$  and the decrease of  $d_p$  with increasing probe size, the sensitivity enhancement showed a maximum around a probe size of 50 nm.

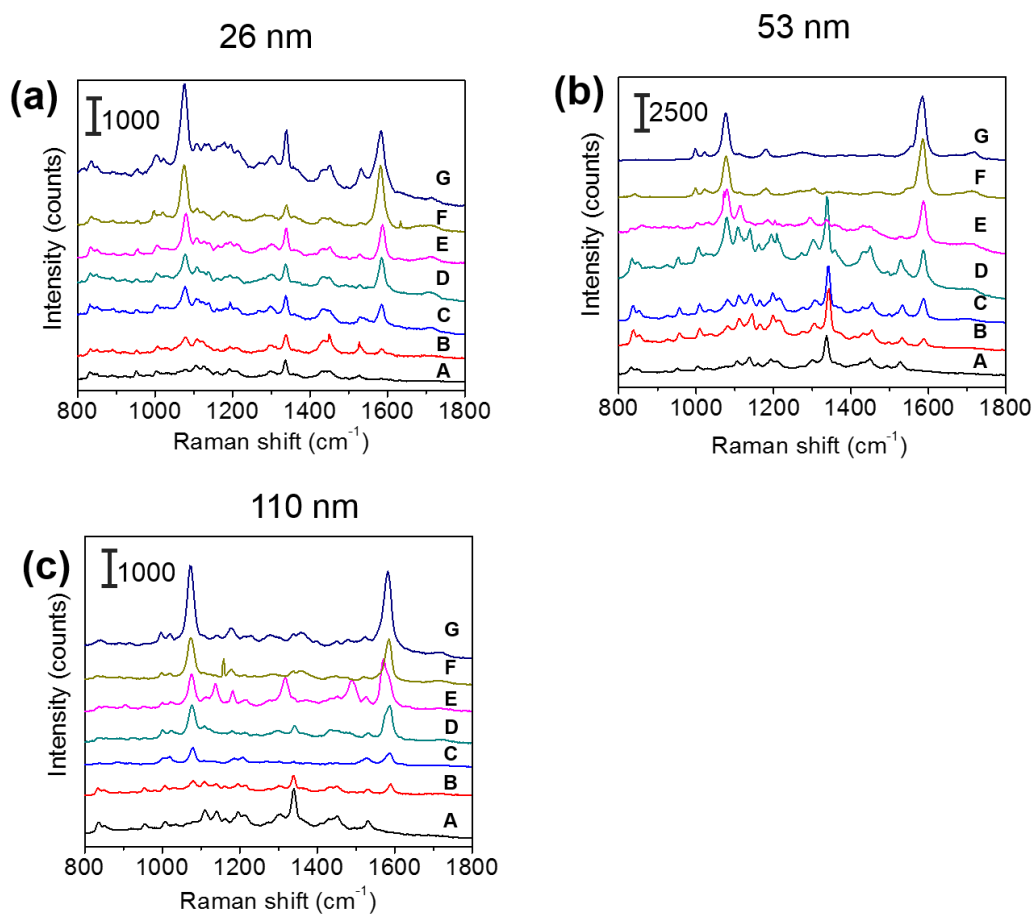


**Fig. 5-5** Raman spectra of immunoassay for H-IgG performed on the SERS substrates using (a) 26, (b) 53, and (c) 110 nm-SERS probes. The concentration of the antigen solution was varied from 0 (control) to 10 ng/mL: a = control, b = 0.1 pg/mL, c = 1 pg/mL, d= 10 pg/mL, e = 0.1 ng/mL, f = 1 ng/mL, and g = 10 ng/mL.

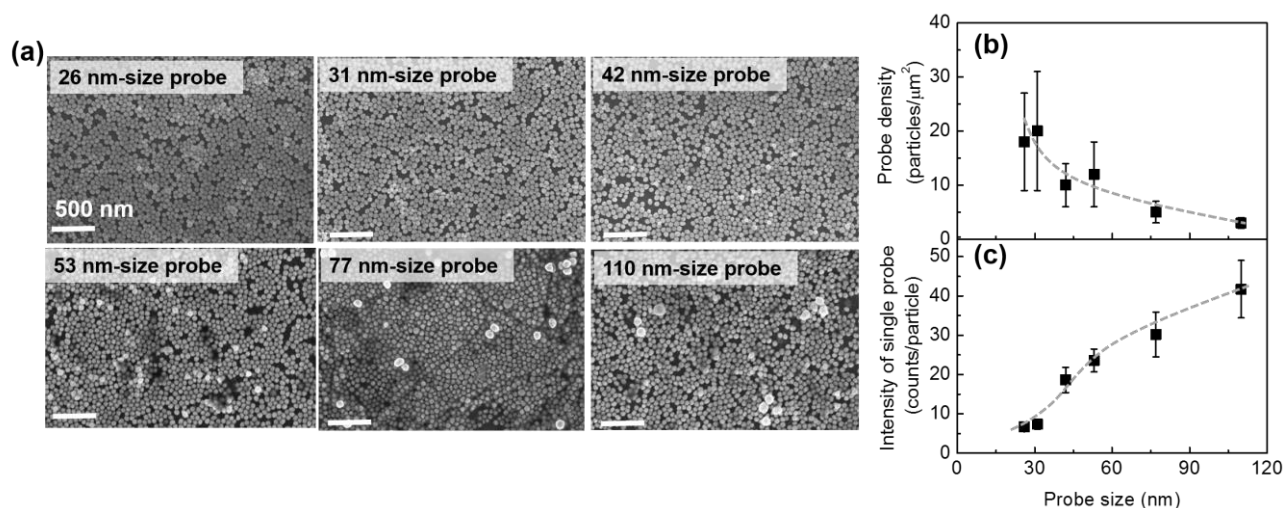


**Fig. 5-6** (a) Representative SEM images of sandwich immunoassay substrates performed at a H-IgG concentration of 1ng/mL using SERS probes of different sizes. Probe size dependence of (b) probe density and (c) SERS intensity of a single probe. The broken curves are guides for the eye.

### 5.3.3 Influence of separation distance between SERS probe and substrate on the sensitivity of SERS immunoassay

The influence of the size of sandwich immunocomplexes on the sensitivity of SERS immunoassay was examined. PSA and H-IgG were selected as representative small and large sandwich immunocomplexes [116,117], respectively, and 53 nm-SERS probes (optimized probe size) were used in these immunoassays. The molecular weights of the H-IgG antibody and antigen, and the PSA antibody (IgG2a isotype) were approximately 150 kDa, whose molecular size was reported to be  $15 \times 10 \times 4 \text{ nm}^3$  [118]. The molecular weight of the PSA antigen was 30 kDa, and its molecular size was estimated to be  $\sim 4 \text{ nm}$  in diameter by assuming the shape of PSA antigen as a globular shape [119], which was in good agreement with the molecular dimension estimated by simulation [117]. Thus, the size difference between the H-IgG and PSA sandwich immunocomplexes mainly arises from the difference in size of antigen. It is very difficult to determine the size of sandwich immunocomplex that determines the separation distance between the SERS substrate and SERS probe because it depends on the alignment structure of the capture antibody, antigen, and detection antibody. For simplicity, in this study the size of sandwich immunocomplex was estimated by sum of each component

size. Here, the sizes of the H-IgG antibody and antigen and the PSA antibody were assumed to be 12 nm [116], and the size of the PSA antigen was 4 nm.

The sensitivity curves for the detection of different analytes cannot be compared directly, because the ability of different antibodies to be immobilized onto the surface and the affinity towards their target antigens are different. Thus, the sensitivity enhancement factors obtained by replacing an Au film with the SERS substrate were evaluated for H-IgG and PSA detection, and then compared. By doing this, the influence of the size of sandwich immunocomplex on the sensitivity of SERS immunoassay could be investigated. To obtain the sensitivity curves of SERS immunoassay for H-IgG, the concentration of H-IgG antigen solution was varied from 0.1 pg/mL to 10 ng/mL. For the control sample, the PBS solution without H-IgG antigen was dropped onto the substrates. Figures 5-7(a) and 5-7(b) show the Raman spectra of the immunoassay for H-IgG conducted on the SERS and Au film substrates, respectively. The sensitivity curves obtained by plotting the peak intensity of the 1587  $\text{cm}^{-1}$  band as a function of the concentration of H-IgG are shown in Fig. 5-8(a). The linear relationship was observed in the concentration range of 0.1 pg/mL to 10 ng/mL for both Au film and SERS substrates. The linear relationships determined by the method of least squares are:  $y = 726x + 9951$  ( $r^2 = 0.98$ ) for the SERS substrate and  $y = 310x + 4335$  ( $r^2 = 0.87$ ) for the Au film substrate. By comparing the slopes, the sensitivity was found to be enhanced 2.3-fold by replacing the Au film substrate with the SERS substrate.

The sensitivity curves of the immunoassay for PSA are shown in Fig. 5-8(b), where the concentration of PSA solution was varied from 0.01 pg/mL to 1 ng/mL. The Raman spectra of the immunoassay for PSA on the SERS and Au film substrates are shown in Fig. 5-7(c) and 5-7(d), respectively. Figure 5-8(b) shows the sensitivity curves of the immunoassays for PSA performed on both substrates. The linear relation was found in the range of 1 pg/mL to 1 ng/mL:  $y = 827x + 10461$  ( $r^2 = 0.95$ ) for the SERS substrate and  $y = 128x + 1742$  ( $r^2 = 0.90$ ) for the Au film substrate. By comparing the slopes, the sensitivity of the immunoassay conducted on the SERS substrate was found to be 6.4-fold higher than that of the Au film substrate.

By comparing the sensitivity enhancement factors, we found that the sensitivity of the sandwich-type SERS immunoassay increased by a factor of 3 as the size of the sandwich immunocomplex decreased from 36 nm to 28 nm. This result can be understood by the increase of the plasmon coupling between the SERS probe

and the SERS substrate with decreasing separation distance between them, suggesting that the sensitivity of SERS-based immunoassay performed on SERS-active substrates can be improved by adopting an antibody-fragment instead of the antibody. Here, we note that the reduction of the affinity to bind with the target antigen must be avoided in producing antibody-fragments.

The SERS-based immunoassay reported here showed low LODs of 0.3 pg/mL (10 fM) for PSA and 0.05 pg/mL (0.3 fM) for H-IgG. The estimated LOD of our system for PSA was lower than those of the previously reported SERS immunoassays: 1 pg/mL for Au substrate with 5,5'-dithiobis(succinimidyl-2-nitrobenzoate)-labelled 30 nm-AuNPs probes [106] and, 1 pg/mL for 2D array of 20 nm AuNPs with rhodamine 6G-labelled 20 nm-AuNPs probes [120].

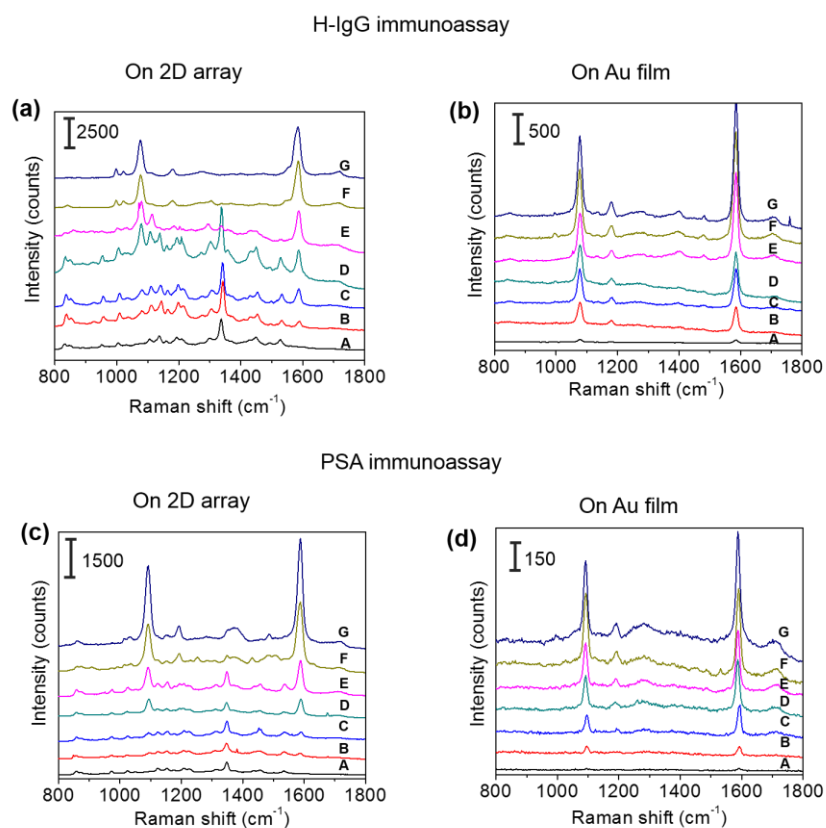


**Fig. 5-7** Raman spectra of the immunoassay for H-IgG performed on (a) SERS (2D array of Au@Ag NPs) substrates and (b) Au film substrates using 53 nm-SERS probes. The concentration of antigen solutions are: a = 0 (control), b = 0.1 pg/mL, c = 1 pg/mL, d = 10 pg/mL, e = 0.1 ng/mL, f = 1 ng/mL, and g = 10 ng/mL. Raman spectra of the immunoassay for PSA on (c) SERS and (d) Au film substrates using 53-nmSERS probes. The concentration of antigen solutions are: a = 0 (control), b = 0.01 pg/mL, c = 0.1 pg/mL, d = 1 pg/mL, e = 0.01 ng/mL, f = 0.1 ng/mL, and g = 1 ng/mL.

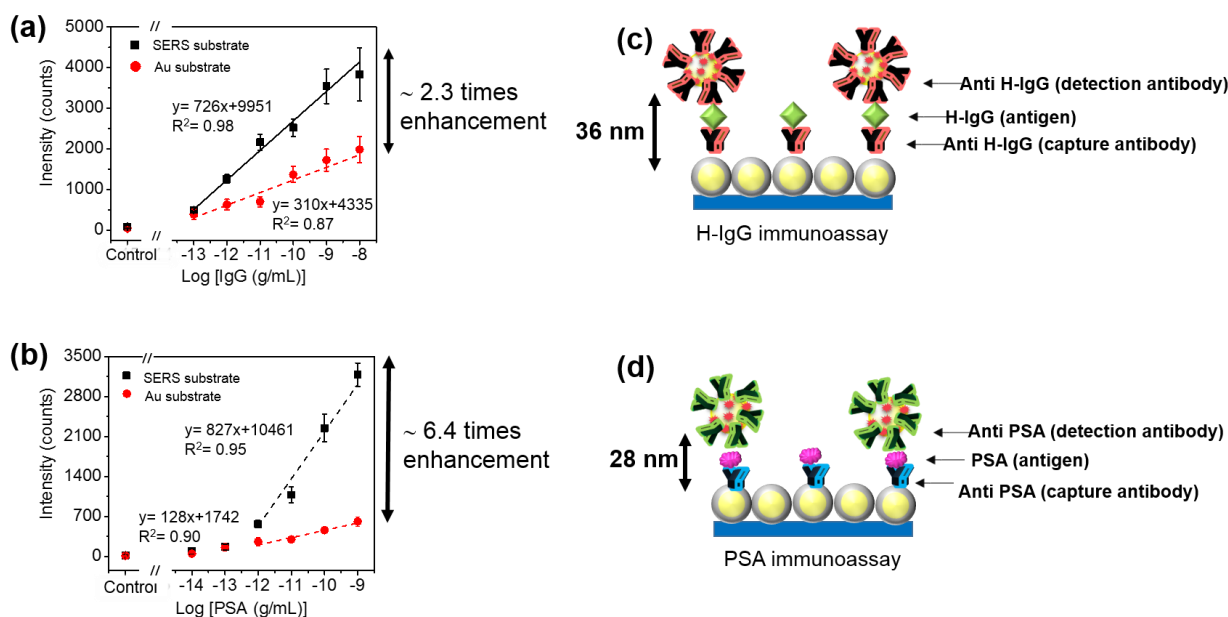


**Fig. 5-8** Sensitivity curves of the sandwich SERS immunoassays for (a) H-IgG and (b) PSA performed on the SERS and Au film substrates. The broken lines are obtained by the method of least squares. Schematic illustration of sandwich immunoassay for (c) H-IgG and (d) PSA.

## 5.4 Conclusion

The Influence of the sizes of SERS probe and sandwich immunocomplex on the sensitivity of sandwich-type SERS immunoassay has been investigated. Antibody-conjugated MBA-labeled AuNPs were served as the SERS probes. To enhance the SERS signal generated from the probe, the immunoassay was performed on the 2D arrays of Au@Ag NPs (SERS-active substrates). The sensitivity of immunoassay for H-IgG detection increased with increasing probe size up to 53 nm, and beyond this probe size, it began to decrease. We found that the sensitivity could be improved by a factor of 2 by using 53-nm probes, instead of 26 nm- or 110 nm-probes. Next, the influence of the size of sandwich immunocomplex on the sensitivity was examined by performing the sandwich immunoassay for H-IgG and PSA detection with 53 nm-SERS probes. We found that the sensitivity of the immunoassay increased by a factor of 3 as the size of sandwich immunocomplex decreased from 36 nm to 28 nm. This sensitivity enhancement can be attributed to the stronger plasmon coupling at the shorter separation distance between the SERS probe and the SERS substrate. This finding suggests that the sensitivity of sandwich SERS immunoassay performed on SERS-active substrates can be

improved by replacing the capture- and detection-antibodies with antibody-fragments if the affinity of the antibody-fragments to bind with the target antigen is unchanged.

## CHAPTER VI

### SUMMARY

In this dissertation, we have developed the highly sensitive immunoassay based on the SERS readout. This goal has been achieved by designing the suitable model of SERS substrate for immunoassay, structure and chemical constituents of SERS probe, and format of SERS immunosensors. Our SERS immunosensors consisted of two main components: SERS-active substrate and SERS probe. In the first step, the appropriate SERS substrates for immunoassay were developed. Before immunoassay, the SERS substrate (Au@Ag core-shell NPs 2D array), which has been proved to be highly sensitive SERS-active substrate [70], was fabricated by using the hybrid method. The as-prepared 2D array is hydrophobic substrate because the capping molecules are the mixture between dodecanethiol and octadecanethiol. The surface modification of this substrate is important for utilizing it as a solid support in an immunoassay because the hydrophobic substrate is not suitable for immunoassay. The hydrophilization was successfully performed by replacing hydrophobic molecules of mixed alkanethiols with a hydrophilic molecule of MHDA. At this step, this MHDA functionalized-SERS substrate is now suitable for utilizing as a solid support in SERS immunoassay because (i) biomolecules are able to bind to this substrate via amide bond formation between COOH of MHDA and NH<sub>2</sub> of biomolecules, and (ii) its LSPR (627 nm) matches to the excitation wavelength (632.8 nm) of our Raman system. Then, the SERS probes were fabricated by selecting 25-nm Au sphere as supporting material, TBBT as Raman reporter molecule, the mixture of PEG-SH and COOH-PEG-SH as protecting shell. The usability of the combination between the hydrophilized Au@Ag core-shell 2D array (SERS substrate) and TBBT-PEGylated-25 nm AuNPs (SERS probe) was demonstrated as a SERS immunosensor for influenza A detection employing direct immunoassay format. The nucleoprotein of influenza A was used as a target antigen. The specific recognition of antigen-antibody complexes was detected by measuring the SERS signal of TBBT molecule, which is the labeling molecule of SERS probe. To improve the sensitivity, the immunoassay was performed on the 2D arrays of Au@Ag core-shell NPs (SERS substrate). The sensitivity of immunoassay was enhanced ~4 times by using SERS substrate instead of flat Au substrate. It indicates that sensitivity improvement is attributed to the plasmon coupling between SERS substrate-probe. This SERS immunoassay for influenza A shows high

specificity to nucleoprotein against other proteins and high reproducibility with acceptable %RSD value. Moreover, this SERS immunosensor was applicable for detection of target nucleoprotein in the complex matrices (infected allantoic fluid) with a low limit of detection about 6 TCID<sub>50</sub>/mL. From the viewpoint of the plasmon coupling, the direct-type immunoassay is preferable, because of no need of capture-antibody: i.e. shorter separation distance. However, this immunoassay format suffers from lack of specific binding of antigen to the immunoassay substrate. The co-adsorption of the target antigens and other components of no interest generally occurs, leading to the lowering of the sensitivity. This disadvantage can be improved by using sandwich immunoassay format, which contained the layer of capture antibody on the substrate for selective binding with target analytes and decreasing non-specific adsorption of other protein. The sandwich immunoassay is expected to be highly sensitive, specific and reliable. However, the separation distance between the SERS probe and the SERS-active substrate should increase by the presence of capture-antibody, weakening their plasmon coupling. Therefore, the optimization of the SERS probe size and the minimization of the separation distance are essential for realizing a highly sensitive sandwich-type SERS immunoassay.

Then, the sandwich-type SERS-based immunoassay has been developed using hydrophilized 2D arrays of Au@Ag NPs as the SERS-active substrates. We have investigated the influence of the sizes of SERS probe and sandwich immunocomplex on the sensitivity. The SERS probes are AuNPs functionalized sequentially with MBA, HS-PEG-COOH, and the antibody specific to a target antigen. MBA was selected as the Raman reporter molecule because it shows strong Raman bands at 1099 and 1596 cm<sup>-1</sup> and has a carboxyl group for antibody immobilization. To realize highly sensitive detection, the optimization of SERS probe for sandwich immunoassay for H-IgG was carried out by varying the Au-core size of SERS probe from 26 to 110 nm. The maximum SERS intensity/sensitivity was found by using 53-nm-Au-core SERS probe. Next, to examine the influence of the size of sandwich immunocomplex on the sensitivity, the sandwich immunoassays for H-IgG and prostate-specific antigen (PSA) detection were performed using the SERS probes with 53 nm Au core size. The sandwich immunoassays for H-IgG and PSA were chosen as the large (36 nm in total size) and small (28 nm in total size) immunocomplexes, respectively. The sensitivity improvement of immunoassay performed on SER substrate was realized compared with that conducted on flat Au substrate. The large sensitivity improvement was obtained from the PSA immunoassay. It indicates that the short antigen/antibody length induces the strong plasmon coupling between SERS substrate-probe. By comparing the sensitivity

enhancement factors, we found that the sensitivity of the sandwich SERS immunoassay increased by the decrease of antigen size: i.e. the decrease of sandwich immunocomplex size. This result suggests that the sensitivity of SERS-based immunoassay performed on SERS-active substrates can be improved by reducing the size of sandwich immunocomplex, which can be achieved by replacing the antibody with an antibody-fragment with the same affinity to the target antigen.

Finally, we have succeeded in improving the performance of SERS immunoassay by using a hydrophilized 2D array of Au@Ag core-shell nanoparticles as a SERS substrate. We have demonstrated that the combined use of SERS substrate and Raman reporter molecule labeled-AuNPs decorated with the antibody (SERS probe) shows highly sensitive detection. The enhancement is attributed to the plasmon coupling between probe and substrate. The utilization of SERS-active substrate as a solid support for improving sensitivity has been previously reported by many groups. There are various designs and structures of the SERS-active substrates using in the immunosensors. However, the consideration of the uniformity of the substrate was very high, but the matching of LSPR of the substrate with excitation laser wavelength is still lacking. Therefore, we concerned the matching of LSPR of SERS-active substrate with laser line of 632.8 nm in Raman measurement to maximize the enhanced electromagnetic field. LSPR can be tuned by designing the structure of Au@Ag core-shell NPs. These sensitivity improvements also involved the optimization of SERS probe, type of immunoassay, and the size of the biomolecules. The sensitivity enhancement of SERS immunosensor strongly depends on probe size and the separation distance between probe and substrate. These studies are the guideline for fabrication of high sensitive sandwich SERS immunosensor. By comparing our immunosensor to other available immunosensors today, the high sensitivity is an advantage of our SERS immunosensor. In the aspect of practical application, however, our SERS immunosensor is still far from other methods that used routinely in the clinical laboratory because of many sample preparation steps and low coverage of biomolecule or SERS probe on the substrate. By simplifying preparation steps, increasing the density of SERS probe on the immunosubstrate, and decreasing of detection time, this sensor may be able to use as an alternative practical sensor without the requirement of the specialized personnel.

## **Future perspective**

In this study, we optimized many parameters for sensitivity improvement in SERS immunoassay. Our work shows that SERS offers high enhancement with appropriate SERS substrate, SERS probe size as well as the molecular size of antigen/antibody. These findings are the guidance for further improvement of SERS immunosensor. Progress in SERS immunosensor has been vastly focused on the development of the sensitivity of the sensor. However, there are some important points should be concerned to employ SERS immunosensor as the practical application, such as the production of SERS substrate with inexpensive, easy to handle, large enhancement, uniform, and reliable. Moreover, the regeneration of the SERS substrate or recyclable SERS substrate with maintaining the SERS activity after detection method is also necessary. Therefore, the regeneration step should be carried out. The substrate may possibly regenerate by using glycine-HCl buffer solution, which is mostly used to regenerate the metal surface. This idea will pave the way to further extend the improvement of SERS immunosensor.

## References

1. M. Santandreu, F. Céspedes, S. Alegret and E. Martínez-Fàbregas, *Anal. Chem.*, 1997, **69**, 2080-2085.
2. I. A. Darwish, *Int. J. Biomed. Sci.*, 2006, **2**, 217-235.
3. P. B. Luppá, L. J. Sokoll and D. W. Chan, *Clin. Chim. Acta*, 2001, **314**, 1-26.
4. N. B. Ramírez, A. M. Salgado and B. Valdman, *Braz. J. Chem. Eng.*, 2009, **26**, 227-249.
5. J. D. Driskell, PhD thesis, Iowa State University, 2006.
6. B. Sharma, R. R. Frontiera, A. I. Henry, E. Ringe and R. P. Van Duyne, *Mater. Today*, 2012, **15**, 16-25.
7. R. A. Tripp, R. A. Dluhy and Y. Zhao, *Nano Today*, 2008, **3**, 31-37.
8. K. C. Bantz, A. F. Meyer, N. J. Wittenberg, H. Im, Ö. Kurtuluş, S. H. Lee, N. C. Lindquist, S. H. Oh and C. L. Haynes, *Phys. Chem. Chem. Phys.*, 2011, **13**, 11551-11567.
9. M. Fleischmann, P. J. Hendra and A. J. McQuillan, *Chem. Phys. Lett.*, 1974, **26**, 163-166.
10. M. G. Albrecht and J. A. Creighton, *J. Am. Chem. Soc.*, 1977, **99**, 5215-5217.
11. D. L. Jeanmaire and R. P. Van Duyne, *J. Electroanal. Chem. Interfacial Electrochem.*, 1977, **84**, 1-20.
12. H. Xu, J. Aizpurua, M. Kall and P. Apell, *Phys. Rev. E: Stat. Phys., Plasmas, Fluids, Relat. Interdiscip. Top.*, 2000, **62**, 4318-4324.
13. A. V. Whitney, J. W. Elam, S. Zou, A. V. Zinovev, P. C. Stair, G. C. Schat and R. P. Van Duyne, *J. Phys. Chem. B*, 2005, **109**, 20522-20528.
14. N. E. Marotta, K. R. Beavers and L. A. Bottomley, *Anal. Chem.*, 2013, **85**, 1440-1446.
15. K. Kneipp, H. Kneipp, I. Itzkan, R. R. Dasari and M. S. Feld, *J. Phys.: Condens. Matter.*, 2002, **14**, R597-R624.
16. A. Campion and P. Kambhampati, *Chem. Soc. Rev.*, 1998, **27**, 241-250.
17. P. Kambhampati, C. M. Child, M. C. Foster and A. Campion, *J. Chem. Phys.*, 1998, **108**, 5013-5026.
18. P. B. Luppá, L. J. Sokoll and D. W. Chan, *Clin. Chim. Acta*, 2001, **314**, 1-26.
19. H. W. Schroeder and L. Cavacini, *J. Allergy Clin. Immunol.*, 2010, **125**, S41-S52.

20. C. A. Janeway, P. Travers, M. Walport and M. J Shlomchik, *Immunobiology: The Immune System in Health and Disease*, Garland Science, New York, 5th edn., 2001.
21. R. Reverberi and L. Reverberi, *Blood Transfus.*, 2007, **5**, 227-240.
22. E. Tapuhi, E. N. Venter and R. Klir, *S. Ar. Tydskr. Chem.*, 1996, **49**, 8-25.
23. G. S. Sittampalam, N. P. Coussens, K. Brimacombe, A. Grossman, M. Arkin, D. Auld, C. Austin, B. Bejcek, M. Glicksman, J. Inglese, P. W. Iversen, Z. Li, J. McGee, O. McManus, L. Minor, A. Napper, J. M. Peltier, T. Riss, O. J. Trask and J. Weidner, *Assay guidance manual*, Eli Lilly & Company and the National Center for Advancing Translational Sciences, Bethesda, 2004.
24. A. Ferreira, C. V. Uliana, M. Castilho, N. C. Pesquero, M. V. Foguel, G. Santos, C. S. Fugivara, A. V. Benedetti and H. Yamanaka, in *State of art in biosensors-Environmental and medical applications*, ed. T. Rinken, Intech, Rijeka, 2013, ch. 12, pp 255-266.
25. D. Grieshaber, R. MacKenzie, J. Vörös and E. Reimhult, *Sensors*. 2008, **8**, 1400-1458.
26. M. S. Castilho, T. Laube, H. Yamanaka, S. Alegret and M. I. Pividori, *Anal. Chem.*, 2011, **83**, 5570-5557.
27. P. D'Orazio, *Clin. Chim. Acta*, 2003, **334**, 41-69.
28. A. Janshoff, H. J. Galla and C. Steinem, *Angew. Chem. Int. Ed. Engl.*, 2000, **39**, 4004-4032.
29. R. Raiteri, M. Grattarola, H. J. Butt and P. Skladal, *Sensor. Actuat. B-Chem.*, 2001, **79**, 115-126.
30. N. V. Lavrik, M. J. Sepaniak and P. G. Datskos, *Rev. Sci. Instrum.*, 2001, **75**, 2229-2253.
31. A. Shons, F. Dorman and J. Najarian, *J. Biomed. Mater. Res.*, 1972, **6**, 565-570.
32. H. Marumatsu, *Anal. Chim. Acta*, 1986, **188**, 257-261.
33. K. Bernd and G. Michael, *Anal. Lett.*, 1993, **26**, 2313-2328.
34. M. Plomer, G. G. Guilbault and B. Hock, *Enzyme Microb. Technol.*, 1992, **14**, 230-235.
35. H. Muramatsu, J. M. Dicks, E. Tamiya and I. Karube, *Anal. Chem.*, 1987, **59**, 2760-2763.
36. R. C. Ebersole and M. D. Ward, *J. Am. Chem. Soc.*, 1988, **110**, 8623-8628.
37. C. K. O'Sullivan and G. G. Guilbault, *Biosens. Bioelectron.*, 1999, **14**, 663-670.
38. S. M. Borisov and O. S. Wolfbeis, *Chem. Rev.*, 2008, **108**, 423-461.
39. E. P. Meulenber, *Antibodies applications and new developments*, Bentham Science publishers, Sharjah, 2012.

40. N. Kim, I. S. Park and W. Y. Kim, *Sensor. Actuat. B-Chem.*, 2007, **121**, 606-615.
41. D. R. Shankaran, K. V. Gobi and N. Miura, *Sensor. Actuat. B-Chem.*, 2007, **121**, 158-177.
42. B. J. Luff, J. S. Wilkinson, J. Piehler, U. Hollenbach, J. Ingenhoff and N. Fabricius, *J. Lightwave Technol.*, 1998, **16**, 583-592.
43. B. K. Oh, Y. K. Kim, K. W. Park, W. H. Le and J. W. Choi, *Biosens. Bioelectron.*, 2004, **19**, 1497-1504.
44. A. Kłos-Witkowska, *Acta Biochim. Pol.*, 2016, **63**, 215-221.
45. H. Mukundan, A. S. Anderson, W. K. Grace, K. M. Grace, N. Hartman, J. S. Martinez and B. I. Swanson, *Sensors*, 2009, **9**, 5783-5709.
46. C. J. Orendorff, A. Gole, T. K. Sau and C. J. Murphy, *Anal. Chem.*, 2005, **77**, 3261-3266.
47. A. Barhoumi and N. J. Halas, *J. Phys. Chem. Lett.*, 2011, **2**, 3118-3123.
48. I. Pavel, E. McCarney, A. Elkhaled, A. Morrill, K. Plaxco and M. Moskovits, *J. Phys. Chem. C*, 2008, **112**, 4880-4883.
49. E. Podstawka and Y. Ozaki, *Biopolymers*, 2008, **89**, 807-819.
50. C. C. Lin, Y. M. Yang, Y. F. Chen, T. S. Yang and H. C. Chang, *Biosens. Bioelectron.*, 2008, **24**, 178-183.
51. J. D. Driskell, K. M. Kwarta, R. J. Lipert, M. D. Porter, J. D. Neill and J. F. Ridpath, *Anal. Chem.*, 2005, **77**, 6147-6154.
52. Y. Pei, Z. Wang, S. Zong and Y. Cui, *J. Mater. Chem. B*, 2013, **1**, 3992-3998.
53. A. Kamińska, E. Witkowska, K. Winkler, I. Dzięcielewski, J. L. Weyher and J. Waluk, *Biosens. Bioelectron.*, 2015, **66**, 461-467.
54. A. J. Driscoll, M. H. Harpster and P. A. Johnson, *Phys. Chem. Chem. Phys.*, 2013, **15**, 20415-20433.
55. C. David, N. Guillot, H. Shen, T. Toury and M. L. dela Chapelle, *Nanotechnology.*, 2010, **21**, 475501.
56. N. Xiao, C. Wang and C. Yu, *Biosensors*, 2013, **3**, 312-326.
57. Y. Wang, B. Yan and L. Chen, *Chem. Rev.*, 2013, **113**, 1391-1428.
58. X. Qian, X. H. Peng, D. O. Ansari, Q. Yin-Goen, G. Z. Chen, D. M. Shin, L. Yang, A. N. Young, M. D. Wang and S. Nie, *Nat. Biotechnol.*, 2008, **26**, 83-90.
59. R. Boyack and E. C. Le Ru, *Phys. Chem. Chem. Phys.*, 2009, **11**, 7398-7405.

60. S. E. Bell and M. R. McCourt, *Phys. Chem. Chem. Phys.*, 2009, **11**, 7455-7462.
61. N. A. A. Hatab, J. M. Oran and M. J. Sepaniak, *ACS Nano*, 2008, **2**, 377-385.
62. Y. K. Park and S. Park, *Chem. Mater.*, 2008, **20**, 2388-2393.
63. A. V. Whitney, J. W. Elam, S. Zou, A. V. Zinovev, P. C. Stair, G. C. Schatz and R. P. Van Duyne, *J. Phys. Chem. B*, 2005, **109**, 20522-20528.
64. H. Im, K. C. Bantz, N. C. Lindquist, C. L. Haynes and S. H. Oh, *Nano Lett.*, 2010, **10**, 2231-2236.
65. B. Sharma, M. F. Cardinal, S. L. Kleinman, N. G. Greeneltch, R. R. Frontiera, M. G. Blaber, G. C. Schatz and R. P. Van Duyne, *MRS bull.*, 2013, **38**, 615-624.
66. P. M. Fierro-Mercado and S. P. Hernández-Rivera, *Int. J. Spectrosc.*, 2012, **2012**, 716527.
67. M. Mulvihill, A. Tao, K. Benjauthrit, J. Arnold and P. Yang, *Angew. Chem., Int. Ed. Engl.*, 2008, **47**, 6456-6460.
68. D. J. King, *Avian Dis.*, 1991, **35**, 505-514.
69. K. Watcharatanyatip, S. Boonmoh, K. Chaichoun, T. Songserm, M. Woratanti and T. Dharakul, *J. Virol. Methods*, 2010, **163**, 238-243.
70. F. Pincella, Y. Song, T. Ochiai, K. Isozaki, K. Sakamoto and K. Miki, *Chem. Phys. Lett.*, 2014, **605-606**, 115-120.
71. U. T. D. Thuy, K. Sakamoto, S. Nishiyama, S. Yanagida, N. Q. Liem and K. Miki, *Langmuir*, 2015, **31**, 13494-13500.
72. T. Ochiai, K. Isozaki, S. Nishiyama and K. Miki, *Appl. Phys. Express*, 2014, **7**, 0065001.
73. K. Isozaki, T. Ochiai, T. Taguchi, K. Nittoh and K. Miki, *Appl. Phys. Lett.*, 2010, **97**, 221101.
74. N. Bhalla, P. Jolly, N. Formisano, P. Estrela, *Essays Biochem.*, 2016, **60**, 1-8.
75. N. Shah and D. C. Naseby, *Biosens. Bioelectron.*, 2015, **68**, 447-453.
76. A. Weinberg and M. L. Walker, *Clin. Diagn. Lab. Immunol.*, 2005, **12**, 367-370.
77. R. A. Medina and A. García-Sastre, *Nat. Rev. Microbiol.*, 2011, **9**, 590-603.
78. M. D. de Jong and T. T. Hien, *J. Clin. Virol.*, 2006, **35**, 2-13.
79. D. Nidzworski, P. Pranszke, M. Grudniewska, E. Król and B. Gromadzka, *Biosens. Bioelectron.*, 2014, **59**, 239-242.

80. K. Das, J. M. Aramini, L. C. Ma, R. M. Krug and E. Arnold, *Nat. Struct. Mol. Biol.*, 2010, **17**, 530-538.
81. X. Huang and M. A. El-Sayed, *J. Adv. Res.*, 2010, **1**, 13-28.
82. T. T. You, P. P. Yin, L. Jiang, X. F. Lang, L. Gou and S. H. Yang, *Phys. Chem. Chem. Phys.*, 2012, **14**, 6817-6825.
83. Y. Wang, L. Gan, H. Chen, S. Dong and J. Wang, *J. Phys. Chem. B*, 2006, **110**, 20418-20425.
84. S. Link, Z. L. Wang and M. A. El-Sayed, *J. Phys. Chem. B*, 1999, **103**, 3529-3533.
85. M. Xiao, J. Nyagilo, V. Arora, P. Kulkarni, D. Xu, X. Sun and D. P. Dave, *Nanotechnology*, 2010, **21**, 035101.
86. X. Qian, X. H. Peng, D. O. Ansari, Q. Yin-Goen, G. Z. Chen, D. M. Shin, L. Yang, A. N. Young, M. D. Wang and S. Nie, *Nat. Biotechnol.*, 2008, **26**, 83-90.
87. S. Hong and X. Li, *J. Nanomater.*, 2013, **2013**, 790323.
88. G. M. Marshall, F. Bensebaa and J. J. Dubowski, *J. Appl. Phys.*, 2009, **105**, 094310.
89. S. Bamrungsap, C. Apiwat, W. Chantima, T. Dharakul and N. Wiriyaichaiorn, *Microchim. Acta*, 2014, **181**, 223-230.
90. L. R. Farris, N. Wu, W. Wang, L. J. A. Clarizia, X. Wang and M. J. McDonald, *Anal. Bioanal. Chem.*, 2010, **396**, 667-674.
91. K. Ohtsuka, H. Endo, K. Morimoto, B. N. Vuong, H. Ogawa, K. Imai and S. Takenaka, *Anal. Sci.*, 2008, **24**, 1619-1622.
92. W. R. Thompson, M. Cai, M. Ho and J. E. Pemberton, *Langmuir*, 1997, **13**, 2291-2302.
93. M. A. Bryant and J. E. Pemberton, *J. Am. Chem. Soc.*, 1991, **113**, 8284-8293.
94. J. Mazur and B. Fanconi, *J. Phys. Chem.*, 1979, **71**, 3629-3637.
95. R. Wojnarowska-Nowak, J. Polit, D. Broda and E. M. Sheregii, *Arch. Metall. Mater.*, 2015, **60**, 2289-2296.
96. J. Cejkova, V. Prokopec, S. Brazdova, A. Kokaislova, P. Matejka and F. Stepanek, *Appl. Surf. Sci.*, 2009, **255**, 7864-7870.
97. N. Wiriyaichaiorn, W. Maneepprakorn, C. Apiwat and T. Dharakul, *Microchim. Acta*, 2015, **182**, 85-93.

98. C. Apiwat, N. Wiriyachaiporn, W. Maneepprakorn, T. Dharakul, C. Thepthai, P. Puthavathana, S. Siritantikorn and N. Horthongkham, *Arch. Virol.*, 2014, **159**, 1603-1611.
99. T. A. El-Brollosy, T. Abdallah, M. B. Mohamed, S. Abdallah, K. Easawi, S. Negm and H. Talaat, *Eur. Phys. J.: Spec. Top.*, 2008, **153**, 361-364.
100. C. Noguez, *J. Phys. Chem. C*, 2007, **111**, 3806-3819.
101. K. L. Kelly, E. Coronado, L. L. Zhao and G. C. Schatz, *J. Phys. Chem. B*, 2003, **107**, 668-677.
102. P. K. Jain, W. Huang and M. A. El-Sayed, *Nano Lett.*, 2007, **7**, 2080-2088.
103. G. Vidarsson, G. Dekkers and T. Rispens, *Front. Immunol.*, 2014, **5**, 520.
104. K. Karn-orachai, K. Sakamoto, R. Laocharoensuk, S. Bamrungsap, S. Songsivilai, T. Dharakul and K. Miki, *RSC Adv.*, 2016, **6**, 97791-97799.
105. M. Li, S. K. Cushing, J. Zhang, S. Suri, R. Evans, W. P. Petros, L. F. Gibson, D. Ma, Y. Liu and N. Wu, *ASC nano*, 2013, **6**, 4967-4976.
106. D. S. Grubisha, R. J. Lipert, H. Y. Park, J. Driskell and M. D. Porter, *Anal. Chem.*, 2003, **75**, 5936-5943.
107. H. Chang, H. Kang, E. Ko, B. H. Jun, H. Y. Lee, Y. S. Lee and D. H. Jeong, *ACS Sens.*, 2016, **1**, 645-649.
108. S. Link and M. A. El-Sayed, *J. Phys. Chem. B*, 1999, **103**, 4212-4217.
109. S. C. Boca, C. Farcau and S. Astilean, *Nucl. Instrum. Meth. B*, 2009, **267**, 406-410.
110. P. P. Fang, J. F. Li, Z. L. Yang, L. M. Li, B. Ren and Z. Q. Tian, *J. Raman. Spectrosc.*, 2008, **39**, 1679-1687.
111. P. K. Jain, K. S. Lee, I. H. El-Sayed and M. El-Sayed, *J. Phys. Chem. B.*, 2006, **110**, 7238-7248.
112. C. Song, L. Min, N. Zhou, Y. Yang, S. Su, W. Huang and L. Wang, *ACS Appl. Mater. Interfaces*, 2014, **6**, 21842-21850.
113. G. Varsányi, L. Láng, and M. A. Kovner, *Assignments for vibrational spectra of seven hundred benzene derivatives*, Institute of Physics Publishing, Bristol, 1974
114. S. J. Patil, N. Duragkar and V. R. Pao, *Sensor. Actuat. B-Chem.*, 2014, **192**, 444-451.
115. A. Barth, *Biochim. Biophys. Acta*, 2007, **1767**, 1073-1101.
116. R. Bharadwaj, S. Mukherji and S. Mukherji, *Plasmonics*, 2016, **11**, 753-761.

117. A. Stephenson-Brown, A. L. Acton, J. A. Preece, J. S. Fossey and P. M. Mendes, *Chem. Sci.*, 2015, **6**, 5114-5119.
118. V. R. Sarma, E. W. Silverton, D. R. Davies and W. D. Terry, *J. Biol. Chem.*, 1971, **246**, 3753-3759.
119. H. P. Erickson, *Biol. Proced. Online*, 2009, **11**, 32-50.
120. K. J. Yoon, H. K. Seo, H. Hwang, D. Pyo, I. Y. Eom, J. H. Hahn and Y. M. Jung, *Bull. Korean Chem. Soc.*, 2010, **31**, 1215-1218.
121. K. M. Mayer and J. H. Hafner, *Chem. Rev.*, 2011, **111**, 3828-3857.
122. N. L. Rosi and C. A. Mirkin, *Chem. Rev.*, 2005, **105**, 1547-1562.
123. S. K. Ghosh and T. Pal, *Chem. Rev.*, 2007, **107**, 4797-4862.
124. P. N. Sisco and C. J. Murphy, *J. Phys. Chem. A*, 2009, **113**, 3973-3978.
125. T. K. Sau and C. J. Murphy, *J. Am. Chem. Soc.*, 2004, **126**, 8648-8649.
126. A. R. Tao, S. Habas and P. Yang, *Small*, 2008, **4**, 310-325.
127. L. Deng , L. Liu , C. Zhu , D. Li and S. Dong, *Chem. Commun.*, 2013, **49**, 2503-2505.
128. D. Y. Kim, S. H. Im, O. O. Park and Y. T. Lim, *Cryst. Eng. Comm.*, 2010, **12**, 116-121.
129. A. Gole and C. J. Murphy, *Chem. Mater.*, 2005, **17**, 1325-1330.
130. H. Wang, C. S. Levin and N. J. Halas, *J. Am. Chem. Soc.*, 2005, **127**, 14992-14993.
131. A. P. Leonov, J. Zheng, J. D. Clogston, S. T. Stern, A. K. Patri and A. Wei, *ACS Nano*, 2008, **2**, 2481-2488.
132. R. G. Rayavarapu, W. Petersen, L. Hartsuiker, P. Chin, H. Janssen, F. W. van Leeuwen, C. Otto, S. Manohar and T. G. van Leeuwen, *Nanotechnology*, 2010, **21**, 145101.
133. N. Bogliotti, B. Oberleitner, A. Di-Cicco, F. Schmidt, J. C. Florent and V. Semetey, *J. Colloid Interface Sci.*, 2011, **357**, 75-81.
134. B. Tah, P. Pal, M. Mahato and G. B. Talapatra, *J. Phys. Chem. B*, 2011, **115**, 8493-8499.

## APPENDIX

### Surface potential change of cationic nanoparticles by polymer coating

#### 1. Introduction

Recently, various types of nanostructures containing structured surfaces and particles have been widely developed. Semiconducting/metallic nanoparticles, in particular, are promising candidates as new functional materials not only as catalysts but also as durable materials for use in novel optical sensors [121] and other devices [122]. Methods for their production have also been widely developed. These methods are usually classified into two types: “top-down” methods and “bottom-up” methods. The author’s group have been investigating the bottom-up methods primarily [70,73]. Among many types of metallic nanoshapes are used in many kinds of chemical sensors [123]. In these cases, a common detergent cetyltrimethylammoniumbromide (CTAB) is often used as a stabilizer for AuNPs with shapes such as cubes, cuboctahedra, octahedral, and rods [124-128]. Among these AuNPs, gold nanorod (AuNRs) are the most frequently used AuNPs. The presence of CTAB is important for nanoparticles synthesis; however, it is cytotoxic in nature [128]. Its strong attachment to the surface of AuNPs has been demonstrated in the literatures [129,130] (e.g., an 8-nm-thick rigid layer on AuNPs has been reported by Wang et al. [130]). Some research groups have reported their attempts to modify CTAB coating to other polymeric surfactant coatings [129,131,132]. These group focused on AuNRs because of their potential biological applications. In some cases, isotropic AuNPs exhibit a high positive charge density caused by CTAB cations. Highly surface-charged particles are strongly affected by a change in ionic strength. For some biological applications, we would prefer to avoid volatile organic contaminants and handle AuNPs only in the aqueous phase. In this paper, we describe a simple surface modification of CTAB(1)-coated AuNPs (referred to as CTAB(1)-AuNPs, hereafter) with two polymers used are poly(sodium 4-styrenesulfonate) (PSS(2)) and polyethyleneglycol bisphenol A epichlorodrin copolymer (PEG(3)). In order to avoid sample loss, we tried the method omitting the often-used biochemical process “dialysis”[133]. We have focused on these two polymers because of their properties of decreasing charge density/repulsion for stabilizing particles and the softness of the polymer chain coating,

which contrasts with the rigid CTAB(1) [130]. For comparison, we also used sodium dodecyl sulfate (SDS(4)) as a low molecular weight, negatively charged ionic coating agent.

## 2. Experimental

All chemicals, such as CTAB(1) (Sigma), PSS(2) ( $M_w = 70,000$ ; Aldrich), PEG(3) ( $M_w = 15-29$  kDa; Sigma-Aldrich), SDS(4) (Sigma-Aldrich), gold(III) chloride trihydrate ( $\text{HAuCl}_4 \cdot 3\text{H}_2\text{O}$ ) (Aldrich), ascorbic acid (Aldrich), and sodium borohydride ( $\text{NaBH}_4$ ) (Wako) were used as received. Water was filtered and deionized with a Milli-Q system (resistance  $18.2 \text{ M}\Omega$ , Millipore).

AuNPs were synthesized via a common seed-mediated growth method [127].  $\text{HAuCl}_4 \cdot 3\text{H}_2\text{O}$  was dissolved in aqueous solution of CTAB(1) and reduce with ice-cooled sodium borohydride to form a “seed solution”. After 1 h “growth solution” was prepared with additional  $\text{HAuCl}_4 \cdot 3\text{H}_2\text{O}$  and diluted seed solution. This mixture was reduced by addition of ascorbic acid in aqueous CTAB(1) solution. The obtained CTAB(1)-AuNPs were subsequently mixed with an aqueous solution of another coating agent (2-4). Each mixed solution was stirred for 1 h, centrifuged ( $6.8 \text{ krcf}$ , 10 min), and then washed twice with  $\text{H}_2\text{O}$ . we hereafter refer to CTAB(1)-AuNPs treated with coating agents (2-4) as coating agent (2-4)-AuNPs. UV-Vis-NIR spectra of AuNPs were measured using a Jasco V-670 spectrophotometer. The zeta potential (hereafter abbreviated as ZP) was determined with an ELSZ-1000 (Otsuka Electronics). Each hydrodynamic diameter (hereafter abbreviated as HD) was measured at  $25^\circ\text{C}$  by the dynamic light scattering (DLS) method using a DLS-8000 (Otsuka Electronics). Microscopic images and EDX measurements were recorded with either an HD-2000 (Hitachi) or a JEM-2100F (JEOL) operating at 200 kV.

## 3. Results and discussion

### 3.1 UV-Vis-NIR spectra of AuNPs

Each absorption spectrum was recorded and normalized at the  $\lambda_{\text{max}}$  of the AuNPs' band; the results are presented in Fig.S1. During the treatment with the coating agents (2-4), a portion of the AuNPs aggregated and attached to the walls of the container or was washed off. Therefore, the concentration of AuNPs decreased

to some extent. Thus, the baseline of each normalized spectrum appeared to shift upward compared to that of CTAB(1)-AuNPs. After the treatment, a blue color gradually appeared on the walls of PEG(3)-AuNPs. Nevertheless, the  $\lambda_{\text{max}}$  of the AuNPs' band was approximately the same for each AuNPs solution. In some cases, as long-term preservation was observed to be problematic, it needs to be improved.

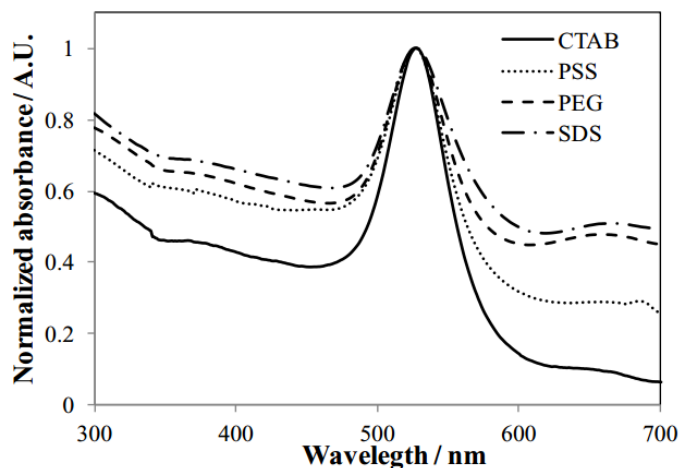


**Fig. S1.** Normalized absorption spectra of AuNPs treated with coating agents (1-4): CTAB(1)-AuNPs (solid line), and CTAB(1)-AuNPs treated with PSS(2) (dotted line), PEG(3) (broken line), and SDS(4) (dotted-chain line).

### 3.2 Zeta-potential measurements

The ZP values of coating agents (1-4) and the AuNPs treated with the coating agents were measured. The observed ZPs are listed in Table 1. CTAB(1) samples were the only ones that exhibited positive values, slightly more than those of AuNPs cubes reported in the literature (+23.2 mV) [124]. This result implies that CTAB(1) salt ionization ratios of the surface layer on the AuNPs differ. For PSS(2) samples, the observed value of ZP in the presence of AuNPs was -25 mV lower than that observed in the absence of AuNPs. This result suggests that PSS(2)-AuNPs were completely negatively charged with high coverage of PSS(2).

Although the ZP in the presence of AuNPs was approximate -40 mV, the ZP of PEG(3) appeared to be close to zero. This highly negative potential value probably arises from an excess amount of anions around the AuNPs in solution.

Based on the change in the ZP of SDS(4)-AuNPs compared to that of SDS(4), SDS(4) appears to form hybrid complexes with CTAB(1) [134] and to attach to NPs by mixing with CTAB(1)-AuNPs.

**Table S1.** ZPs (mV) of each coating agent (1-4), CTAB(1)-AuNPs, and coating agent (2-4)-AuNPs

<b>Samples</b>	<b>Coating agent only*</b>	<b>AuNPs**</b>
<b>CTAB(1)</b>	+45.8	+38.5
<b>PSS(2)</b>	-41.6	-68.9
<b>PEG(3)</b>	-9.1	-37.3***
<b>SDS(4)</b>	-66.8	-26.4

\*Values were recorded as soon as possible because each coating agent showed irreversible adsorption onto the electrodes and the polystyrene cell walls during the measurements, especially in the case of CTAB(1).

\*\*AuNPs corresponds to CTAB(1)-AuNPs or coating agent(2-4)-AuNPs.

\*\*\*Particles gradually aggregated on the polypropylene microtube walls during storage. Small amount of sediments were observed for other AuNPs

### 3.3 DLS measurements

The DLS results are summarized in Table S2. The average HD of CTAB(1)-AuNPs was 55.6 nm and was very similar to that of PSS(2)-AuNPs (53.4 nm). Gole et al [129] reported an increase of ~3.4 nm in the diameter of CTAB(1)-coated AuNRs after being treated with PSS (under experimental conditions that differ from ours). The HDs of PEG(3)-AuNPs in aqueous solution are larger than those of CTAB(1)- and PSS(2)-AuNPs.

One possible reason for this larger HDs is that the hydrophobic parts (“bisphenol A” moiety in PEG(3)) form a hybrid structure with CTAB(1) to stabilize the particles. The source of the high negative charge on the AuNPs in PSS(2)-AuNPs and SDS(4)-AuNPs is certainly attributable to the presence of PSS(2) and SDS(4), respectively. The reason for the high negative charge of PEG(3)-AuNPs, as reported in table S1, is unclear. According to the DLS results, the diameter of PEG(3)-AuNPs was large, which suggests the occurrence of a hydrodynamic effect between PEG moiety and water of CTAB(1) molecules in their aqueous solutions. In the transmission electron microscopy (TEM) images (shown later in Fig. S2), the observed diameters of the AuNPs did not substantially differ.

**Table S2.** HDs (nm) of particles in each surfactant (1-4) and CTAB(1)-AuNPs or coating agent (2-4)-AuNPs.

<b>Samples</b>	<b>Coating agent only*</b>	<b>AuNPs**</b>
<b>CTAB(1)</b>	241**	55.6
<b>PSS(2)</b>	107	53.4
<b>PEG(3)</b>	124	108
<b>SDS(4)</b>	219**	194

\*Each coating agent sample showed small (d2 nm, corresponding to a monomer/oligomer peak), intermediate (100-200 nm, micelles), and large (e800 nm, corresponding to a higher complex peaks). The listed values are those of middle-sized peaks because of their supposed nature. Each AuNPs sample also showed small (d10 nm), intermediate (50-200 nm), and large (e500 nm) peaks. The intermediate peaks values are listed.

\*\*Values were not stable because of the adsorbate nature of each coating agent.

### 3.4 Microscopic observation of AuNPs

CTAB(1)-AuNPs used in this investigation were rather polydispersed. The typical TEM images that were observed are presented in Fig. S2 and S3. We observed primarily hexagons and small AuNRs with aspect ratios less than ~3. Fig. S2 shows a typical projection view of the hexagonal particle. This image indicates that the particles shape would be cuboctahedral/octahedral. As Kim et al [128] described, depending on the stage of particle growth, the 100 faces are blocked with CTAB (1) because of their strong ability to bind to 100. TEM images of each AuNPs are presented in the Fig. S3. Because carbon deposition occurred rapidly during the microscopic observations, images were taken within a short time. In Fig.S3, the diameters of the particles appear to be similar, in contrast to their HDs reported in Table S2.

PSS(2)-AuNPs were dispersed better than others. The particles in other samples were closely packed. In the case of PEG(3)-AuNPs, in particular, NPs tended to form multilayers, even in areas with relatively small populations of NPs. Compared to the other samples, SDS(4)-AuNPs tended not only to aggregate but also to connect to one another, which may be related to the strong interaction between CTAB(1) cations and SDS(4) anions [134]. Average particle diameters of the AuNPs calculated from TEM images are  $44.7 \pm 3.2$  nm, 44.1

$\pm 3.1$  nm,  $43.9 \pm 3.3$  nm, and  $42.3 \pm 6.5$  nm for CTAB(1)-, PSS(2)-, PEG(3)-, and SDS(4)-AuNPs, respectively. Based on these calculated values, the average diameters of the AuNPs determined from TEM did not substantially differ. Because we did not use chemicals that induced digestive effects, such effects and other surface chemical reactions could be excluded in these cases.

Fig. S4 shows the typical overlay images of Br K-line maps and bright-field images for CTAB(1)- and PSS(2)-AuNPs (images for PEG(3)- and SDS(4)-AuNPs are not shown because no significant changes from the images in Fig.S4 are observed). From the Br K-line maps, a decrease in the amount of Br was not evident, probably because of the limited measurement time, the initial Br K-line intensity, and the existence of Au-Br bonds. Thus, Br was detected in all cases. The situations in aqueous solutions and those on the carbon-supported cellulose nitrate membrane on copper TEM grids certainly differ. The source of negative charge on PEG(3)-AuNPs in our case was suggested to be Br<sup>-</sup>, the CTAB(1) counter-anion.

We also measured and investigated the EDS spectra (data not shown) of each AuNPs. In the case of PEG(3)-AuNPs, two different areas were detected. One area contained many AuNPs and the other contained only polymer chains. Br L-lines were observed in both areas, indicating that the Br<sup>-</sup> ions were attached to PEG(3) polymer surface.

The differences between the microscopic images and the DLS/ZP results for the solutions may arise from the solvent evaporation process. In solutions, particles are possibly to have charges (either positive or negative). However, when samples are in a dried state, i.e., solid state, the charges on the AuNPs are compensated by the counter charges of the substrate or other molecules in the solutions. In the case of PEG(3), because the polymeric chain is highly hydrophilic, AuNPs are coated not only by the molecules of the coating agent, but also by numerous water molecules. Therefore, the HD would grow to be much larger than those of CTAB(1)- or PSS(2)-AuNPs. In the solid phase (as is the case of samples prepared for microscopic observations), AuNPs are dried by solvent evaporation.

The conditions around the AuNPs in a solution could be controllable by changing the method that is used to wash them. However, the ZP measurements indicated the presence of negative charges, which indicates that the number of anions located within the HD of the NPs should be larger than the number of the cations. In this study, AuNPs were initially coated with CTAB(1). To maintain the negative ZP of the AuNPs after

they have been coated with neutral PEG(3), the NP surface must contain more anions than cations. Br mapping is observed to be an ineffective method for tracing CTAB(1) cations ( a counter ion is Br<sup>-</sup>) because of polymer-CTAB(1) or polymer-Br<sup>-</sup> interactions. SDS(4) showed strong interaction with CTAB(1) partly aggregated on the TEM grids. Based on these results, we observed some interesting relationships between the polymer and particle charges. We expect to improve the mixing and washing procedures in future.

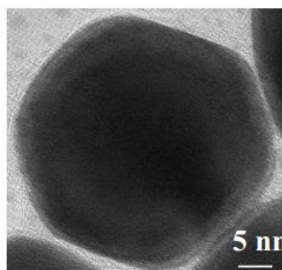


**Fig. S2** A typical TEM image of hexagonal shape CTAB(1)-AuNPs on a copper TEM grid

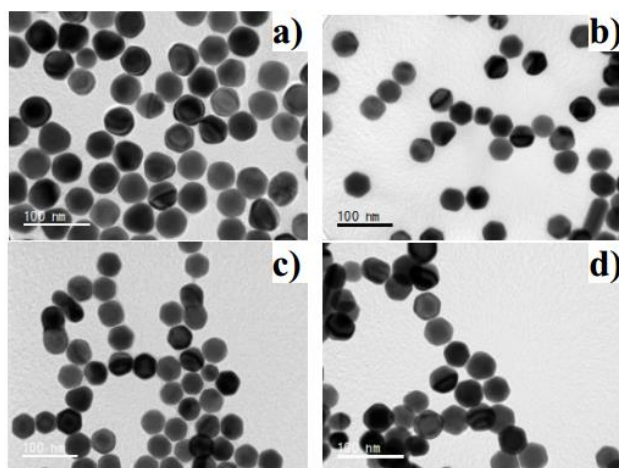


**Fig. S3** TEM images of CTAB(1)-AuNPs and coating agent (2-4)-AuNPs: a) CTAB(1)-AuNPs, b) PSS(2)-AuNPs, c) PEG(3)-AuNPs, and d) SDS(4)-AuNPs. Scale bars: 100 nm

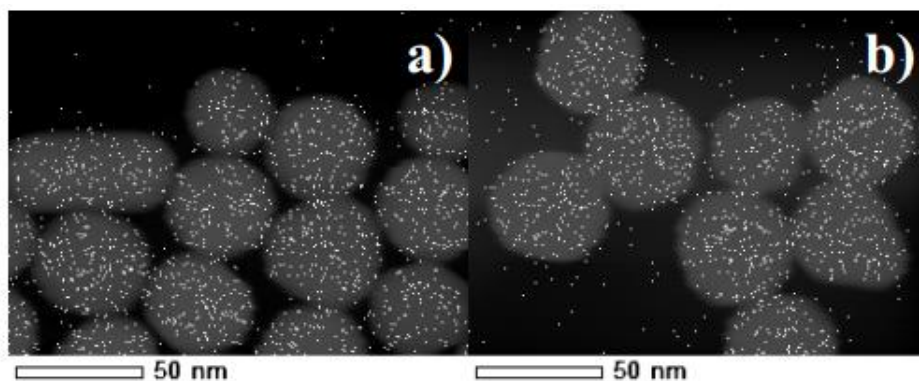


**Fig. S4** Typical EDX (Br K) mapping images of a) CTAB(1)-AuNPs and b) PSS(2)-AuNPs